

N°d'ordre :

Université des Sciences et Technologies de Lille

Ecole Doctorale Régionale Sciences pour l'Ingénieur Lille Nord-de-France

THÈSE

présentée à l'Université des Sciences et Technologies de Lille

pour obtenir le grade de

Docteur de l'Université

**Spécialité : Micro et Nano Technologies, Acoustique et
Télécommunications**

par

Wenxing ZHANG

**Etudes théoriques de l'effet du couplage
électron-phonon sur les propriétés de
transport dans les nanofils de silicium**

Soutenue le 15 Mai 2009 à Pékin à l'Institut de Physique de l'Académie des Sciences
de Chine devant le jury composé de :

Rapporteurs : Hong Guo
Jian Wang

Examineurs : Shiwu Gao
Wang Xiao Qun

Directeurs de thèse : Enge Wang
Guy Allan

Co-directeur : Christophe Delerue

Etudes théoriques de l'effet du couplage électron-phonon
sur les propriétés de transport dans les nanofils de silicium

For the Degree of
Doctor of Philosophy (Condensed Matter Physics)

Wenxing Zhang

Supervisors: Prof. Guy Allan (IEMN/CNRS)

Prof. Christophe Delerue (IEMN/CNRS)

Prof. Enge Wang (IOP/CAS)

Université des Sciences et Technologies de Lille
Graduate school of Chinese Academy of Sciences

9/03/2009

To my mother for her amazing courage and love

Acknowledgements

First of all, I would like to thank my supervisors Professor Wang Enge, Professor Guy Allan and Professor Christophe Delerue for always finding time to offer helpful support and enthusiastic encouragement when guiding me throughout the work. Professor Wang Enge is my Chinese supervisor and Professor Christophe Delerue is my French supervisor. I learn a lot from both of them during past several years. In particular, I am also grateful to Professor Guy Allan for his warm help and useful suggestions.

I would like to express my gratitude to all of you who helped me in many ways. I have had many inspiring discussions with Dr. Lu Wengang, Prof. Xu Lifang, Prof. Yao Yugui and Prof. Xue Qikun in IOP. I have got a lot of helps from Dr. Ludger wirdz, Engineer Jean-Michel, and our secretary Mrs. Florence Senez in IEMN.

I also would like to thank all the previous and present members in the Physique group of IEMN and the SF01 group of IOP. I appreciate the resources and environment of research in both institutes. The days in Lille and the days in Beijing leave lots of wonderful memories to me.

Lastly, I would like to thank my parents and my elder sister for their everlasting love. And thank my dear Feier for all her love and patience.

Thank you again and best wishes for all of you. Cheers!

Wenxing

in Beijing

Abstract

Zhang wenxing (Condensed Matter Physics)

Major Professors: Prof. Christophe Delerue and Prof. Wang Enge

In this thesis, the electronic structure, the phonon spectrum, and the electron-phonon (e-p) coupling effect in transport properties of Silicon Nanowires (SiNW) have been studied systematically based on Tight-Binding (TB) model and Valence-Force-Field (VFF) model. The electronic structure of SiNW is strongly dependent on the orientation and the diameter, even changing from direct gap to indirect gap, and the gap of SiNWs decreases and tends to the bulk value as the diameter increases. The phonon spectra are also dependent on the orientation and the diameter. It's a character of nanowires that there are four acoustic phonon modes. Based on the calculation of both low field mobility and lifetime of electrons in SiNWs along [110], it's confirmed that at room temperature the transport of carriers in SiNWs strongly depends on the phonon scattering, involving both optical phonons and acoustic phonons. The mobility increases and tends to the bulk value when the diameter increases. The mobility decreases in power law when the temperature increases from 77K to 300K. The relationship between the mobility and the density of carrier is more complicated. For low density of carrier ($<10^{19}/\text{cm}^3$), the mobility is almost constant because it is approximately independent on the Fermi level at low concentration. For higher concentration, the mobility is strongly dependent on the density of carrier because the Fermi level is high enough to cross the conduction band edge (CBE) and multi-band transport becomes important.

The current programs used in the investigation are developed by the author using Fortran90 programming language. The mode of sparse matrix diagonalisation, which is named 'diag_cg', is based on the conjugate gradient (CG) algorithm and was written by Dr. Y. M. Niquet. In the code, there are three different $\text{sp}^3\text{d}^5\text{s}^*$ TB models named as Boykin's, Jancu's and Niquet's, and each one can be used to construct the electron Hamiltonian as required. Spin-orbit coupling is included also. The code uses 'zheev' (from Lapack) and 'diag_cg' to diagonalize the Dynamical matrix and the Hamiltonian matrix separately. Formulas of electron-phonon coupling, derivative of Hamiltonian, and low-field mobility in 1D system are derived. Based on the formulas, the electron-phonon scattering rate and the low-field mobility are calculated. The density of state (DOS) and the vibration mode are also obtained. By the means of including all electron-phonon scattering, the transport behavior of electrons in SiNWs is studied systematically. The code is MPI/OpenMPI parallel.

TB model and Nonequilibrium Green's Function (NEGF) are used to calculate the ballistic transport properties of Carbon Nanotube (CNT) heterojunctions $(n_1, m_1)/(n_2, m_2)/(n_1, m_1)$.

Keywords: Silicon Nanowire, Diffusion Transport, Ballistic Transport, Tight Binding, Valence Force Field, Nonequilibrium Green's Function, Sparse Matrix, Transport of Carbon Nanotube

Résumé

Zhang wenxing (Condensed Matter Physics)

Major Professors: Prof. Christophe Delerue and Prof. Wang Enge

La structure électronique, le spectre de phonons et les effets du couplage électron-phonon (e-p) sur les propriétés de transport de nanofils de Si (SiNW) ont été étudiés systématiquement sur la base de calculs en liaisons fortes et en champ de forces de valence. La structure électronique des nanofils dépend de leur orientation et de leur diamètre, changeant d'une bande interdite directe à indirecte. La largeur de bande interdite décroît et tend vers celle du Si massif quand le diamètre croît. Les spectres de phonons dépendent également de l'orientation et du diamètre. Ils présentent quatre modes acoustiques ce qui est typique des systèmes unidimensionnels. La mobilité et le temps de vie des électrons dans des nanofils orientés [110] ont été calculés. Les calculs confirment qu'à température ambiante les propriétés de transport dans les SiNWs dépendent fortement de la diffusion par les phonons, impliquant à la fois des modes acoustiques et optiques tous dérivant des modes acoustiques du Si massif. La mobilité augmente et tend vers celle du massif quand le diamètre augmente, et elle décroît quand la température passe de 77K à 300K. La relation entre la mobilité et la densité de porteurs est plus complexe. Pour des densités inférieures à 10^{19} cm^{-3} , la mobilité est pratiquement constante car elle ne dépend pas de la position du niveau de Fermi. Pour des densités supérieures, la mobilité dépend très fortement de la densité de porteurs car le niveau de Fermi est suffisamment haut pour croiser le minimum de bande de conduction et le transport multi-bandes devient important.

Un autre travail entrepris dans la thèse a concerné la modélisation en liaisons fortes et en fonctions de Green hors équilibre du transport balistique dans des hétérojonctions de nanotubes de carbone $(n_1, m_1)/(n_2, m_2)/(n_1, m_1)$. La conductance des jonctions semiconductrices décroît exponentiellement quand la longueur du nanotube (n_2, m_2) augmente. Cependant la conductance de $(12, 0)/(9, 0)/(12, 0)$ augmente avec la longueur du nanotube $(9, 0)$. Cet accroissement anormal de la conductance est expliqué par l'évolution du potentiel. De plus, la relation entre la conductance et la symétrie de rotation dans les jonctions métalliques est étudiée. Un comportement universel de conductance est démontré et est interprété par la différence de phase des électrons qui traversent deux interfaces de la jonction. Finalement, la conductance balistique de multi-jonctions est étudiée et la possibilité de réaliser des composants basés uniquement sur des nanotubes de carbone est proposée.

Mots clés: Nanofil, Silicium, Transport diffusif, Transport balistique, Théorie, Liaisons Fortes, Modèle de Champ de Forces de Valence, Fonctions de Green hors équilibre, Nanotubes de carbone

Contents

Acknowledgements	i
Abstract	iii
Résumé	iv
1 Introduction	1
2 Background	3
2.1 State of art of SiNW	3
2.1.1 Fabrication of SiNW	4
2.1.2 Physical properties of SiNW	5
2.2 Structure of SiNW	6
3 Theoretical model	11
3.1 Tight-binding model	11
3.2 Valence force field model	15
3.2.1 Lattice dynamics	15
3.2.2 Calculation method	16
3.2.3 Valence force field model	17
3.3 Electron-phonon coupling theory	18
4 Programming	21
4.1 Outline of the code	21
4.2 Programming of electronic structure	24
4.3 Programming of phononic structure	26
4.4 Electron-phonon scattering matrix	27
4.4.1 Electron-phonon scattering matrix element	27
4.4.2 Energy conservation	30
4.5 Low field mobility and mean free path	32
4.5.1 Low field mobility	32
4.5.2 Mean free path	36

4.6 CG algorithm of diagonalisation of large sparse matrix	36
4.6.1 Storage of sparse matrix	36
4.6.2 CG algorithm	37
4.6.3 Convergence analysis	39
4.6.4 Preconditioned CG	40
4.6.5 Eigenvalue	41
4.7 Outlook of the code	41
5 E-p coupling effect in transport properties of SiNW	43
5.1 Electronic structure of SiNW	44
5.2 Phonon structure of SiNW	49
5.3 [110]SiNW: low-field mobility and e-p coupling effect	56
5.3.1 Low-field mobility versus density of carrier	57
5.3.2 Electron-transition rate	60
5.3.3 Low-field mobility versus diameter	64
5.3.4 Low-field mobility versus temperature	65
5.4 Summary	65
Appendix A: Y. M. Niquet TB model	67
Appendix B: Ballistic transport of CNT heterojunctions	71
B.1 CNT heterojunction	71
B.2 Theoretical background	75
B.3 Anomalous conductance of (12,0)/(9,0)/(12,0) junction	80
B.4 Ballistic transport of metallic CNT junctions	86
B.5 Ballistic transport of T junction and Cross junction	90
References	93
Publication & Meeting	109

Chapter 1 Introduction

Since the invention of transistor and integrated circuit, silicon industry developed rapidly and mankind has entered a digital age. This digital age is changing the way we live, work, communicate and research. Moore's Law¹⁻⁴ states that the number of transistors on a chip doubles about every two years. Increase of transistor density not only improves the performance but requires fabricating electronic devices smaller and smaller. Intel corporation^{5,6} has put '45nm technique CPU (Central Processing Unit)' into production in 2007. They have fabricated '32nm transistor' for SRAM successfully in 2008 and plan to realize the '32nm technique CPU' in 2009. Sub-10nm SiNWs have already been fabricated successfully with Electron beam lithography (EBL) or nano-imprint lithography (NIL) in laboratory. The transport properties of electronic devices in nano scale are totally different from the transport properties of traditional ones, because the quantum effect becomes more and more remarkable when the size of device decreases to nano scale. Owing to a lot of applications^{7,8}, nanomaterials like SiNWs⁹ or CNTs¹⁰ have become the foci of research at the end of last century. Fabrication, assembling and transport properties of devices in nano scale are studied extensively¹¹⁻²⁰ at the present time.

Theoretical studies of transport properties of materials started very early and combined with experiments closely all the time. A lot of outstanding scientists, like Faraday²¹, Boltzmann²², Dirac²³, Fermi²⁴, Landauer²⁵ and so on, spent a lot of time and energy even whole life on this subject. From classic transport²⁶ to quantum transport²⁷, researchers have developed various kinds of transport theory and applied them to a lot of problems successfully²⁷. Thanks to high performance computer, nowadays we can study the transport property of materials at atomic level. And in turn,

the study of transport property helps human to improve the performance of transistor and the speed of computer.

This thesis presents a theoretical study of electron-phonon coupling effect in transport properties of SiNWs. It consists of five chapters and two appendices. In chapter 2, we introduce the background of study and the structures of SiNW. In chapter 3, tight binding (TB) model, valence force field (VFF) model and electron-phonon (e-p) coupling theory are presented. In chapter 4, the algorithms and formulas employed in the code are introduced in detail in the order of electronic structure, phononic structure, e-p scattering matrix, low field mobility and diagonalisation of large sparse matrix. In the last section of chapter 4, we introduce some future development of the code. At the beginning of chapter 5, the electronic structures and phonon spectra of SiNWs along various orientations are presented and discussed. Then we introduce the low field mobility and transition rate of [110]SiNW, and we discuss the e-p coupling effect in transport properties of [110]SiNW in detail. At last, we introduce the Niquet's tight-binding model and the ballistic transport properties of CNT heterojunctions in appendix A and B separately.

Chapter 2 Background

Since the successful fabrication of high quality SiNW from 1997²⁸, numerous investigations of SiNW in both theory and experiment have been made in the past decade. This chapter introduces the fabrication, physical properties and structure of SiNW.

§2.1 State of art of SiNW

It can not be determined who discovered SiNW for the first time in history. As early as 1964, Wagner and Ellis fabricated ultra fine silicon filaments in laboratory²⁹ with vapor-liquid-solid (VLS) method, and the smallest silicon filament is about 90nm wide (Fig.2.1.1). In 1997, Westwater²⁸ *et al.* manufactured a quantity of thin SiNWs successfully. From then on, the fabrication and properties of SiNW are studied by a lot of groups all over the world.



Fig.2.1.1 Silicon filament from Wagner and Ellis³

2.1.1 Fabrication of SiNW

Vapor-liquid-solid (VLS)

The VLS method was proposed by Wagner and Ellis in 1964²⁹. Gold is generally used as the mediating solvent and SiCl_4 (diluted with H_2) or SiH_4 is used as the Si source gas (Fig.2.1.2). When the temperature is increased to $\sim 950^\circ\text{C}$ which is higher than the eutectic temperature ($\sim 370^\circ\text{C}$) of gold-silicon alloy and lower than the melting points of both gold (1063°C) and silicon (1414°C), the gold nano-particle melts into liquid droplet and silicon atoms are attached to the surface of droplet. Then silicon atoms pass through the gold droplet and are deposited on the substrate, and consequently the SiNW grows. The VLS method is a kind of bottom-up method.

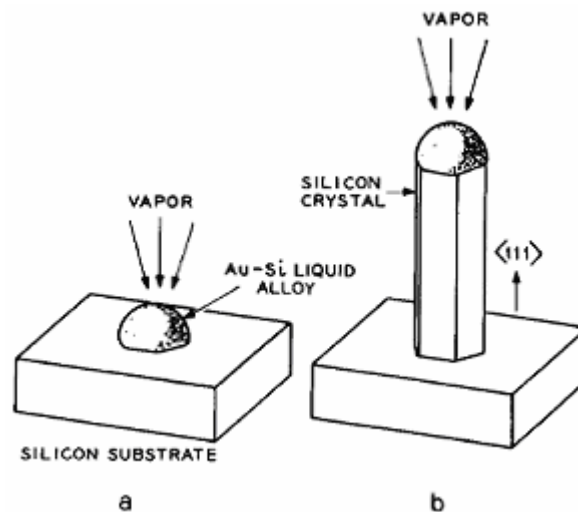


Fig.2.1.2 Schematic diagram of vapor-liquid-solid method³

Electron-beam-lithography (EBL)

The principle of EBL³⁰ is to apply an electron sensitive polymer film to a sample surface and then expose certain parts of the sample to the scanning electron beam to form a user-defined pattern. Further, this pattern can be transferred to the silicon layer by etching. It's a top-down method.

Nano-imprint-lithography (NIL)

NIL³¹ is a novel method of fabricating nanometer scale patterns. It creates

patterns by mechanical deformation of imprint resist and subsequent processes. It is a simple process with low cost, high throughput and high resolution. In principle, there is no limitation on the smallest size that can be fabricated.

2.1.2 Physical properties of SiNW

Bulk silicon is indirect gap semiconductor³². The gap is 1.17eV at 0K and 1.21eV at 300K. From measurements³³, it is found that the gap of SiNW increases from 1.1eV to 3.5eV when the diameter of SiNW decreases from 7nm to 1.3nm and it is in consistent with the theoretical prediction^{34,35}. Measurements on the transport properties of SiNWs doped with impurities show the transport of carrier in SiNW belongs to diffusion category. And heavily doped SiNW appears metallic. Gunawan³⁶ *et al.* fabricated SiNW arrays on insulator substrate and measured the transport properties (Fig.2.1.3). They found the mobility of carrier in SiNW is very different from the planar silicon inversion layers. First, the mobility is very small for low density of carrier. Second, the mobility increases to a maximum for moderate density of carrier. Third, for high density of carrier the mobility decreases to a limit.

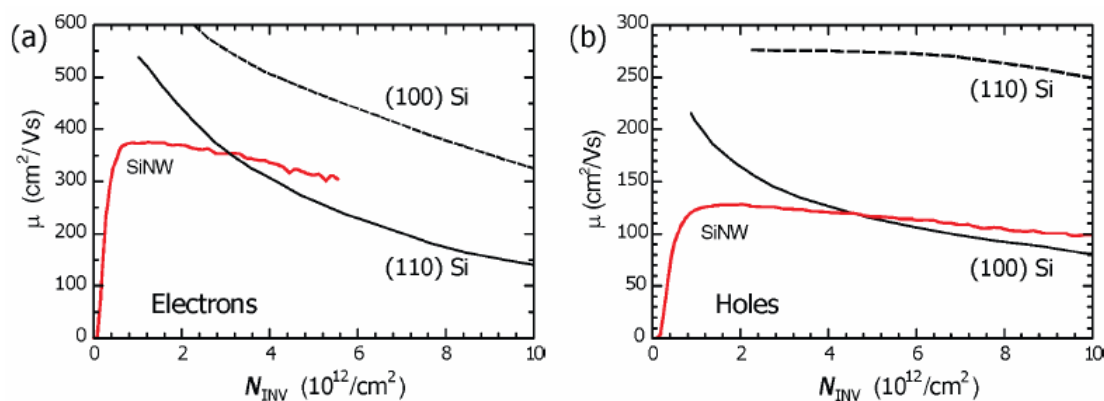


Fig.2.1.3 Comparison of electron mobility (a) and hole mobility (b) in SiNW-FET³⁶ (red) with planar silicon inversion layer (black). N_{INV} is the inversion carrier density.

For theoretical study, Zhao³⁷ *et al.* calculated the electronic structure of SiNW from first principle and they introduced the GW correction to obtain correct gap. Thonhauser³⁸ *et al.* calculated the phonon dispersion relation of [111]SiNW with

Stillinger model and they found four acoustic modes in SiNW while there are only three acoustic modes in bulk materials generally. It is a character for one dimensional (1D) structure.

From both experiments and calculations, we see there are big differences in electronic properties, phononic properties and transport properties between SiNW and bulk silicon. So far, theoretical studies have explained the electronic properties and phonon properties successfully. However, theoretical studies of electronic transport properties of SiNW are far from comprehension³⁹⁻⁴². There are several reasons: first, a lot of studies are based on simplified models of electrons or phonons, like $k \cdot p$ model for electron^{40,42} or continuum model for phonon^{39,41}; second, electronic structure or phononic structure of SiNW is too expensive to calculate by ab-initio method; third, phonon modes in previous works are treated as two parts, that is, acoustic modes and optical modes, so the discussion of electron-phonon (e-p) coupling is divided into two parts also, which results in a big difficulty for the analysis under uniform frame. Macro phenomena come from micro mechanism. Especially on nanometer scale, a little change of microstructure can result in a remarkable effect in e-p coupling and transport properties. For the purpose of investigating e-p interactions and e-p coupling effect in transport properties of SiNWs systematically, we derive the algorithm of e-p coupling in 1D system and develop the corresponding code which includes full electronic band structure, full phonon structure and all e-p scatterings in the calculation of transport properties.

§2.2 Structure of SiNW

Crystalline SiNW is always along a fixed orientation. For convenience, SiNWs are named after their orientations, like [001], [110], [111] or [112]. With transmission electron microscopy (TEM), scanning electron microscopy (SEM), X-ray diffraction, Infrared spectra or Raman scattering, people can determine the atomic structure of SiNW directly. A high-resolution-transmission-electron-microscopy (HRTEM) photo

of [111]SiNW is shown in Fig.2.2.1⁴³. The inside of nanowire is crystalline silicon and the outside is SiO_x.

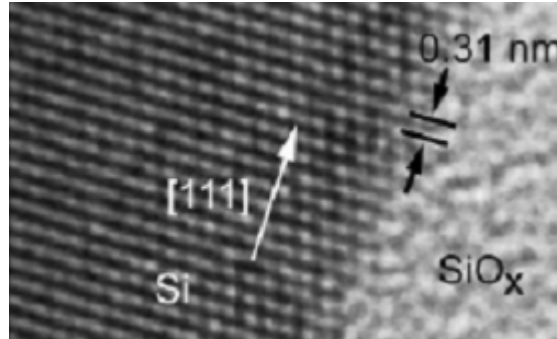


Fig.2.2.1 HRTEM photo for [111]SiNW⁴³

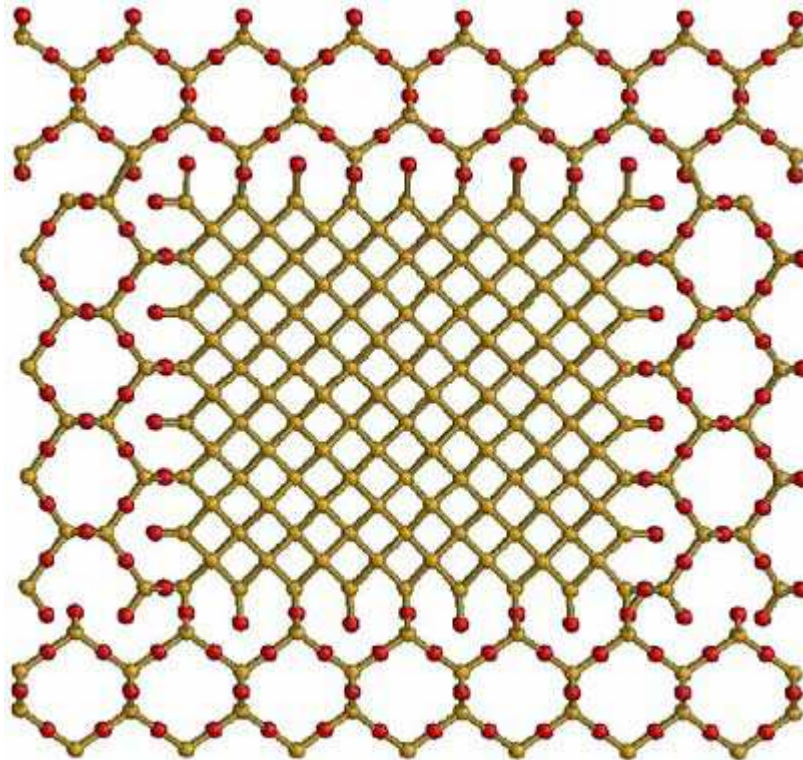


Fig.2.2.2 Atomic structure of [001]SiNW with square cross section and saturated with silicon dioxide. (yellow ball: silicon atom, red ball: oxygen atom)⁴⁴

In theory, there are several different opinions about the cross section shape of SiNW and the saturation of dangling bond on nanowire surface. Sacconi⁴⁴ *et al.* used square cross section and saturated the dangling bonds with silicon dioxide in

[001]SiNW (Fig.2.2.2). Thonhauser³⁸ *et al.* used hexagonal cross section and retained the dangling bonds in [111]SiNW (Fig.2.2.3). Niquet⁴⁵ *et al.* chose circular cross section and saturated the dangling bonds with hydrogen atoms. In this thesis, circular cross section and hydrogen saturation are chosen. Because the circular cross section is the most common shape for SiNWs made in experiment and the most stable shape in configuration relaxations. SiNW will be metallic and reactive if dangling bonds exist, so the passivation is also necessary.

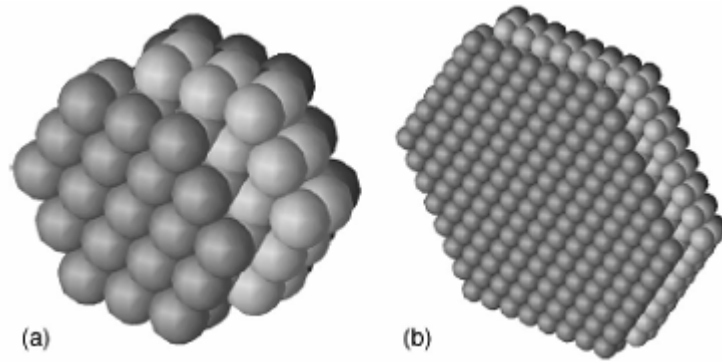


Fig.2.2.3 [111]SiNW with hexagonal cross section and without passivation³⁸

In the construction of SiNW, we cut a cylinder from the bulk silicon along a fixed orientation, and then we put hydrogen atoms on the dangling bonds. It's worth noting that the silicon atoms on which there are three dangling bonds are replaced by hydrogen atoms directly because such silicon atoms are reactive and unstable. The radius⁴⁵ of SiNW is defined as:

$$r = \sqrt{\frac{Na^3}{8\pi l}} \quad (2.2.1)$$

where a ($=5.431\text{\AA}$) is the lattice constant of silicon, N is the number of silicon atoms in one unit cell and l is the length of unit cell:

$$l = \begin{cases} a & , \text{for } [001] \\ a/\sqrt{2} & , \text{for } [110] \\ \sqrt{3}a & , \text{for } [111] \\ 3a/\sqrt{6} & , \text{for } [112] \end{cases} \quad (2.2.2)$$

Fig.2.2.4 illustrates the atomic structure of SiNWs created by author.

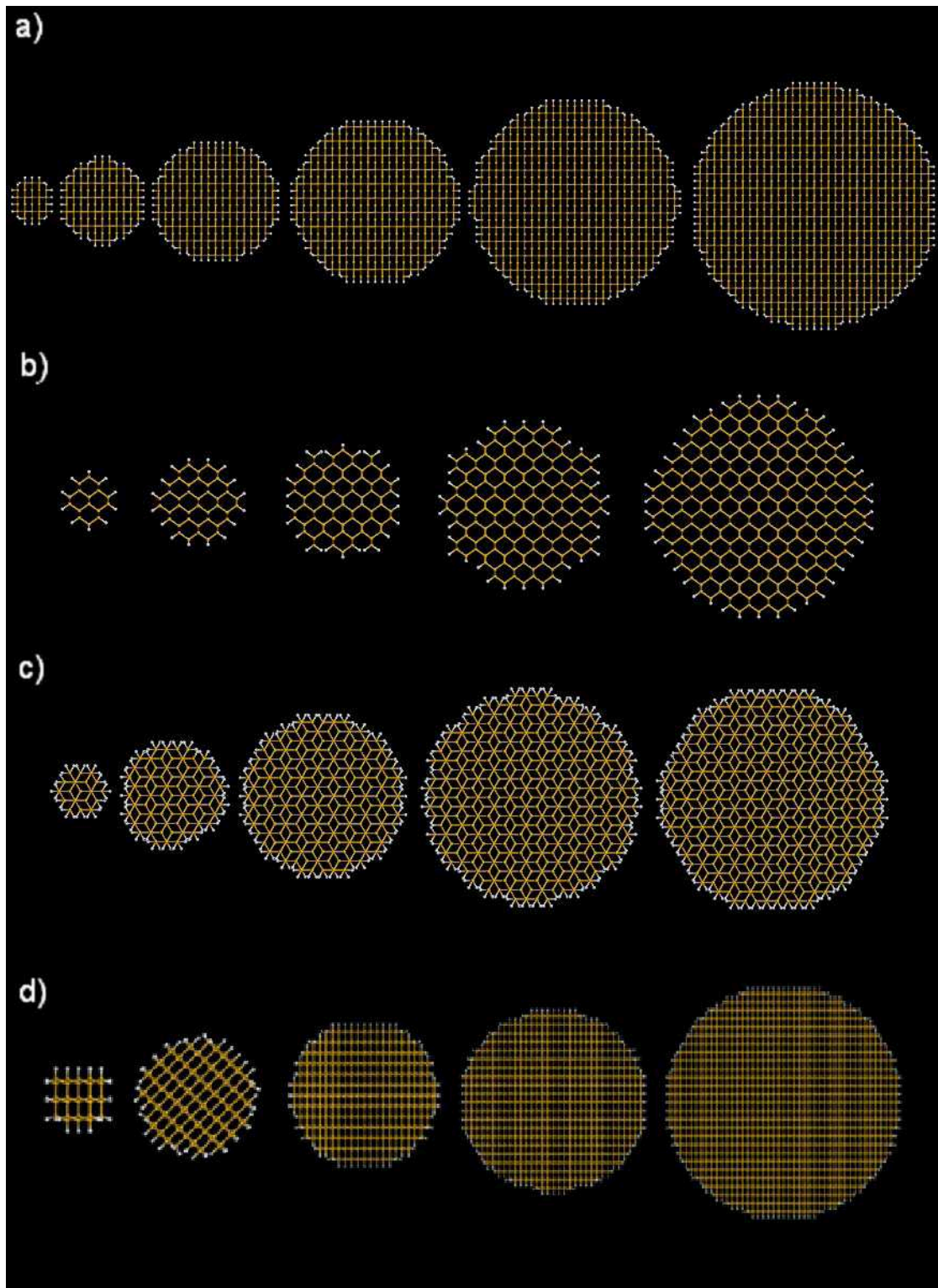


Fig.2.2.4 Cross section view of atomic structure for SiNWs along different orientations and with various diameters: a)[001]SiNW, b)[110]SiNW, c)[111]SiNW, d)[112]SiNW.

Chapter 3 Theoretical model

Electronic band structure and phononic dispersion relation of SiNW are not only important physical properties but the basis for calculation of e-p coupling. Since J. C. Slater and G. F. Koster raised the two-center approximation⁴⁶ in 1954, the tight-binding (TB) method developed quickly and was used to explore the electronic structure of various materials successfully⁴⁷. So far, among various TB models the $sp^3d^5s^*$ model⁴⁸ is the most accurate one to describe the electronic band structure of silicon. Lattice dynamics⁴⁹ combined with valence-force-field (VFF) model⁵⁰ give us the phonon dispersion relations. Keating model⁵¹ is famous and D. Vanderbilt *et al.* generalized it to describe anharmonic vibration of silicon⁵². This chapter introduces the $sp^3d^5s^*$ TB model and Vanderbilt VFF model which are used in our study. And then the e-p coupling theory for nanowire is presented and the formula of electron transition rate is derived.

§3.1 Tight-binding model

In the main, there are three different methods to determine the electronic structure of materials: quantum Monte-Carlo method⁵³, ab-initio method⁵⁴ and TB method⁴⁶. Due to the limitation of computing power and the need of explicit Hamiltonian in e-p coupling, the first two methods, quantum Monte-Carlo and ab-initio, are not suitable for the calculation of e-p coupling currently. TB models can describe the quantum effect of systems because it is based on the quantum mechanics. The Hamiltonian of TB is parameterized and TB parameters are fitted with ab-initio

results or experimental data. Because of parameterization, it's convenient to construct a TB Hamiltonian matrix of a system. But in turn, the transferability of the TB model is limited by the parameters also. In general, TB model is not as accurate as ab-initio method. But in applications a TB model can also be very accurate in describing the electronic structure with well-fitted parameters, and there have been a lot of successful applications⁵⁵ already. Additionally, the number of nonzero elements in TB Hamiltonian matrix is proportional to the number of atoms in one unit cell, thus it's possible and suitable to use sparse matrix skill to calculate the energy bands of electrons. And it's very important for the analysis of e-p coupling to calculate the electron energy bands quickly. Due to all above reasons, we choose the TB method to describe the electronic structure of SiNW.

In Bloch theorem⁵⁶, electron wave function can be expanded into a linear combination of atomic orbitals (LCAO):

$$\sum_{R_i} e^{ik \cdot R_i} \phi_n(r - R_i) \quad (3.1.1)$$

where R_i denotes the summation over all unit cells.

Using the atomic orbitals ϕ as basis⁵⁷, the Hamiltonian is a matrix but three-center integrals appear. The three-center integrals are difficult to deal with. In 1954, J. C. Slater and G. F. Koster proposed a simplified method, that is two-center approximation⁴⁶. It means we can disregard the three-center integrals and fit the Hamiltonian parameters up to two-center integrals only. From then on, the TB method is applied successfully to a lot of materials involving insulators⁵⁸, semiconductors⁵⁹ and even metals⁶⁰. From two-center approximation, the Hamiltonian matrix is represented by several parameters $(ss\sigma)$, $(pp\sigma)$, $(pp\pi)$, $(dd\sigma)$, $(dd\pi)$, $(dd\delta)$, $(sp\sigma)$, $(sd\sigma)$, $(pd\sigma)$ and $(pd\pi)$. The expressions for off diagonal Hamiltonian matrix elements are shown in Table 3.1.

All TB parameters used in this thesis are prepared by Dr. Y. M. Niquet⁶¹ and fitted with ab-initio results which are obtained from the calculation of band structures using ABINIT package⁶².

Table 3.1 Off-diagonal elements in Hamiltonian matrix⁴⁶

$E_{s,s}$	$(ss\sigma)$
$E_{s,x}$	$l(sp\sigma)$
$E_{x,x}$	$l^2(pp\sigma) + (1-l^2)(pp\pi)$
$E_{x,y}$	$lm(pp\sigma) - lm(pp\pi)$
$E_{x,z}$	$nl(pp\sigma) - nl(pp\pi)$
$E_{s,xy}$	$\sqrt{3}lm(sd\sigma)$
E_{s,x^2-y^2}	$\frac{1}{2}\sqrt{3}(l^2 - m^2)(sd\sigma)$
$E_{s,3z^2-r^2}$	$[n^2 - \frac{1}{2}(l^2 + m^2)](sd\sigma)$
$E_{x,xy}$	$\sqrt{3}l^2m(pd\sigma) + m(1 - 2l^2)(pd\pi)$
$E_{x,yz}$	$\sqrt{3}lmn(pd\sigma) - 2lmn(pd\pi)$
$E_{x,zx}$	$\sqrt{3}l^2n(pd\sigma) + n(1 - 2l^2)(pd\pi)$
E_{x,x^2-y^2}	$\frac{1}{2}\sqrt{3}l(l^2 - m^2)(pd\sigma) + l(1 - l^2 + m^2)(pd\pi)$
E_{y,x^2-y^2}	$\frac{1}{2}\sqrt{3}m(l^2 - m^2)(pd\sigma) - m(1 + l^2 - m^2)(pd\pi)$
E_{z,x^2-y^2}	$\frac{1}{2}\sqrt{3}n(l^2 - m^2)(pd\sigma) - n(l^2 - m^2)(pd\pi)$
$E_{x,3z^2-r^2}$	$l[n^2 - \frac{1}{2}(l^2 + m^2)](pd\sigma) - l\sqrt{3}n^2(pd\pi)$
$E_{y,3z^2-r^2}$	$m[n^2 - \frac{1}{2}(l^2 + m^2)](pd\sigma) - \sqrt{3}mn^2(pd\pi)$
$E_{z,3z^2-r^2}$	$n[n^2 - \frac{1}{2}(l^2 + m^2)](pd\sigma) + \sqrt{3}n(l^2 + m^2)(pd\pi)$
$E_{xy,xy}$	$3l^2m^2(dd\sigma) + (l^2 + m^2 - 4l^2m^2)(dd\pi) + (n^2 + l^2m^2)(dd\delta)$
$E_{xy,yz}$	$3lm^2n(dd\sigma) + nl(1 - 4m^2)(dd\pi) + nl(m^2 - 1)(dd\delta)$
$E_{xy,zx}$	$3l^2mn(dd\sigma) + mn(1 - 4l^2)(dd\pi) + mn(l^2 - 1)(dd\delta)$
E_{xy,x^2-y^2}	$\frac{3}{2}lm(l^2 - m^2)(dd\sigma) + 2lm(m^2 - l^2)(dd\pi) + \frac{1}{2}lm(l^2 - m^2)(dd\delta)$

E_{yz,x^2-y^2}	$\frac{3}{2}mn(l^2 - m^2)(dd\sigma) - mn[1 + 2(l^2 - m^2)](dd\pi)$ $+ mn[1 + \frac{1}{2}(l^2 - m^2)](dd\delta)$
E_{zx,x^2-y^2}	$\frac{3}{2}nl(l^2 - m^2)(dd\sigma) + nl[1 - 2(l^2 - m^2)](dd\pi)$ $- nl[1 - \frac{1}{2}(l^2 - m^2)](dd\delta)$
$E_{xy,3z^2-r^2}$	$\sqrt{3}lm[n^2 - \frac{1}{2}(l^2 + m^2)](dd\sigma) - 2\sqrt{3}lmn^2(dd\pi) + \frac{1}{2}\sqrt{3}lm(1 + n^2)(dd\delta)$
$E_{yz,3z^2-r^2}$	$\sqrt{3}mn[n^2 - \frac{1}{2}(l^2 + m^2)](dd\sigma) + \sqrt{3}mn(l^2 + m^2 - n^2)(dd\pi)$ $- \frac{1}{2}\sqrt{3}mn(l^2 + m^2)(dd\delta)$
$E_{zx,3z^2-r^2}$	$\sqrt{3}nl[n^2 - \frac{1}{2}(l^2 + m^2)](dd\sigma) + \sqrt{3}nl(l^2 + m^2 - n^2)(dd\pi)$ $- \frac{1}{2}\sqrt{3}nl(l^2 + m^2)(dd\delta)$
$E_{x^2-y^2,x^2-y^2}$	$\frac{3}{4}(l^2 - m^2)^2(dd\sigma) + [l^2 + m^2 - (l^2 - m^2)^2](dd\pi)$ $+ [n^2 + \frac{1}{4}(l^2 - m^2)^2](dd\delta)$
$E_{x^2-y^2,3z^2-r^2}$	$\frac{1}{2}\sqrt{3}(l^2 - m^2)[n^2 - \frac{1}{2}(l^2 + m^2)](dd\sigma) + \sqrt{3}n^2(m^2 - l^2)(dd\pi)$ $+ \frac{1}{4}\sqrt{3}(1 + n^2)(l^2 - m^2)(dd\delta)$
$E_{3z^2-r^2,3z^2-r^2}$	$[n^2 - \frac{1}{2}(l^2 + m^2)]^2(dd\sigma) + 3n^2(l^2 + m^2)(dd\pi) + \frac{3}{4}(l^2 + m^2)^2(dd\delta)$

§3.2 Valence force field model

Phonon^{56,63} is a kind of elementary excitation in solid, and it describes small vibrations of lattice. Lattice dynamics⁶³ is the theory of calculating phonons.

3.2.1 Lattice dynamics⁶⁴

At first for the sake of simplicity we consider a simple lattice that includes only one atom in one unit cell, and then we generalize the discussion to compound lattice which includes several atoms in one unit cell.

Assuming the vibrations in lattice are very small, the total potential energy is expanded as:

$$\Phi = \Phi_0 + \sum_{l,\alpha} \Phi_\alpha(l) u_l^\alpha + \frac{1}{2} \sum_{l,\alpha} \sum_{l',\beta} \Phi_{\alpha\beta}(l,l') u_l^\alpha u_{l'}^\beta + \dots \quad (3.2.1)$$

Where u_l^α is the displacement of atom l along direction α (x, y, z). Φ_0 is the potential energy of equilibrium geometry, so it's a constant. At equilibrium the potential should be minimum:

$$\Phi_\alpha(l) = \left(\frac{\partial \Phi}{\partial u_l^\alpha} \right)_{equilibrium} = 0 \quad (3.2.2)$$

The second derivative of potential energy is:

$$\Phi_{\alpha\beta}(l,l') = \left(\frac{\partial^2 \Phi}{\partial u_l^\alpha \partial u_{l'}^\beta} \right)_0 = \Phi_{\beta\alpha}(l',l) = \Phi_{\alpha\beta}(l-l') = \Phi_{\beta\alpha}(l'-l) \quad (3.2.3)$$

Where the second equation comes from the commutativity of second derivative and the last two equations are due to the translation invariance of lattice.

For a compound lattice that includes n atoms in one unit cell, the secular equation of phonon is:

$$\sum_{\beta,s'} D_{\alpha\beta} \begin{pmatrix} k \\ s, s' \end{pmatrix} e_k^\beta(s') = \omega^2 e_k^\alpha(s) \quad (3.2.4)$$

Where s and s' are atom indexes ($1, \dots, n$), and the squared frequency ω^2 is

determined by:

$$\det \left\| D_{\alpha\beta} \begin{pmatrix} k \\ s, s' \end{pmatrix} - \omega^2 \delta_{\alpha\beta} \delta_{ss'} \right\| = 0 \quad (3.2.5)$$

Solving Eq.3.2.5 is a problem of $3n \times 3n$ Matrix diagonalisation which can be carried out by ‘zheev’ (a standard procedure in Lapack package). In Eq.3.2.4 and Eq.3.2.5, the definition of dynamical matrix $D_{\alpha\beta}$ is:

$$D_{\alpha\beta} \begin{pmatrix} k \\ s, s' \end{pmatrix} \equiv \frac{1}{\sqrt{M_s M_{s'}}} \sum_l \Phi_{\alpha\beta} \begin{pmatrix} l \\ s, s' \end{pmatrix} e^{-ik \cdot R_l} \quad (3.2.6)$$

Where the force-constant matrix $\Phi_{\alpha\beta}$ is defined as:

$$\Phi_{\alpha\beta} \begin{pmatrix} l-l' \\ s, s' \end{pmatrix} \equiv \left(\frac{\partial^2 \Phi}{\partial u_l^\alpha(s) \partial u_{l'}^\beta(s')} \right)_0 \quad (3.2.7)$$

In Eq.3.2.7, $u_l^\alpha(s)$ denotes the displacement of atom s in unit cell l along direction α . Solving Eq.3.2.5, there should be $3n$ eigenfrequencies:

$$\omega = \omega_\sigma(k), \quad (\sigma = 1, \dots, 3n) \quad (3.2.9)$$

and each eigenfrequency corresponds to an eigenvector $e_{k\sigma}(s)$. The displacement of atom s in unit cell l is:

$$u_l(s) = \frac{1}{\sqrt{NM_s}} \sum_{k,\sigma} e_{k\sigma}(s) Q_{k\sigma} e^{ik \cdot R_l} \quad (3.2.10)$$

Where M_s is the mass of atom s and $Q_{k\sigma}$ is called normal coordinate.

3.2.2 Calculation method

Phonons can be calculated by ab-initio method⁶⁵ or empirical potential method⁵². Main differences of these methods lie in the way how to construct the force-constant matrix and dynamical matrix. So far, there are two kinds of ab-initio methods. One is called frozen-phonon approximation (FPA) super-cell method⁶⁶ and the other is called density functional perturbation theory⁶⁵ (DFPT). The FPA super-cell method involves perturbing the positions of atoms slightly and calculating the reaction forces, so it is

necessary to use supercells of the original cell when interatomic interaction is long ranged. It is a big difficulty when the super-cell is large because of costly calculation. The DFPT method uses linear response calculations to evaluate the dynamical matrix directly for a set of q-vectors. The starting point of the DFPT approach is the evaluation of the second-order change in the total energy induced by atomic displacements. However, these ab-initio methods are too expensive to calculate the phonon spectra of SiNW. As a result, we use the empirical potential method to calculate the phonons of SiNW in this thesis.

There are a lot of empirical potential models. As the name implies, an empirical potential model assumes the analytical form of crystal potential energy Φ directly. The parameters in the analytical expression of potential energy are fitted to experimental data. One of the most famous empirical potential models is called ‘keating model’ which was broached by Keating in 1966^{50,51}. Vanderbilt⁵² *et al.* generalized the keating model and studied the anharmonic elastic and phononic properties of diamond-structure silicon successfully. We adopt this generalized keating model in our work and introduce it in the next subsection.

3.2.3 VFF model

The generalized keating model⁵² proposed by Vanderbilt *et al.* is a kind of VFF model that involves contributions of bond stretch, bond angle bend, torsion and inversion. To describe accurately the anharmonic elastic properties of silicon, Vanderbilt *et al.* expanded the potential energy of crystal to the fourth-order as follow:

$$h_{ii} \equiv x_i^2 / a_K^2 - 3 \quad (3.2.11)$$

$$h_{ij} \equiv (x_i \cdot x_j + x_i^2 / 6 + x_j^2 / 6) / a_K^2 \quad (3.2.12)$$

$$\begin{aligned} \Phi^{[2]} = & \sum_i \frac{1}{2} k_{rr} h_{ii}^2 + \sum_{(i<j)} \left[\frac{1}{2} k_{\theta\theta} h_{ij}^2 + k_{r\theta} (h_{ii} + h_{jj}) h_{ij} + k_{rr} h_{ii} h_{jj} \right] \\ & + \sum_{(i<j<k)} k_{\theta\theta'} (h_{ij} h_{ik} + h_{ij} h_{jk} + h_{ik} h_{jk}) + \sum_{(i;j<k)} k_{\theta\theta''} h_{ij} h_{ik} \end{aligned} \quad (3.2.13)$$

$$\begin{aligned} \Phi^{[3]} = & \sum_i \frac{1}{6} k_{rrr} h_{ii}^3 + \sum_{(i<j)} \left[\frac{1}{2} k_{rr\theta} (h_{ii}^2 + h_{jj}^2) h_{ij} + \frac{1}{2} k_{r\theta\theta} (h_{ii} + h_{jj}) h_{ij}^2 + \frac{1}{6} k_{\theta\theta\theta} h_{ij}^3 \right. \\ & \left. + \frac{1}{2} k_{rrr'} (h_{ii} + h_{jj}) h_{ii} h_{jj} + k_{rr'\theta} h_{ii} h_{jj} h_{ij} \right] \end{aligned} \quad (3.2.14)$$

$$\begin{aligned} \Phi^{[4]} = & \sum_i \frac{1}{24} k_{rrrr} h_{ii}^4 + \sum_{(i<j)} \left[\frac{1}{6} k_{rrr\theta} (h_{ii}^3 + h_{jj}^3) h_{ij} + \frac{1}{4} k_{rr\theta\theta} (h_{ii}^2 + h_{jj}^2) h_{ij}^2 \right. \\ & + \frac{1}{6} k_{r\theta\theta\theta} (h_{ii} + h_{jj}) h_{ij}^3 + \frac{1}{24} k_{\theta\theta\theta\theta} h_{ij}^4 + \frac{1}{6} k_{rrr'} (h_{ii}^2 + h_{jj}^2) h_{ii} h_{jj} \\ & \left. + \frac{1}{4} k_{rr'r'} h_{ii}^2 h_{jj}^2 + \frac{1}{2} k_{rrr'\theta} (h_{ii} + h_{jj}) h_{ii} h_{jj} h_{ij} + \frac{1}{2} k_{rr'\theta\theta} h_{ii} h_{jj} h_{ij}^2 \right] \end{aligned} \quad (3.2.15)$$

Here, i and j label nearest-neighbor bonds (NBB), x_i is the ‘bond vector’ pointing from one atom to its neighbor, and $a_K = a/4$ (a is lattice constant). ($i < j$) indicates a sum over all pairs of NBBs sharing an atom, ($i < j < k$) indicates a sum over triplets of NBBs sharing an atom, and ($i; j < k$) represents a sum over chains of three NBBs arranged end to end, with i sharing one of its atoms with j and the other with k , in a 180° dihedral-angle configuration. The superscript “[2]” (“[3]”, “[4]”) in Eq.3.2.13 (Eq.3.2.14, Eq.3.2.15) indicates a set of terms which are quadratic (cubic, quartic) in the variables r , θ , h_{ii} and h_{ij} . Parameters (k_{rr} , $k_{\theta\theta}$, ...) are determined from fitting the inelastic-neutron-scattering data²¹¹.

§3.3 Electron-phonon coupling theory⁶⁷

In this section, we will discuss the electron-phonon coupling in solid and derive the formula of electronic transition rate due to electron-phonon scattering.

Band theory of solid assumes an electron moves in a periodic potential. In fact, the lattice vibrates all the time. The periodicity of the potential in lattice will be broken down by the displacement of atoms from their equilibrium positions. So we

have to include the interaction between electron and lattice vibration when studying the real electron behavior. The deviation of potential from periodic case is usually denoted as a complementary field. When the deviation is small, we can use phonons to describe the vibration of lattice and use first-order perturbation theory to describe the electron-phonon coupling. For diffusion-transport regime, electron-phonon coupling is the most important factor because there are much more contributions from electron-phonon scattering than from any other scattering mechanism. From now on, we will derive the formulas of electron-phonon scattering probability and the electronic transition rate. Here we just consider one-phonon scattering processes.

First, we expand the Hamiltonian to the first-order approximation of $\bar{S}_{n\alpha i}$, which denotes the displacement of atom α in unit cell n along direction i (x, y, z).

$$H = H_0 + \sum_{n,\alpha,i} \left(\frac{\partial H}{\partial S_{n\alpha i}} \right) S_{n\alpha i} = H_0 + V \quad (3.3.1)$$

According to the lattice dynamics introduced in last section, the displacement of atom from equilibrium position reads,

$$S_{n\alpha i}(t) = \frac{1}{\sqrt{NM_\alpha}} \sum_{j\bar{q}} Q_j(\bar{q}) e_{\alpha i}^{(j)}(\bar{q}) \exp[i(\bar{q} \cdot \bar{R}_n - \omega_j(\bar{q})t)] \quad (3.3.2)$$

Here N is the number of Wigner-Seitz unit cell, M_α is the mass of atom α , \bar{R}_n is the position vector of unit cell, \bar{q} is the wave vector of phonon, j is the phonon mode, $e_{\alpha i}^{(j)}(\bar{q})$ is the element of eigenvector of phonon state $|q, j\rangle$ and $\omega_j(\bar{q})$ is the corresponding eigenfrequency.

Second, we calculate the scattering matrix element from an initial state $|0\rangle|k, b\rangle$ to a final state $| -q, j\rangle|k + q, b'\rangle$ via emitting a phonon $| -q, j\rangle$ under complementary potential field V . From second quantization,

$$Q_j(\bar{q}, t) = Q_j(\bar{q}) e^{-i\omega_j(\bar{q})t} \rightarrow Q_{\bar{q}, j} = \sqrt{\frac{\hbar}{2\omega_j(\bar{q})}} (a_{-\bar{q}, j}^+ + a_{\bar{q}, j}) \quad (3.3.3)$$

$$|k, b\rangle = \sum_{\beta, \eta} C_{\beta, \eta}^{k, b} \frac{1}{\sqrt{N}} \sum_m e^{ik \cdot R_{m\beta}} \varphi_\eta(r - R_{m\beta}) \quad (3.3.4)$$

Where \hbar is the Planck constant, a^+ is the creation operator and a is the annihilation operator, Eq.3.3.4 is an expansion of electron wave function in atomic orbital basis under tight-binding model, k is the wave vector of electron, b is the energy-band index of electron state, $C_{\beta,\eta}^{k,b}$ is the eigenvector element of tight-binding Hamiltonian H_0 , β is the atom index, η denotes different two-center integrals of tight-binding and $\varphi_\eta(r - R_{m\beta})$ is the atomic orbital. Substitute Eq.3.3.3 and Eq.3.3.4 into the transition probability of one-phonon emission $\langle k + q, b' | \langle -q, j | V | 0 \rangle | k, b \rangle$, then

$$\begin{aligned} \langle k + q, b' | \langle -q, j | V | 0 \rangle | k, b \rangle &= \sum_{\alpha,i} \frac{1}{\sqrt{NM_\alpha}} \sqrt{\frac{\hbar}{2\omega_{q,j}}} e_{\alpha i}^{(j)}(q) \sum_{\beta,\eta,\beta',\eta'} C_{\beta',\eta'}^{k+q,b'^*} C_{\beta,\eta}^{k,b} \\ &\times \sum_{m,m'} e^{ik \cdot R_{m\beta}} e^{-i(k+q) \cdot R_{m'\beta'}} \langle \varphi_{\eta'}(r - R_{m'\beta'}) | \frac{\partial H}{\partial S_{0\alpha i}} | \varphi_\eta(r - R_{m\beta}) \rangle \end{aligned} \quad (3.3.5)$$

The transition probability of one-phonon absorption $\langle k + q, b' | \langle 0 | V | q, j \rangle | k, b \rangle$ is exactly the same. In the derivation we used the following identity:

$$\sum_n e^{i(q+k-k')R_n} = N\delta_{k',k+q+K} \quad (3.3.6)$$

Where $\delta_{k',k+q+K}$ is the Kronecker delta function.

Finally, we apply the Fermi-Golden rule to calculate the transition rate or inverse of lifetime.

$$\text{Fermi-Golden rule: } W(i \rightarrow f) = \frac{2\pi}{\hbar} \sum_{i,f} p(i) |\langle final | V | initial \rangle|^2 \delta(E_f - E_i) \quad (3.3.7)$$

Substitute Eq.3.3.5 into Eq.3.3.7, the electronic transition rate reads

$$\begin{aligned} W_{q,j}(|k, b \rangle \rightarrow |k + q, b' \rangle) &= \frac{2\pi}{\hbar} |\langle k + q, b' | \langle -q, j | V | 0 \rangle | k, b \rangle|^2 \times \\ &\{n(q, j)\delta(E_{k+q,b'} - E_{k,b} - \hbar\omega_{q,j}) + (n(q, j) + 1)\delta(E_{k+q,b'} - E_{k,b} + \hbar\omega_{q,j})\} \end{aligned} \quad (3.3.10)$$

Where $n(q, j)$ is the Bose-Einstein distribution function of phonons.

Chapter 4 Programming

In programming, we will meet a lot of questions like ‘how to construct the electronic Hamiltonian’, ‘how to construct the dynamical matrix’, ‘how to calculate the transition rate’ and so on. We give answers to these questions in this chapter. The formulas and algorithms employed by the code are introduced.

§4.1 Outline of the code

There are six parts of the code: (1) atomic structure of SiNW, (2) eigenvalue and eigenvector of electronic Hamiltonian, (3) phonon spectra and vibration mode, (4) electron-phonon transition rate, (5) electron mobility, (6) data processing. This section will introduce each part briefly.

The first part of the code produces the atomic coordinates of atoms in the origin unit cell of SiNW with Cartesian coordinate system. We use angstrom as unit of length. In the code, first we cut a silicon crystal lattice along an orientation with a fixed radius. Second search the silicon atoms who have dangling bonds. Third, hydrogen atoms are connected to the open ends of dangling bonds to passivate the surface. At last, the code searches the nearest neighbors and second-nearest neighbors of each atom in the unit cell, and stores the nearest-neighbor list and second-nearest-neighbor list into arrays.

The second part of the code includes the generation of wave vectors in the first Brillouin zone, construction of Hamiltonian, calculation of eigenvalues and eigenvectors. The wave vector is 1-dimensional for SiNW and it is determined

according to the orientation of SiNW. We use $sp^3d^5s^*$ tight-binding model^{48,61,68} to construct the electronic Hamiltonian matrix. It means that there are ten atomic orbitals ($s, p_x, p_y, p_z, d_{yz}, d_{zx}, d_{xy}, d_{x^2-y^2}, d_{3z^2-r^2}, s^*$) per silicon and one atomic orbital (s) per hydrogen. The dimension of Hamiltonian matrix should be $(10N_{Si} + N_H) \times (10N_{Si} + N_H)$ without spin-orbit coupling and $2(10N_{Si} + N_H) \times 2(10N_{Si} + N_H)$ with spin-orbit coupling. Eigenvalues and eigenvectors are obtained by solving the following secular equation

$$H\psi = E\psi \quad (4.1.1)$$

Here H is the Hamiltonian matrix, ψ is the eigenvector, and E is the eigenvalue. Linear algebra told us solving secular equation is equivalent to diagonalisation of Hamiltonian matrix. After diagonalisation the Hamiltonian matrix is transformed to a diagonal matrix whose diagonal elements are eigenvalues and the columns of transfer matrix are eigenvectors. There are a lot of methods to diagonalize a square matrix. Here we use two different methods. One is ‘LU’ decomposition method and the other is conjugate-gradient iterative method (CG). LU method is a direct method and can be used to diagonalize any square matrix in principle, but the LU decomposition is costly in computation when the matrix is large. CG method is an iterative method and it is especially suitable to the diagonalisation of large sparse matrix. The advantage of CG method is fast, but the disadvantage is only several eigenvalues and eigenvectors could be obtained. In the code, LU method and CG method are implemented into modules ‘diag_zheev’ and ‘diag_cg’ separately, and either LU method or CG method can be used according to need.

The third part of the code consists of calculation of force constant, construction and diagonalisation of dynamical matrix. From Eq.3.2.7, the force constant matrix element is the second derivative of potential energy according to the displacement of atom. The dynamical matrix is constructed from Eq.3.2.6. We use ‘diag_zheev’ to diagonalize the dynamical matrix because the eigenvalues are heavy degenerate and it is difficult to deal with by ‘diag_cg’. It will need the complete phonon spectra to

calculate the electron transition probability, so 'diag_zheev' is suitable.

The fourth part of the code solves the equation of energy conservation and calculates the derivative of Hamiltonian, the scattering matrix element and the transition rate. Both the energy and momentum of electron change when the electron absorbs or emits a phonon to jump to another state, but the total energy and the total momentum keep invariance. The conservation of momentum is ensured by the Kronecker delta function (Eq.3.3.6). The conservation of energy is implied by Dirac delta function (Eq.3.3.8). However, the Dirac delta function tends to infinity when the energy is conserved. It's difficult to use Dirac delta function directly in programming. A lot of researchers use Gaussian function⁶⁹ instead of Dirac delta function because Dirac delta function is the limit of Gaussian function when the line-width of Gaussian function tends to zero. The accuracy of approximate function depends on the selection of line-width and the computation is costly. The author improved the formula of transition rate and overcame the difficulty of Dirac delta function by searching all possible electronic transitions. This improvement is analytical, so the result is accurate. Please read the fourth section of this chapter for a detailed discussion on the energy conservation. The fourth section also introduces expressions of derivative of Hamiltonian.

The fifth part of the code is in charge of simulating the electronic low-field mobility. When the applied electric field is weak, the low-field mobility can be derived directly from Boltzman transport equation (BTE) involving relaxation time approximation (RTA). Detailed derivation of low-field mobility is in the fifth section. This part of the code also involves the calculation of carrier density with respect to Fermi level.

The last part of the code collects the data such as the electronic band structure, the phonon spectra, the density of states (DOS) for phonons, the vibration mode, the electronic transition rate, the electronic low field mobility and the density of carrier. And the code outputs the data to well organized files after transforming these physical quantities into standard units.

§4.2 Programming of electronic structure

This section introduces some key aspects about the construction of $sp^3d^5s^*$ tight-binding Hamiltonian with spin-orbit coupling⁷⁰.

The structure of Hamiltonian with spin-orbit coupling is

$$\begin{bmatrix} H_{SiSi}^{\uparrow\uparrow} & H_{SiH}^{\uparrow\uparrow} & H_{SiSi}^{\uparrow\downarrow} & H_{SiH}^{\uparrow\downarrow} \\ H_{HSi}^{\uparrow\uparrow} & H_{HH}^{\uparrow\uparrow} & H_{HSi}^{\uparrow\downarrow} & H_{HH}^{\uparrow\downarrow} \\ H_{SiSi}^{\downarrow\uparrow} & H_{SiH}^{\downarrow\uparrow} & H_{SiSi}^{\downarrow\downarrow} & H_{SiH}^{\downarrow\downarrow} \\ H_{HSi}^{\downarrow\uparrow} & H_{HH}^{\downarrow\uparrow} & H_{HSi}^{\downarrow\downarrow} & H_{HH}^{\downarrow\downarrow} \end{bmatrix}$$

Here $\uparrow(\downarrow)$ represents spin-up (spin-down), subscript ‘ Si ’ and ‘ H ’ denote silicon and hydrogen separately. There is no spin-orbit coupling either for hydrogen self or between silicon and hydrogen, so $H_{HH}^{\uparrow\downarrow} = H_{HH}^{\downarrow\uparrow} = H_{SiH}^{\uparrow\downarrow} = H_{SiH}^{\downarrow\uparrow} = H_{HSi}^{\uparrow\downarrow} = H_{HSi}^{\downarrow\uparrow} = 0$.

$H_{HH}^{\uparrow\uparrow}$ and $H_{HH}^{\downarrow\downarrow}$ are diagonal matrix, and all diagonal elements are equal to the onsite energy of hydrogen E_s^H . Block matrices $H_{SiSi}^{\uparrow\uparrow}$ and $H_{SiSi}^{\downarrow\downarrow}$ are arranged in the order of silicon atoms. A block Hamiltonian matrix between any two different silicon atoms is in the form as follow:

	s	p_x	p_y	p_z	d_{yz}	d_{zx}	d_{xy}	$d_{x^2-y^2}$	$d_{3z^2-r^2}$	s^*
s	H_{ss}	H_{sp_x}	H_{sp_y}	H_{sp_z}	$H_{sd_{yz}}$	$H_{sd_{zx}}$	$H_{sd_{xy}}$	$H_{sd_{x^2-y^2}}$	$H_{sd_{3z^2-r^2}}$	H_{ss}^*
p_x	$H_{p_x s}$	$H_{p_x p_x}$	$H_{p_x p_y}$	$H_{p_x p_z}$	$H_{p_x d_{yz}}$	$H_{p_x d_{zx}}$	$H_{p_x d_{xy}}$	$H_{p_x d_{x^2-y^2}}$	$H_{p_x d_{3z^2-r^2}}$	$H_{p_x s}^*$
p_y	$H_{p_y s}$	$H_{p_y p_x}$	$H_{p_y p_y}$	$H_{p_y p_z}$	$H_{p_y d_{yz}}$	$H_{p_y d_{zx}}$	$H_{p_y d_{xy}}$	$H_{p_y d_{x^2-y^2}}$	$H_{p_y d_{3z^2-r^2}}$	$H_{p_y s}^*$
p_z	$H_{p_z s}$	$H_{p_z p_x}$	$H_{p_z p_y}$	$H_{p_z p_z}$	$H_{p_z d_{yz}}$	$H_{p_z d_{zx}}$	$H_{p_z d_{xy}}$	$H_{p_z d_{x^2-y^2}}$	$H_{p_z d_{3z^2-r^2}}$	$H_{p_z s}^*$
d_{yz}	$H_{d_{yz} s}$	$H_{d_{yz} p_x}$	$H_{d_{yz} p_y}$	$H_{d_{yz} p_z}$	$H_{d_{yz} d_{yz}}$	$H_{d_{yz} d_{zx}}$	$H_{d_{yz} d_{xy}}$	$H_{d_{yz} d_{x^2-y^2}}$	$H_{d_{yz} d_{3z^2-r^2}}$	$H_{d_{yz} s}^*$
d_{zx}	$H_{d_{zx} s}$	$H_{d_{zx} p_x}$	$H_{d_{zx} p_y}$	$H_{d_{zx} p_z}$	$H_{d_{zx} d_{yz}}$	$H_{d_{zx} d_{zx}}$	$H_{d_{zx} d_{xy}}$	$H_{d_{zx} d_{x^2-y^2}}$	$H_{d_{zx} d_{3z^2-r^2}}$	$H_{d_{zx} s}^*$
d_{xy}	$H_{d_{xy} s}$	$H_{d_{xy} p_x}$	$H_{d_{xy} p_y}$	$H_{d_{xy} p_z}$	$H_{d_{xy} d_{yz}}$	$H_{d_{xy} d_{zx}}$	$H_{d_{xy} d_{xy}}$	$H_{d_{xy} d_{x^2-y^2}}$	$H_{d_{xy} d_{3z^2-r^2}}$	$H_{d_{xy} s}^*$
$d_{x^2-y^2}$	$H_{d_{x^2-y^2} s}$	$H_{d_{x^2-y^2} p_x}$	$H_{d_{x^2-y^2} p_y}$	$H_{d_{x^2-y^2} p_z}$	$H_{d_{x^2-y^2} d_{yz}}$	$H_{d_{x^2-y^2} d_{zx}}$	$H_{d_{x^2-y^2} d_{xy}}$	$H_{d_{x^2-y^2} d_{x^2-y^2}}$	$H_{d_{x^2-y^2} d_{3z^2-r^2}}$	$H_{d_{x^2-y^2} s}^*$
$d_{3z^2-r^2}$	$H_{d_{3z^2-r^2} s}$	$H_{d_{3z^2-r^2} p_x}$	$H_{d_{3z^2-r^2} p_y}$	$H_{d_{3z^2-r^2} p_z}$	$H_{d_{3z^2-r^2} d_{yz}}$	$H_{d_{3z^2-r^2} d_{zx}}$	$H_{d_{3z^2-r^2} d_{xy}}$	$H_{d_{3z^2-r^2} d_{x^2-y^2}}$	$H_{d_{3z^2-r^2} d_{3z^2-r^2}}$	$H_{d_{3z^2-r^2} s}^*$
s^*	$H_{s s}$	$H_{s p_x}$	$H_{s p_y}$	$H_{s p_z}$	$H_{s d_{yz}}$	$H_{s d_{zx}}$	$H_{s d_{xy}}$	$H_{s d_{x^2-y^2}}$	$H_{s d_{3z^2-r^2}}$	$H_{s s}^*$

Element in the block is calculated by formula

$$H_{ij,\sigma} = \sum_{\langle R_l+r_j \rangle} e^{ik \cdot (R_l+r_j-r_i)} E_{\sigma}(r_i, R_l+r_j)$$

Here $\langle R_l+r_j \rangle$ denotes the summation over all nearest neighbors of atom i , σ denotes the type of coupling between atomic orbitals like ss , sp_x , sp_y , sp_z , sd_{yz} , sd_{zx} , sd_{xy} , $sd_{x^2-y^2}$, $sd_{3z^2-r^2}$, ss^* and so on.

H_{ii} is the diagonal block of Hamiltonian for the same silicon atom. The onsite energies are E_s^{Si} , E_p^{Si} , E_d^{Si} and $E_{s^*}^{Si}$ separately.

The form of spin-orbit coupling is as follows:

	$p_x \uparrow$	$p_y \uparrow$	$p_z \uparrow$	$p_x \downarrow$	$p_y \downarrow$	$p_z \downarrow$
$p_x \uparrow$		$-i\frac{\Delta}{3}$				$+\frac{\Delta}{3}$
$p_y \uparrow$	$+i\frac{\Delta}{3}$					$-i\frac{\Delta}{3}$
$p_z \uparrow$				$-\frac{\Delta}{3}$	$+i\frac{\Delta}{3}$	
$p_x \downarrow$			$-\frac{\Delta}{3}$		$+i\frac{\Delta}{3}$	
$p_y \downarrow$			$-i\frac{\Delta}{3}$	$-i\frac{\Delta}{3}$		
$p_z \downarrow$	$+\frac{\Delta}{3}$	$+i\frac{\Delta}{3}$				

Where Δ is called the spin-orbit coupling parameter. It's worth noting that the off-diagonal blocks $H_{SiSi}^{\uparrow\downarrow}$ and $H_{SiSi}^{\downarrow\uparrow}$ become nonzero because of the spin-orbit coupling.

Jancu *et al.* introduced a series of deformation-potential parameters n_{σ} into two-center integrals of $sp^3d^5s^*$ tight-binding model to describe the effect of bond length.

$$V_{\sigma}(d) = V_{\sigma}(d_0) \cdot \left(\frac{d}{d_0} \right)^{n_{\sigma}} \quad (4.2.1)$$

Here V_{σ} represents a two-center integral, σ is the type of integral like $ss\sigma$, $sp\sigma$,

$pp\sigma$, $pp\pi$, $sd\sigma$, $s^*p\sigma$, $pd\sigma$, $pd\pi$ and so on.

We construct the block Hamiltonian $\uparrow\uparrow$ and copy it to the block $\downarrow\downarrow$, and then we add the spin-orbit coupling into Hamiltonian. In practice, we only construct the up-triangular of Hamiltonian matrix because Hamiltonian matrix is Hermitian. We put the line index and row index of every nonzero element into arrays at the time of constructing Hamiltonian, and then we store Hamiltonian matrix in sparse form.

§4.3 Programming of phononic structure

We have introduced the Vanderbilt's VFF model⁵² in last chapter. The second-order approximation of potential energy is as follows:

$$\begin{aligned} \Phi^{[2]} = & \sum_i \frac{1}{2} k_{rr} h_{ii}^2 + \sum_{(i<j)} \left[\frac{1}{2} k_{\theta\theta} h_{ij}^2 + k_{r\theta} (h_{ii} + h_{jj}) h_{ij} + k_{rr'} h_{ii} h_{jj} \right] \\ & + \sum_{(i<j<k)} k_{\theta\theta'} (h_{ij} h_{ik} + h_{ij} h_{jk} + h_{ik} h_{jk}) + \sum_{(i;j<k)} k_{\theta\theta^*} h_{ij} h_{ik} \end{aligned} \quad (4.3.1)$$

$$h_{ii} \equiv x_i^2 / a_K^2 - 3$$

$$h_{ij} \equiv (x_i \cdot x_j + x_i^2 / 6 + x_j^2 / 6) / a_K^2$$

Here i , j and k are chemical bonds between nearest-neighbor atoms, x_i denotes the vector of bond i , $a_K = a/4$, a is the lattice constant, $(i < j)$ indicates a sum over all pairs of nearest-neighbor bonds sharing an atom, $(i < j < k)$ indicates a sum over triplets of nearest-neighbor bonds sharing an atom, and $(i; j < k)$ indicates a sum over chains of three nearest-neighbor bonds arranged end to end, with i sharing one of its atoms with j and the other with k , in a 180° dihedral-angle configuration. The values of k_{rr} , $k_{\theta\theta}$, $k_{r\theta}$, $k_{rr'}$, $k_{\theta\theta'}$ and $k_{\theta\theta^*}$ are from Ref.20.

The element of force constant matrix is the second derivative of potential energy. The formula is as follows.

$$\begin{aligned}
\Phi_{l\alpha,l'\beta} \equiv \frac{\partial^2 \Phi^{[2]}}{\partial \alpha_l \partial \beta_{l'}} &= \sum_i \frac{1}{2} k_{rr} \frac{\partial^2 h_{ii}^2}{\partial \alpha_l \partial \beta_{l'}} + \sum_{(i<j)} \left[\frac{1}{2} k_{\theta\theta} \frac{\partial^2 h_{ij}^2}{\partial \alpha_l \partial \beta_{l'}} + k_{r\theta} \left(\frac{\partial^2 h_{ii} h_{ij}}{\partial \alpha_l \partial \beta_{l'}} + \frac{\partial^2 h_{jj} h_{ij}}{\partial \alpha_l \partial \beta_{l'}} \right) \right. \\
&\quad \left. + k_{rr'} \frac{\partial^2 h_{ii} h_{jj}}{\partial \alpha_l \partial \beta_{l'}} \right] + \sum_{(i<j<k)} k_{\theta\theta'} \left[\frac{\partial^2 h_{ij} h_{ik}}{\partial \alpha_l \partial \beta_{l'}} + \frac{\partial^2 h_{ij} h_{jk}}{\partial \alpha_l \partial \beta_{l'}} + \frac{\partial^2 h_{ik} h_{jk}}{\partial \alpha_l \partial \beta_{l'}} \right] + \sum_{(i;j<k)} k_{\theta\theta^*} \frac{\partial^2 h_{ij} h_{ik}}{\partial \alpha_l \partial \beta_{l'}}
\end{aligned} \tag{4.3.2}$$

Where l and l' are atom indices, α and β represent coordinate x, y, z . In

order to calculate $\Phi_{l\alpha,l'\beta}$ we need to derive the expressions of $\frac{\partial^2 h_{ii}^2}{\partial \alpha_l \partial \beta_{l'}}$, $\frac{\partial^2 h_{ij}^2}{\partial \alpha_l \partial \beta_{l'}}$,

$\frac{\partial^2 h_{ii} h_{ij}}{\partial \alpha_l \partial \beta_{l'}}$ and so on. We take $\frac{\partial^2 h_{ii}^2}{\partial \alpha_l \partial \beta_{l'}}$ as an example,

$$\begin{aligned}
\frac{\partial^2 h_{ii}^2}{\partial \alpha_l \partial \beta_{l'}} &= \frac{\partial}{\partial \beta_{l'}} \left(2h_{ii} \frac{\partial h_{ii}}{\partial \alpha_l} \right) = 2 \left(\frac{\partial h_{ii}}{\partial \alpha_l} \frac{\partial h_{ii}}{\partial \beta_{l'}} + h_{ii} \frac{\partial^2 h_{ii}}{\partial \alpha_l \partial \beta_{l'}} \right) = 2 \frac{\partial h_{ii}}{\partial \alpha_l} \frac{\partial h_{ii}}{\partial \beta_{l'}} = \\
&2 \left(2 \frac{(\alpha_l - \alpha_{i2})}{a_K^2} \delta_{l,i1} + 2 \frac{(\alpha_{i1} - \alpha_l)}{a_K^2} \delta_{l,i2} \right) \cdot \left(2 \frac{(\beta_{l'} - \beta_{i2})}{a_K^2} \delta_{l',i1} + 2 \frac{(\beta_{i1} - \beta_{l'})}{a_K^2} \delta_{l',i2} \right)
\end{aligned} \tag{4.3.3}$$

Here we use the relation $h_{ii}|_{equilibrium} = 0$, $i1$ and $i2$ denote the two atoms of bond 'i'.

It's worth noting that the last term in second derivative of potential energy, i.e.

$\sum_{(i;j<k)} k_{\theta\theta^*} h_{ij} h_{ik}$, involves four atoms and three bonds, so the list of second-nearest neighbors is needed in the calculation.

§4.4 Electron-phonon scattering matrix

This section introduces how to calculate electron-phonon scattering matrix and how to deal with the divergence of Dirac delta function.

4.4.1 Electron-phonon scattering matrix element

When electron transits from one state to another by absorbing or emitting a

phonon, the transition probability or so-called scattering matrix element is

$$\begin{aligned}
M_{q,j}^{k,b,b'} = & \sum_{\alpha,i} \frac{1}{\sqrt{NM_\alpha}} \sqrt{\frac{\hbar}{2\omega_{q,j}}} e_{\alpha i}^{(j)}(q) \sum_{\beta,\eta,\beta',\eta'} C_{\beta',\eta'}^{k+q,b'^*} C_{\beta,\eta}^{k,b} \\
& \times \sum_{m,m'} e^{ik \cdot R_{m,\beta}} e^{-i(k+q) \cdot R_{m',\beta'}} \langle \varphi_{\eta'}(r - R_{m',\beta'}) | \frac{\partial H}{\partial S_{0\alpha i}} | \varphi_{\eta}(r - R_{m\beta}) \rangle
\end{aligned} \tag{4.4.1}$$

Where N is the number of Wigner-Seitz cell, M_α is the mass of atom α , $M_{q,j}^{k,b,b'}$ is the scattering matrix element of electronic transition from initial state $|k,b\rangle$ to final state $|k+q,b'\rangle$ by absorbing a phonon $|q,j\rangle$ or emitting a phonon $| -q,j\rangle$, $\omega_{q,j}$ is the angular frequency of phonon, $e_{\alpha i}^{(j)}(q)$ is the element of phonon eigenvector, i denotes the coordinate direction, α and β denote atom indices, $C_{\beta,\eta}^{k,b}$ is the element of electronic eigenvector of state $|k,b\rangle$, η denotes the type of atomic orbital ($s^\uparrow s^\downarrow$, $p_x^\downarrow d_{x^2-y^2}^\uparrow$, ...), $R_{m,\beta}$ is the coordinate of atom β in unit cell m , $S_{0\alpha i}$ is the component of displacement of atom α in unit cell 0 along direction i .

From Eq.4.4.1, it is necessary to calculate the derivative of Hamiltonian $\frac{\partial H}{\partial S_{0\alpha i}}$.

Dr. Y. M. Niquet improved the on-site block of $sp^3d^5s^*$ tight-binding Hamiltonian in order to describe the deformation potential more accurately. A detailed discussion about Niquet's model is in appendix A. Thanks to the Hermitian of Hamiltonian, we just need the expressions for derivatives of up-triangular elements and off-diagonal elements, so there are 166 explicit expressions employed by the code. For the sake of

clearness, here we take the expression of $\frac{\partial E_s^i}{\partial \alpha_{j'}}$ as an example,

$$E_s^i = E_s^0 + \frac{3}{4} \alpha_s \sum_j \frac{d_{ij} - d_0}{d_0}, \quad d_{ij} = \sqrt{(x_i - x_j)^2 + (y_i - y_j)^2 + (z_i - z_j)^2} \tag{4.4.2}$$

1) if atom i is in the unit cell 0, then

$$\frac{\partial E_s^i}{\partial x_{j'}} = \begin{cases} \frac{3}{4} \alpha_s \frac{x_{j'} - x_i}{d_{ij'}^2} & , j' \in \{j\} \\ \frac{3}{4} \alpha_s \sum_j^{N.N.} \frac{-(x_j - x_i)}{d_{ij}^2} & , j' = i \\ 0 & , j' \notin \{i, \{j\}\} \end{cases}$$

$$\frac{\partial E_s^i}{\partial y_{j'}} = \begin{cases} \frac{3}{4} \alpha_s \frac{y_{j'} - y_i}{d_{ij'}^2} & , j' \in \{j\} \\ \frac{3}{4} \alpha_s \sum_j^{N.N.} \frac{-(y_j - y_i)}{d_{ij}^2} & , j' = i \\ 0 & , j' \notin \{i, \{j\}\} \end{cases}$$

$$\frac{\partial E_s^i}{\partial z_{j'}} = \begin{cases} \frac{3}{4} \alpha_s \frac{z_{j'} - z_i}{d_{ij'}^2} & , j' \in \{j\} \\ \frac{3}{4} \alpha_s \sum_j^{N.N.} \frac{-(z_j - z_i)}{d_{ij}^2} & , j' = i \\ 0 & , j' \notin \{i, \{j\}\} \end{cases}$$

Here $\{j\}$ denotes the set of nearest neighbor of atom i , and $N.N.$ is the abbreviation of ‘nearest neighbor’.

2) if atom i is in the unit cell ± 1 , then

$$\frac{\partial E_s^i}{\partial x_{j'}} = \begin{cases} 0 & , j' \notin \{j\} \\ \frac{3}{4} \alpha_s \frac{x_{j'} - x_i}{d_{ij'}^2} & , j' \in \{j\} \end{cases}$$

$$\frac{\partial E_s^i}{\partial y_{j'}} = \begin{cases} 0 & , j' \notin \{j\} \\ \frac{3}{4} \alpha_s \frac{y_{j'} - y_i}{d_{ij'}^2} & , j' \in \{j\} \end{cases}$$

$$\frac{\partial E_s^i}{\partial z_{j'}} = \begin{cases} 0 & , j' \notin \{j\} \\ \frac{3}{4} \alpha_s \frac{z_{j'} - z_i}{d_{ij'}^2} & , j' \in \{j\} \end{cases}$$

The other expressions are derived similarly and included in the code already. If it is necessary to use Boykin’s model or Jancu’s model, one just needs to change the parameters and set $\alpha_{s(p,d,s^*)}$, $\beta_{p(d)}$, $\gamma_{p(d)}$ to zero.

Based on phonon structure, electronic eigenvector and derivative of Hamiltonian,

the scattering matrix element can be obtained from Eq.4.4.1.

4.4.2 Energy conservation

Transition of electron is possible only under the condition of energy conservation. In the formula of electronic transition rate (Eq.3.3.10), the energy conservation is implied in the Dirac delta function $\delta(E(k+q, b') - E(k, b) \pm \hbar\omega_j(q))$. However, it's difficult to calculate Dirac delta function directly in programming, because the Dirac delta function diverges to positive infinity when the variable tends to zero. To conquer this difficulty, a lot of people use Gaussian function instead of Dirac delta function. As we know, the line shape of Gaussian function is as shown in Fig.4.4.1.

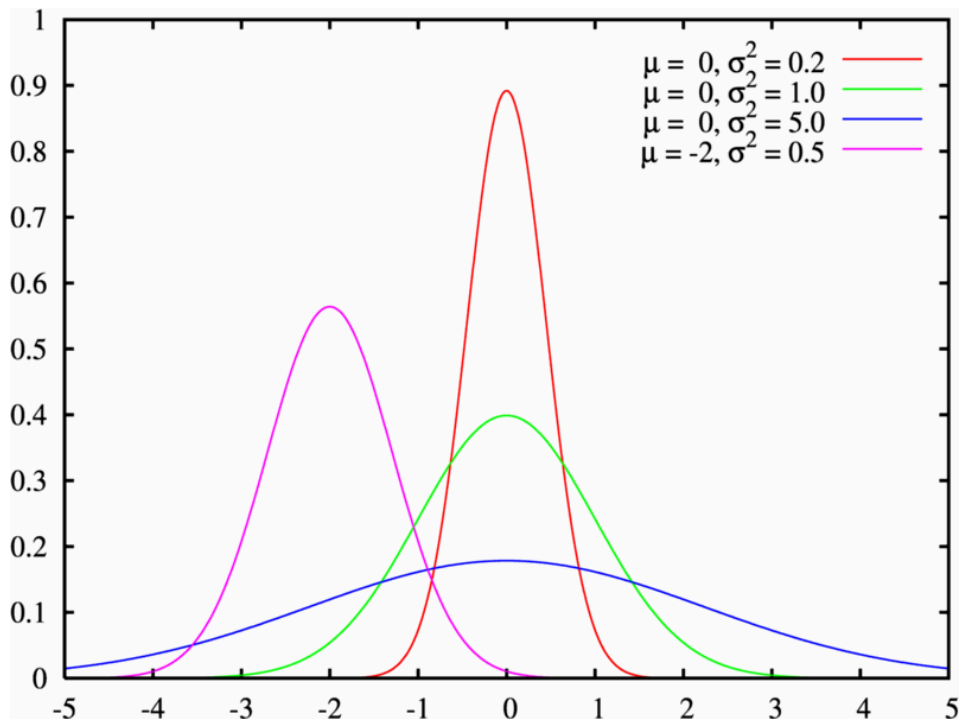


Fig.4.4.1 Line shape of Gaussian function⁶⁹, μ is the expectation and σ^2 is the variance of Gaussian function

The Gaussian function $g(x) = \frac{1}{c\sqrt{\pi}} e^{-\frac{(x-b)^2}{c^2}}$ has following properties:

- 1) $\int_{-\infty}^{+\infty} g(x) dx = 1;$
- 2) expectation: $\mu = b;$
- 3) variance: $\sigma^2 = c^2;$
- 4) $\lim_{c \rightarrow 0} g(x) = \delta(x - b).$

Parameter c is called Gaussian line width. Gaussian function tends to Dirac delta function when c decreases, and correspondingly, the computation becomes more and more expensive. Due to the large unit cell of SiNW, we have to find a more suitable and practical algorithm.

We adapted the formula of lifetime (Eq.4.5.12) as follows:

$$\begin{aligned}
\frac{1}{\tau_b(k)} &= \sum_{q,j,b'} W_{q,j}(|k,b\rangle \rightarrow |k+q,b'\rangle) \\
&= \sum_{1BZ} \sum_{j,b'} W_{q,j}(|k,b\rangle \rightarrow |k+q,b'\rangle) \\
&= \int_{-\pi/l}^{\pi/l} \frac{Nl}{2\pi} \sum_{j,b'} \frac{2\pi}{\hbar} |M_{q,j}^{k,b,b'}|^2 \times \left\{ \begin{aligned} &n_{q,j} \delta[E(k+q,b') - E(k,b) - \hbar\omega_j(q)] + \\ &(n_{q,j} + 1) \delta[E(k+q,b') - E(k,b) + \hbar\omega_j(q)] \end{aligned} \right\} dq \\
&= \sum_{i1}^{\{q,j,b'\}_1} \frac{Nl}{\hbar} \cdot \frac{|M_{q_{i1},j_{i1}}^{k,b,b'_{i1}}|^2 n_{q_{i1},j_{i1}}}{\left| \frac{\partial}{\partial q} [E(k+q,b') - E(k,b) - \hbar\omega_j(q)] \right|_{i1}} \\
&\quad + \sum_{i2}^{\{q,j,b'\}_2} \frac{Nl}{\hbar} \cdot \frac{|M_{q_{i2},j_{i2}}^{k,b,b'_{i2}}|^2 (n_{q_{i2},j_{i2}} + 1)}{\left| \frac{\partial}{\partial q} [E(k+q,b') - E(k,b) + \hbar\omega_j(q)] \right|_{i2}}
\end{aligned} \tag{4.4.3}$$

Where l is the length of unit cell, and $\{q,j,b'\}_{1(2)}$ is the set of solutions of $E(k+q,b') - E(k,b) \pm \hbar\omega_j(q) = 0$. The following property of Dirac delta function has been used in Eq.4.4.3.

$$\int_a^b f(x) \delta[g(x)] dx = \sum_i \frac{f(x_i)}{|g'(x_i)|} \tag{4.4.4}$$

Here x_i is the solution of $g(x) = 0$ and is located on the region $[a, b]$.

Obviously, it's easy to solve $E(k + q, b') - E(k, b) \pm \hbar\omega_j(q) = 0$ and to calculate

$\frac{\partial}{\partial q}[E(k + q, b') - E(k, b) \pm \hbar\omega_j(q)]$ for the code. It is worth noting that the above

transformation is analytical. We deal with the condition of energy conservation directly and explicitly. It turned out that it is accurate and fast to calculate the transition rate from Eq.4.4.3.

§4.5 Low field mobility and mean free path

In this section, we will derive the low field mobility based on the relaxation time approximation (RTA) and the boltzman transport equation⁷¹ (BTE). At last, we will introduce the formula of mean free path.

4.5.1 Low field mobility

When electrons move in electric field, the distribution function $f(k, r, t)$ is described by boltzman transport equation⁷¹ (BTE),

$$\frac{\partial f}{\partial t} = -v_k \cdot \nabla_r f(k, r, t) - \left(\frac{dk}{dt}\right) \cdot \nabla_k f(k, r, t) + \left(\frac{\partial f}{\partial t}\right)_{collision} \quad (4.5.1)$$

Where $\left(\frac{\partial f}{\partial t}\right)_{collision}$ is called 'collision term'.

If the applied electric field and the temperature are constant, the distribution of electrons is independent of time,

$$\frac{\partial f}{\partial t} = 0$$

so

$$v_k \cdot \nabla_r f(k, r) + \left(\frac{dk}{dt}\right) \cdot \nabla_k f(k, r) = \left(\frac{\partial f}{\partial t}\right)_{collision} \quad (4.5.2)$$

Eq.4.5.2 is known as stationary BTE.

If the wire is uniform, the distribution function is independent of real space,

$$\nabla_r f(k, r) = 0$$

and incorporated with formula

$$\frac{dk}{dt} = -\frac{qE}{\hbar}$$

then

$$-\frac{q}{\hbar} \mathbf{E} \cdot \nabla_k f(k) = \left(\frac{\partial f}{\partial t} \right)_{\text{collision}} \quad (4.5.3)$$

If applied field is low, the collision term can be written as (RTA)

$$\left(\frac{\partial f}{\partial t} \right)_{\text{collision}} = -\frac{f - f_0}{\tau(k)} \quad (4.5.4)$$

Here τ is called lifetime and it is the inverse of transition rate. Substitute Eq.4.5.4 into Eq. 4.5.3, the BTE reads,

$$-\frac{q}{\hbar} \mathbf{E} \cdot \nabla_k f(k) = -\frac{f - f_0}{\tau} \quad (4.5.5)$$

Obviously, the solutions $f(k)$ of Eq.4.5.5 depend on the applied electric field E .

It's able to expand $f(k)$ into series of E ,

$$f = f_0(E^0) + f_1(E^1) + f_2(E^2) + \dots \quad (4.5.6)$$

Substitute Eq.4.5.6 into Eq.4.5.5, then

$$-\frac{q}{\hbar} \mathbf{E} \cdot \nabla_k f_0 - \frac{q}{\hbar} \mathbf{E} \cdot \nabla_k f_1 + \dots = -\frac{f_1}{\tau} - \frac{f_2}{\tau} + \dots \quad (4.5.7)$$

The terms of the same exponent of E should be equal, so

$$\frac{f_1}{\tau} = \frac{q}{\hbar} \mathbf{E} \cdot \nabla_k f_0$$

$$\frac{f_2}{\tau} = \frac{q}{\hbar} \mathbf{E} \cdot \nabla_k f_1$$

$$\frac{f_3}{\tau} = \frac{q}{\hbar} \mathbf{E} \cdot \nabla_k f_2$$

⋮

Where f_0 is the distribution function under equilibrium, i.e. Fermi-Dirac distribution function, f_0 only depends on the electronic energy $E(k)$. We consider the distribution function up to the first-order approximation,

$$f = f_0 + f_1, \quad f_1 = \frac{q\tau}{\hbar} \mathbf{E} \cdot \nabla_k E(k) \left(\frac{\partial f_0}{\partial E} \right) \quad (4.5.8)$$

On the other hand, carriers in the wire will approach a new stationary distribution $f(k)$ very quickly under a constant and uniform field \mathbf{E} . For unit volume the number of electrons in dk is $f(k)dk/(2\pi)^3$. Assume the speed of electrons is $v(k)$, then the current density should be

$$-q \int f(k)v(k)dk/(2\pi)^3$$

The total current density is the integral over k -space,

$$j = -q \int f(k)v(k)dk/(2\pi)^3 \quad (4.5.9)$$

Substitute Eq.4.5.8 into Eq.4.5.9, then

$$j = -q \int f_0 v(k)dk/(2\pi)^3 - q \int f_1 v(k)dk/(2\pi)^3$$

Here the first term is equal to zero because it describes the current density under equilibrium, so

$$j = -q \int f_1 v(k)dk/(2\pi)^3 = -q^2 \int \frac{\tau}{\hbar} \mathbf{E} \cdot \nabla_k E(k) \left(\frac{\partial f_0}{\partial E} \right) v(k)dk/(2\pi)^3$$

For the situation of multi-band electronic structure, the formula of current density should be

$$j_i = -q^2 \int \frac{\tau_i}{\hbar} \mathbf{E} \cdot \nabla_k E_i(k) \left(\frac{\partial f_0}{\partial E} \right) v_i(k)dk/(2\pi)^3 \quad (4.5.10)$$

Here i denotes the index of band.

From now on, we will limit the discussion to one-dimensional (1D) nanowire. In 1D system j_i , \mathbf{E} , $\nabla_k E_i(k)$, dk and $v_i(k)$ in Eq.4.5.10 are scalar, and $(2\pi)^3$ should be changed into 2π also.

The definition of mobility is

$$j = \sum_i j_i = q \sum_i n_i \mu_i E = q n_T \mu E \quad (4.5.11)$$

Here n_T is the number of carriers and T is the temperature.

We combine Eq.4.5.10 with Eq.4.5.11, then we obtain

$$\mu_i = \frac{j_i}{q n_i E} = -\frac{q}{\hbar^2 n_i} \int \tau_i \left(\frac{\partial E_i(k)}{\partial k} \right)^2 \frac{\partial f_0(E)}{\partial E} \Omega dk / 2\pi$$

and

$$\mu = \frac{\sum_i n_i \mu_i}{n_T}, \quad n_T = \sum_i \int \rho_i(k) f_0(E_i(k)) \Omega dk / 2\pi$$

Where $\rho_i(k)$ is the density of state of band i , Ω is unit volume which is a constant. The number of occupation is one, $n_i = 1$, because we have considered the spin orbit coupling and per state is occupied by one electron. For the sake of convenience in programming, we change the integral with respect to k into a summation of electronic states:

$$\mu_i = -\frac{q}{\hbar^2} \sum_{k \in 1BZ} \tau_i(k) \left(\frac{\partial E_i(k)}{\partial k} \right)^2 \frac{\partial f_0(E)}{\partial E} \Big|_{E_i(k)},$$

$$\frac{1}{\tau_i(k)} = \sum_{q,j,b'} W_{q,j}(|k,i\rangle \rightarrow |k+q,b'\rangle) \quad (4.5.12)$$

and

$$\mu = \frac{\sum_i \mu_i}{n_T},$$

$$n_T = \sum_{i,k \in 1BZ} f_0(E) \Big|_{E_i(k)} \quad (4.5.13)$$

Where '1BZ' denotes the first Brillouin zone.

The formula for doping density of carrier is

$$D_{doping} = n_T / N_k V_{cell} \quad (4.5.14)$$

Where N_k is number of k points in the first Brillouin zone, $V_{cell} = N_{atom} \cdot \frac{a^3}{8}$ is

volume of unit cell, and N_{atom} is number of silicon atoms in unit cell.

Eq.4.5.12, Eq.4.5.13 and Eq.4.5.14 are employed by the code to calculate the low field mobility and the doping density of carrier.

4.5.2 Mean free path

Besides the low field mobility, another important transport property is the mean free path⁷² $L_i(k)$. The mean free path describes how far the carrier can transport between two scatterings. The formula of mean free path is

$$L_i(k) = v_i(k)\tau_i(k) \quad (4.5.15)$$

§4.6 CG algorithm of diagonalisation of large sparse matrix

Conjugate-gradient (CG) iterative algorithm⁷³ is a kind of method used widely in linear system. It was proposed by Hestenes and Stiefel in the beginning of 1950s at first⁷⁴. In the recent thirty years, CG method was developed rapidly⁷⁵⁻⁸⁰ and became one of the most popular methods applied to solve large sparse matrix. At the beginning CG method was used to solve positive definite symmetric matrix only, but afterwards preconditioned CG algorithm was developed and was applied to Hermitian matrix. In principle, CG method is a direct method and beyond order-N scaling. For large sparse matrix, it just needs a few steps to converge to a high accuracy with preconditioned CG algorithm.

4.6.1 Storage of sparse matrix⁸¹

Sparse matrix is defined as a matrix which has only a few nonzero elements. For example, the tight-binding Hamiltonian we used is a big sparse matrix because only the onsite terms and the elements between nearest neighbors are nonzero. The number of nonzero elements is proportional to the dimension of matrix. For large system, the total number of elements is very huge while the number of nonzero elements is limited. In many cases, the matrix is too big to deal with by standard algorithms, so

we need to modify standard algorithms to utilize the sparsity of sparse matrix in order to store and operate quickly.

There are a lot of methods to store a sparse matrix, and here we introduce the most common method which is adopted in the code also. For example, A is a sparse matrix as follows

$$A = \begin{bmatrix} 1 & 2 & 0 & 0 \\ 0 & 3 & 9 & 0 \\ 0 & 1 & 4 & 0 \end{bmatrix}$$

We can store matrix A by three arrays in computer,

$$\begin{aligned} a &= [1 \ 2 \ 3 \ 9 \ 1 \ 4] \\ ia &= [1 \ 3 \ 5 \ 7] \\ ja &= [1 \ 2 \ 2 \ 3 \ 2 \ 3] \end{aligned}$$

Where a contains all nonzero elements of A and the elements are ranked in the order of row, ia (ja) contains the row(column) numbers of nonzero elements in the same order as a . The meaning of ia is: the first and the second elements of a belong to the first row, the third and the fourth element of a belong to the second row, the fifth and the sixth element of a belong to the third row.

4.6.2 CG algorithm

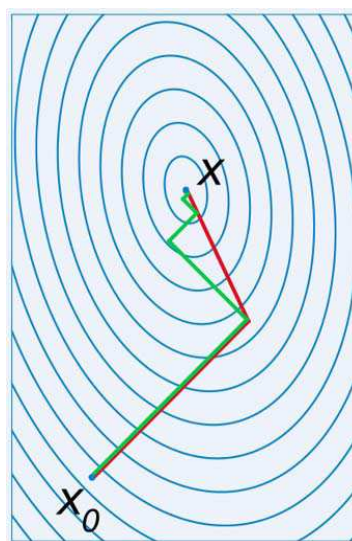


Fig.4.6.1 A comparison of the convergence of gradient descent with optimal step size (green) and conjugate gradient (red).⁸²

Conjugate gradient (CG) method⁸¹ is a technique searching the minimum of a function. It comes from the famous gradient descent (GD) algorithm⁸¹. The principle of CG is the same as GD, i.e. searching smaller values along the direction of gradient descent. The difference between CG and GD is the directions of gradient descent adopted by the two methods are slightly different. Fig.4.6.1 shows a comparison of the convergence of GD with optimal step size (green) and CG (red). We see CG is more efficient than GD. In principle, CG is a direct method and the convergence is guaranteed, but GD is an iterative method and converges asymptotically.

Definition: $A \in R^{n \times n}$ is a positive definite symmetric matrix, if $u^T Av = 0$ and $u^T Au > 0$, $v^T Av > 0$, then vectors u and v are conjugate with respect to A .

Theorem one: if $A \in R^{n \times n}$ is a positive definite symmetric matrix, then

1) solving equation $Ax = b$ is equivalent to searching the minimum of function $\varphi(x) = x^T Ax - 2b^T x$,

2) if there are n -dimensional vectors $u_1, u_2, \dots, u_m (m < n)$, and they are conjugate to each other, i.e.

$$u_i^T Au_j \begin{cases} = 0, i \neq j \\ > 0, i = j \end{cases} \quad i, j = 0, 1, \dots, m$$

then u_1, u_2, \dots, u_m are linearly independent,

3) if g_1, g_2, \dots, g_m are linearly independent vectors, then one can construct a series of vectors p_1, p_2, \dots, p_m from linear combinations of g_1, g_2, \dots, g_m , and p_1, p_2, \dots, p_m are conjugate to each other,

4) starting from any position vector $x_0 \in R^n$, searching the minimum of $\varphi(x) = x^T Ax - 2b^T x$ along directions of p_1, p_2, \dots, p_m , if p_1, p_2, \dots, p_m are conjugate to each other with respect to A , then the searching series $\{x_k\}_{k=0}^{m+1}$ satisfy

$$x_k = x_0 + \sum_{i=0}^{k-1} \alpha_i p_i, \quad \alpha_i = \frac{r_i^T p_i}{p_i^T A p_i},$$

5) if p_1, p_2, \dots, p_m are conjugate to each other with respect to A , starting from any position vector $x_0 \in R^n$, walking along directions of p_1, p_2, \dots, p_m , and searching series $\{x_k\}_{k=0}^{m+1}$ satisfy $x_{k+1} = x_k + \alpha_k p_k$, $\alpha_k = \frac{r_k^T p_k}{p_k^T A p_k}$ ($k = 0, 1, \dots, m-1$), and $x_m = x^*$, then x^* is the solution of equation $Ax = b$.

Algorithm: starting from any vector $x_0 \in R^n$ (e.g. $x_0 = 0$),

$$k = 0$$

$$r_0 = b - Ax_0$$

$$p_0 = r_0$$

loop: $k = 1, n$

$$\alpha_k = \frac{r_k^T r_k}{p_k^T A p_k}$$

$$x_{k+1} = x_k + \alpha_k p_k$$

$$r_{k+1} = r_k - \alpha_k A p_k$$

if $r_{k+1} < \varepsilon$ (e.g. $\varepsilon = 10^{-10}$) return

$$\beta_k = \frac{r_{k+1}^T r_{k+1}}{r_k^T r_k}$$

$$p_{k+1} = r_{k+1} + \beta_k p_k$$

$$k = k + 1$$

end loop

$$x^* = x_{k+1}$$

4.6.3 Convergence analysis

Here we introduce two theorems⁷⁵ as a reference for the analysis of convergence and errors.

Theorem two: $A \in R^{n \times n}$ is a positive definite symmetric matrix, if $A = I + B$ and $rank(B) = r$, then the accurate solution should be obtained within $r + 1$ iterations by CG method.

This theorem tells us the iteration of CG should converge to the accurate solution within $r + 1$ steps, so CG method is a direct method in principle. In application the scaling behavior of CG method is approximately in order of $\log(N)$, and the worst case is order N .

Theorem three: if x^* is the exact solution of equation $Ax = b$, then the error between x^* and the approximate solution x_k from CG iterative algorithm satisfies the following inequality:

$$\|x_k - x^*\|_A \leq 2 \left(\frac{\sqrt{\kappa_2} - 1}{\sqrt{\kappa_2} + 1} \right)^k \|x_0 - x^*\|_A \quad (4.6.1)$$

Where $\kappa_2 = \|A\|_2 \|A^{-1}\|_2$, and $\|A\|_2$ is the Euclidean norm of matrix.

From theorem three, we know that the smaller Euclidean norm κ_2 is, the smaller the error is and the quicker the convergence is.

4.6.4 Preconditioned CG⁸³

A preconditioner is a reversible matrix C that equation $C^{-1}Ax = C^{-1}b$ is easier to solve than equation $Ax = b$. The simplest preconditioner is a diagonal matrix that has just the diagonal elements of A . This is known as Jacobi preconditioning or diagonal scaling.

$$C_{ij} = \begin{cases} 0, & i \neq j \\ A_{ij}, & i = j \end{cases} \quad (4.6.2)$$

Since diagonal matrices are trivial to invert and store in memory, a Jacobi preconditioner is a good starting point. More sophisticated choices must trade-off the reduction in the condition number of A , such as symmetric Gauss-Seidel (SGS)

preconditioner and Symmetric Successive Over Relaxation (SSOR) preconditioner. The SSOR preconditioner is of the fastest convergence.

4.6.5 Eigenvalue⁸¹

For a square matrix A , a vector x and a scalar λ , if they satisfy

$$Ax = \lambda x \quad (4.6.3)$$

then x is called the eigenvector of A and λ is called the eigenvalue of A . The condition of nontrivial solution is

$$p(\lambda) \equiv \det(A - \lambda \cdot I) = 0 \quad (4.6.4)$$

$p(\lambda)$ is called the characteristic polynomial. From $p(\lambda) = 0$ we can derive the eigenvalues directly.

In application, it's always difficult to solve the eigenvalues and eigenvectors of A directly. Because computing the polynomial is very expensive in itself, and analytic roots of a high-degree polynomial are difficult to express. Effective numerical algorithms for approximating roots of polynomials exist, but very small errors of eigenvalues can lead to very large errors of eigenvectors. Therefore, we generally use iterative algorithms like CG to find eigenvalues and eigenvectors. Solving the eigenvalues is equivalent to searching the minimum of function $\zeta(x) = x^T Ax / x^T x$. So we can use a similar CG algorithm, as described in section 4.6.2, to calculate the eigenvalues efficiently. If we got the eigenvalues of matrix A , we can derive the eigenvectors by solving linear equations

$$(A - \lambda \cdot I)x = 0 \quad (4.6.5)$$

with CG method.

§4.7 Outlook of the code

First, for the present the code can be used to calculate the low-field transport properties only, because relaxation time approximation (RTA) is used. But the

scattering matrix element and transition rate obtained by the code are the basic parameters of Boltzmann transport equations (BTE). So we plan to develop the code to solve BTE directly with Monte-Carlo simulation and then the code will be able to simulate the transport properties of SiNWs in the presence of high field.

Second, at the beginning the electronic model and phononic model employed by the code were designed to be able to describe the strain effect of lattice. Therefore, we plan to add the high-order terms of the VFF potential energy to the code to study the strain effect in transport properties of SiNWs.

Third, we will extend the code to some other materials if there are appropriate tight-binding parameters.

Fourth, in principle the method of the code is able to be implemented into an ab-initio code, therefore it's possible to study transport properties of nano-electronic devices in the diffusive regime from first principle.

Speaking in general, our knowledge of the electric transport of materials in the diffusive regime becomes deeper and deeper as the performance of computer improves.

Chapter 5 E-p coupling effect in transport properties of SiNW

SiNWs are investigated widely because there are a lot of applications of SiNW in making electronic devices. Transport property is the most important factor to decide the performance of an electronic device. Therefore, we need to know the mechanism of each kind of scattering that reduces the mobility of carriers. From experiments and theoretical studies, it's proven that at room temperature the scattering from lattice vibration is the most important mechanism in silicon and is the major factor that reduces the mobility of carriers. However, studies on the mechanism of electron-phonon (e-p) scattering in SiNWs are rare. There are several reasons: in experiments, at present high purity crystalline SiNWs are difficult to fabricate and the contact between lead and single SiNW is uncontrollable; in theoretical studies, there are too many atoms in one unit cell even for the smallest SiNW, so it's too expensive to obtain the electronic structure from first principle. That is to say, it is a big challenge to study e-p coupling effect in transport properties of SiNW at the atomic level before this work. In this thesis, we have proposed a new method that makes it possible to study the transport properties and e-p coupling effect in SiNWs directly. The method is implemented into a code with which we studied electronic structures, phonon spectra, vibration modes of SiNWs in various orientations. And we also studied the low-field transport properties of [110]SiNWs. This chapter will introduce the results and we will also give out a detailed discussion on the e-p coupling effect in transport properties of SiNW.

§5.1 Electronic structure of SiNW

In recent years electronic structures of SiNW are studied a lot⁸⁴⁻⁹⁷. The number of silicon atoms in SiNW is proportional to the square of diameter: $N_{Si} \propto d^2$. Therefore, the number of atoms in SiNW increases rapidly with size. For example, a [112]SiNW of 10nm diameter includes over 3,000 silicon atoms and about 300 hydrogen atoms in one unit cell. It is the big size of unit cell that makes the investigation of electronic structure from first principle very difficult. So far, the biggest size of SiNWs studied from first principle is 4.2nm of diameter⁹¹. More frequently, people use tight-binding (TB) model or $k \cdot p$ model to study the electronic structure of SiNW. With these methods people can study SiNWs of over 10nm diameter. TB model is much more accurate than $k \cdot p$ model, so we employ TB method in the code. The transferability of TB model depends on the TB parameters, so we should be careful when we apply a set of bulk parameters to SiNWs. Due to the quantum-confinement effect, old parameters can not describe the band structure of SiNW exactly. Jancu *et al.* proposed a TB model⁴⁸ and took into account the deformation potential. Applied to SiNWs, Jancu's model is accurate for the valence band but not so good for the conduction band. Niquet improved Jancu's model by including the strain effect of onsite terms in Hamiltonian. The TB parameters were fitted with ab-initio band structure of bulk silicon with GW correction^{98,99}. By comparing with ab-initio results it has been confirmed that Niquet's model is able to reproduce the deformation potentials of conduction band and valence band for both bulk silicon and SiNW. Therefore, we employed Niquet's model⁶¹ in the study. For further particulars about Niquet's model, please refer to Appendix A.

In this section we introduce the electronic structures of [001]SiNW, [110]SiNW, [111]SiNW, and [112]SiNW with various diameters as shown in Fig.5.1.1, Fig.5.1.2, Fig.5.1.3, and Fig.5.1.4, respectively. In the figures, a (=5.431Å) is the lattice constant of bulk silicon, d denotes the diameter of SiNW. For the sake of contrast, electronic bands of different diameter SiNWs are arranged into a line.

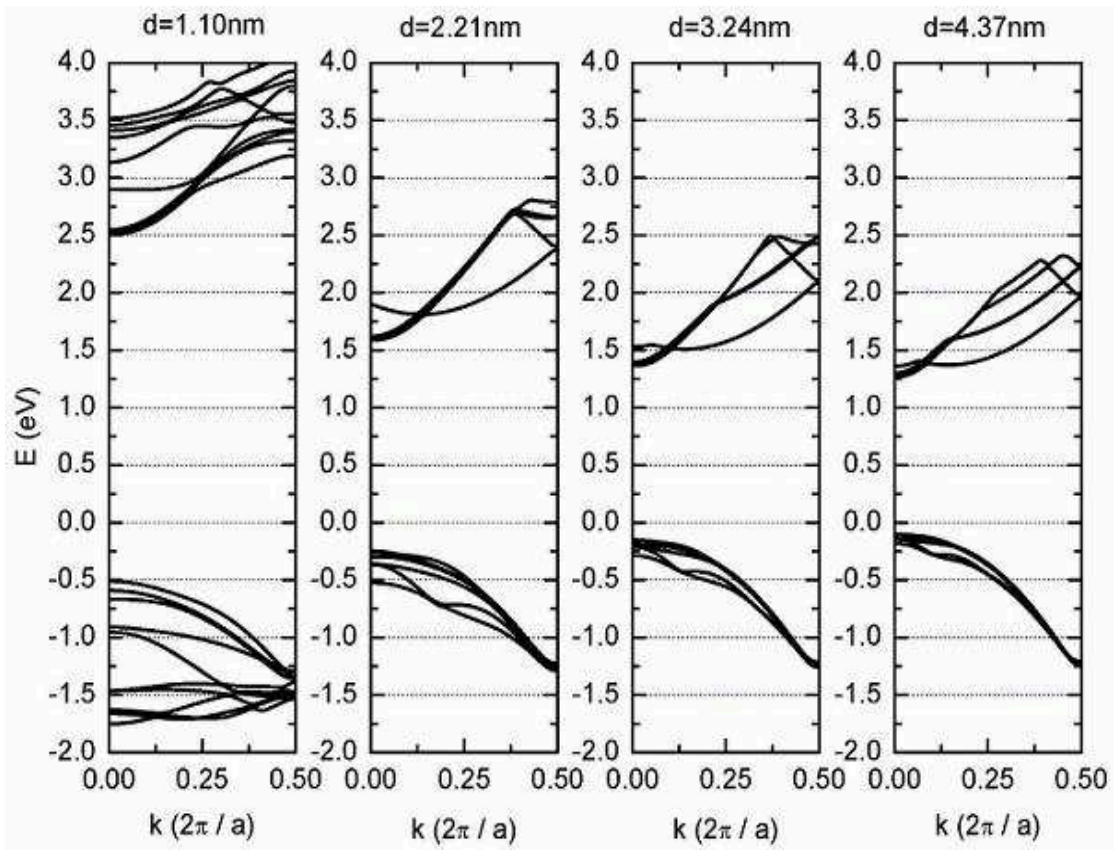


Fig.5.1.1 Electronic structure of [001]SiNW with different diameters

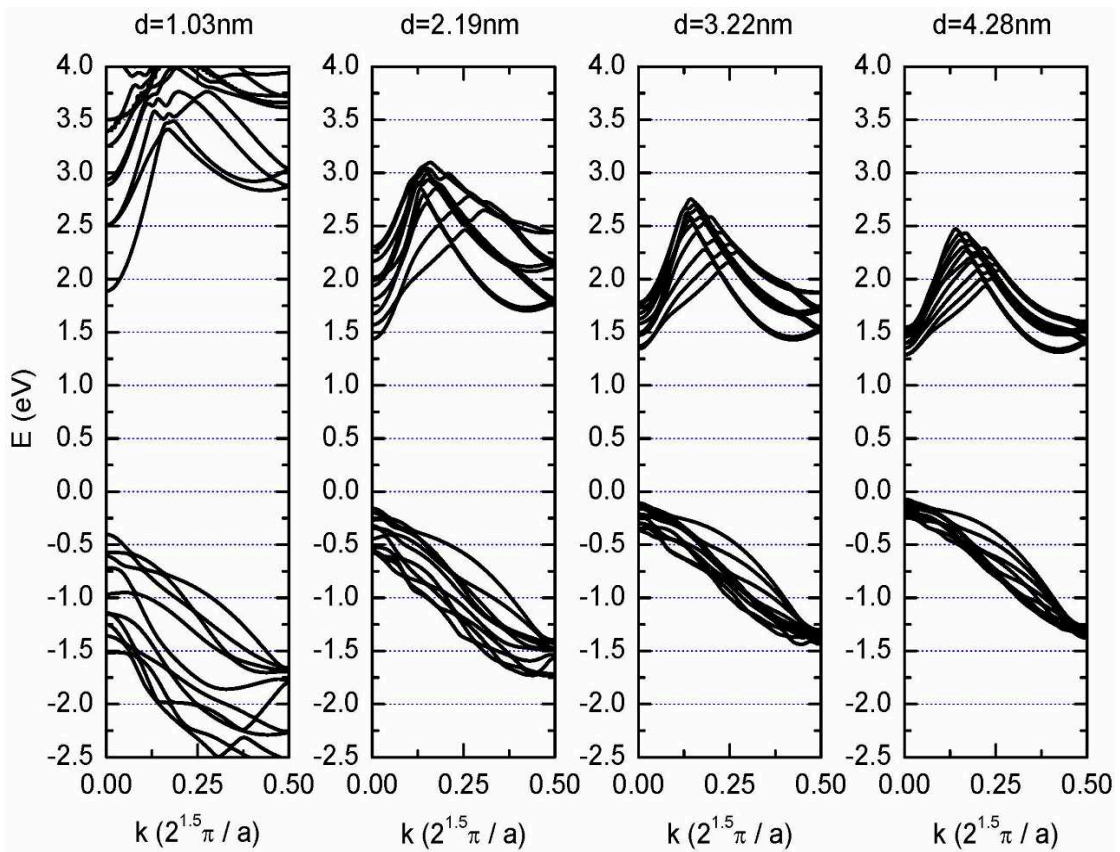


Fig.5.1.2 Electronic structure of [110]SiNW with different diameters

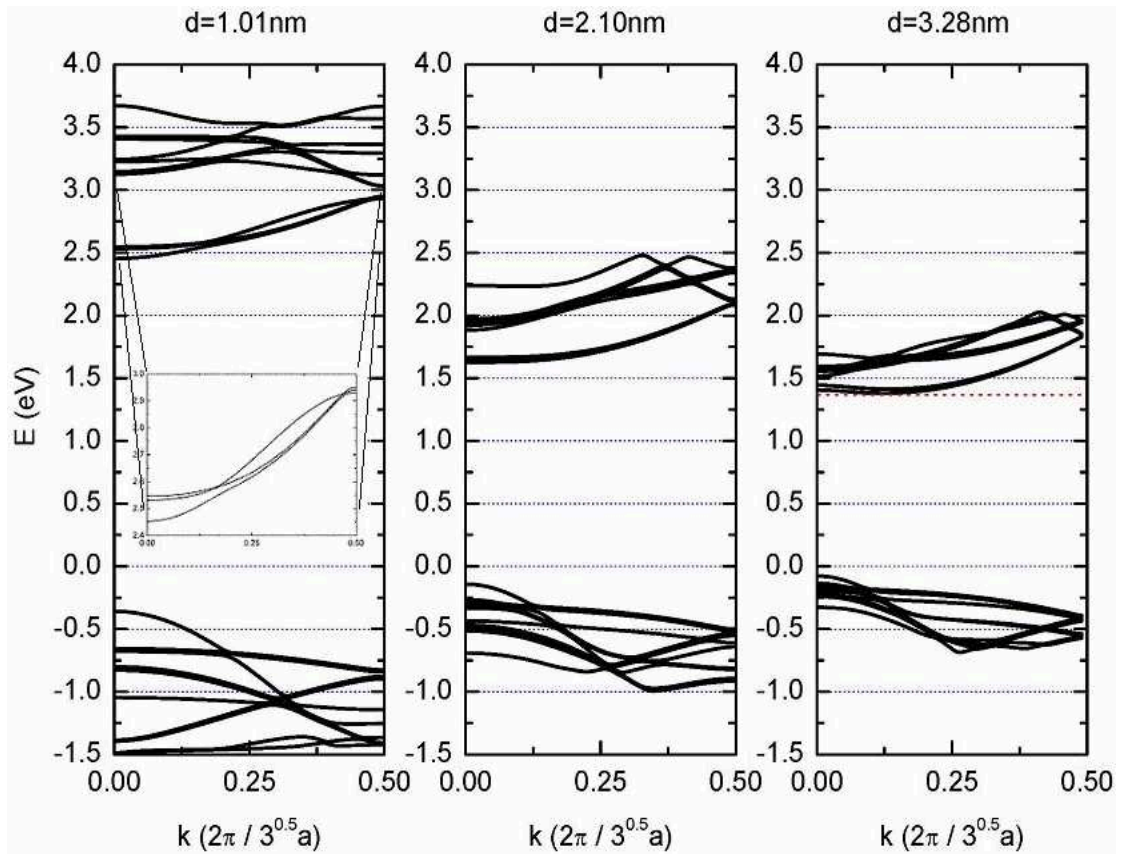


Fig.5.1.3 Electronic structure of [111]SiNW with different diameters

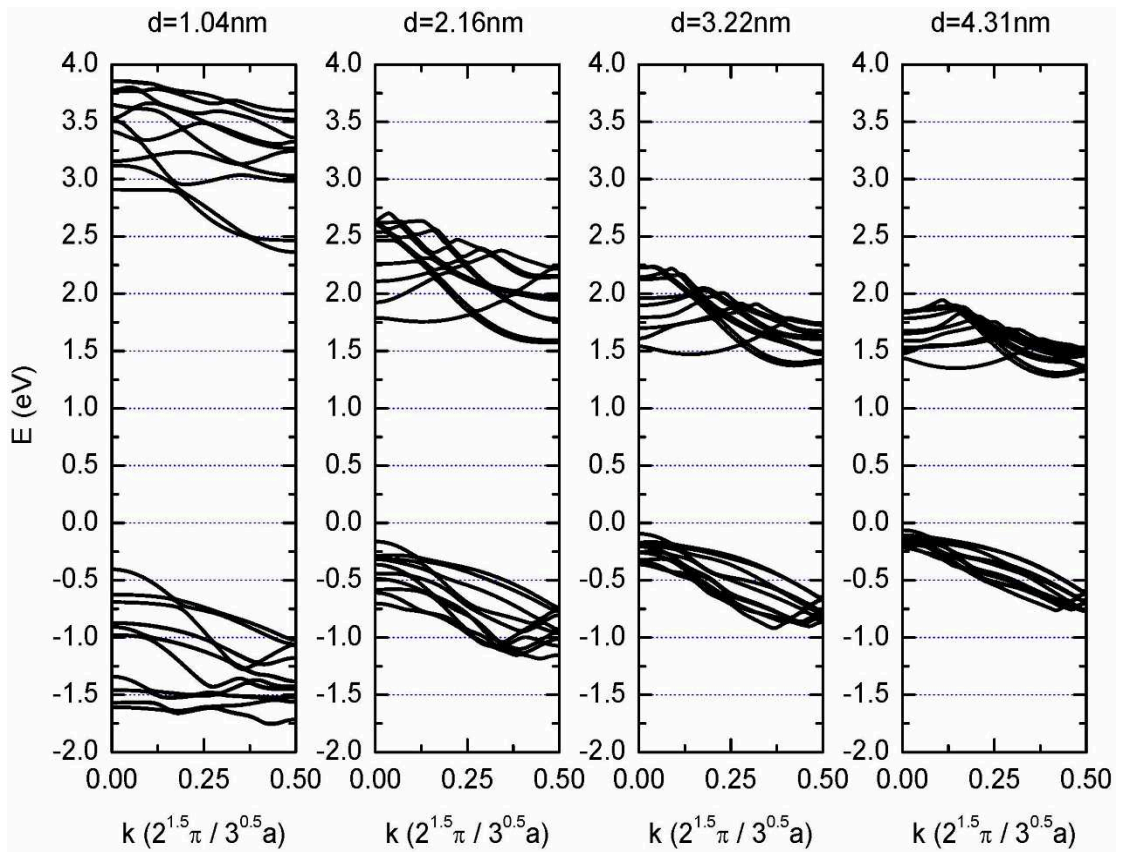


Fig.5.1.4 Electronic structure of [112]SiNW with different diameters

Table 5.1 Values of $K_{c(v)}$, $a_{c(v)}$, and $b_{c(v)}$ ⁴⁵

	K (eV nm ²)	a (nm)	b (nm)
[001] _c	0.6589	0.235	0.142
[001] _v	-0.8825	1.245	0.488
[110] _c	0.6470	0.123	0.849
[110] _v	-0.6825	2.062	0.996
[111] _c	0.8010	0.342	0.212
[111] _v	-0.6964	3.664	-0.374
[112] _c	0.7273	0.246	0.313
[112] _v	-0.7075	2.616	-0.083

From the figures, we see the gap of SiNW decreases and tends to the bulk value (~1.2eV) as the diameter increases. Niquet⁴⁵ *et al.* proposed an empirical formula for the energy gap of SiNW as follows:

$$E_g(R) = E_g(\infty) + \frac{K_c}{R^2 + a_c R + b_c} - \frac{K_v}{R^2 + a_v R + b_v} \quad (5.1.1)$$

Here $E_g(\infty)$ denotes the energy gap of bulk silicon, $K_{c(v)}$, $a_{c(v)}$, and $b_{c(v)}$ are empirical parameters. The values of parameters are shown in table 5.1.

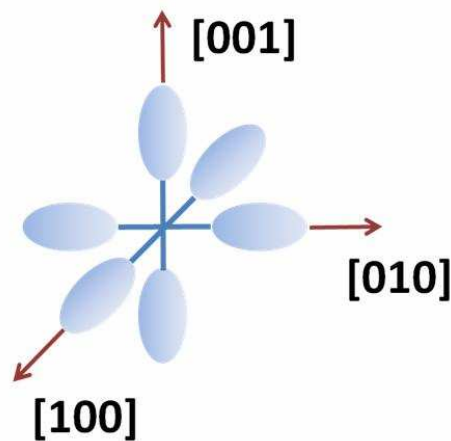


Fig.5.1.5 Constant-energy ellipsoids in the Brillouin zone of silicon¹⁰⁰ near the six conduction band minima. The longitudinal and transverse effective masses are:

$$m_l = 0.92m, \quad m_t = 0.19m, \quad \text{and } m \text{ is the free electron mass.}$$

Electronic band structures of SiNWs along different orientations are different:

- 1) The conduction band minimum of direct gap (CBM1) of [001]SiNW lies on $k = 0$, and the conduction band minimum of indirect gap (CBM2) of [001]SiNW lies on $k \approx \pm 0.4\pi/a$. In fact, there are six equivalent conduction band minima (CBM) located around $\pm 0.8\Gamma X$ in the Brillouin zone of bulk silicon, i.e. around $\pm 1.6\pi/a$ along directions of $\langle 001 \rangle$, $\langle 010 \rangle$ and $\langle 100 \rangle$. The constant-energy surfaces in the vicinity of CBMs are ellipsoids elongated along the ΓX axes as shown in Fig.5.1.5. Electrons have a heavy effective mass along ΓX and a light effective mass perpendicular to ΓX . Four CBMs along $\langle 010 \rangle$ and $\langle 100 \rangle$ project onto $k = 0$ and the last two CBMs along $\langle 001 \rangle$ project onto $k \approx \pm 0.4\pi/a$ in [001]SiNW. CBM1 is lower than CBM2, because electrons around the $\langle 001 \rangle$ minima are light in the plane vertical to nanowire and thus of a higher energy, while electrons around the other four minima are heavier because of the character mixed heavy and light. At room temperature, high-energy phonons exist and electrons located in the first conduction band will be able to jump to CBM2 by absorbing a phonon or vice versa when the splitting Δ between CBM1 and CBM2 is small $\sim 200\text{meV}$. Thus the transport properties of SiNWs depend strongly on Δ and the temperature.
- 2) In [110]SiNW, CBM1 lies on $k = 0$ and CBM2 lies on $k \approx \pm 0.8\pi/l$ with $l = a/\sqrt{2}$ the length of unit cell. Two CBMs along $\langle 001 \rangle$ project onto $k = 0$. The other four CBMs project onto $k \approx \pm 0.8\pi/l$. Electrons around the $\langle 001 \rangle$ minima are heavier than electrons around $\langle 010 \rangle$ and $\langle 100 \rangle$ along the nanowire. Therefore, CBM1 is lower than CBM2. It's worth noting that the first several conduction bands are close to each other for [110]SiNWs, thus not only intraband scattering but interband scattering via phonons play an important role in the electronic transport of [110]SiNWs.
- 3) In [111]SiNW, there is only one band gap located at $k \approx \pm 0.4\pi/a$ because all six

minima of bulk silicon project onto this k point in [111]SiNW. Note that interband coupling splits the sixfold degenerate CBMs of bulk silicon into three subbands. The splitting between subbands is very small and depends strongly on the detailed structure of SiNW. For example in 1.01nm-diameter [111]SiNW the splitting between the first and the second conduction band is about 79meV, and about 14meV between the second and the third conduction band. There is another interesting phenomenon to note for [111]SiNW: the band gap changes from indirect gap to direct gap as diameter decreases because the quantum-confinement effect is more and more prominent when SiNW becomes thinner.

- 4) The electronic band structure of [112]SiNW is a bit more complicated than the other SiNWs mentioned above. [112]SiNW is an indirect-gap semiconductor. CBM1 and CBM2 are located at $k \approx \pm 0.4\pi/a$ and $k \approx \pm 0.8\pi/l$ separately. But the position of CBM1 approaches Γ point and the position of CBM2 approaches the boundary of Brillouin zone when the diameter of SiNW decreases. This phenomenon also comes from the quantum-confinement effect.

In general, the electronic structure of SiNW is strongly dependent on the diameter and orientation. With increasing the diameter, conduction bands of SiNWs become denser, and the quantum-confinement effect becomes smaller.

§5.2 Phonon structure of SiNW

Based on the theory of lattice dynamics and the Vanderbilt's VFF model introduced in chapter three, we studied the vibrational properties of SiNWs along [001], [110], [111] and [112] separately. The corresponding phonon structures are shown in Fig.5.2.1, Fig.5.2.2, Fig.5.2.3, and Fig.5.2.4.

In bulk materials, there are three acoustic modes that pass through the Γ point, and the other curves are optical modes that have positive values at the Γ point. In SiNWs, those optical modes of low frequency are from the bulk acoustic modes³⁸.

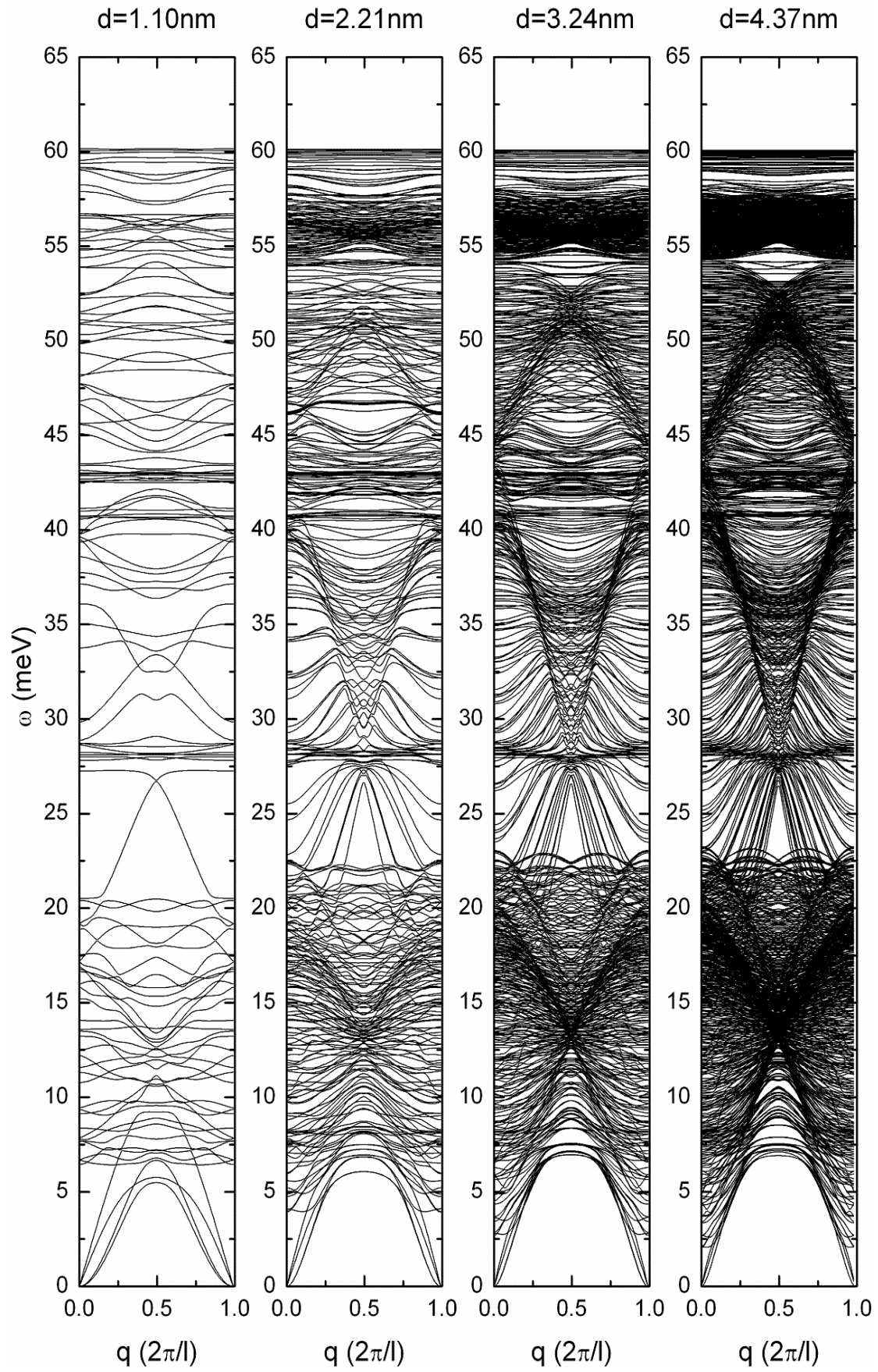


Fig.5.2.1 Phonon structure of [001]SiNW with different diameters

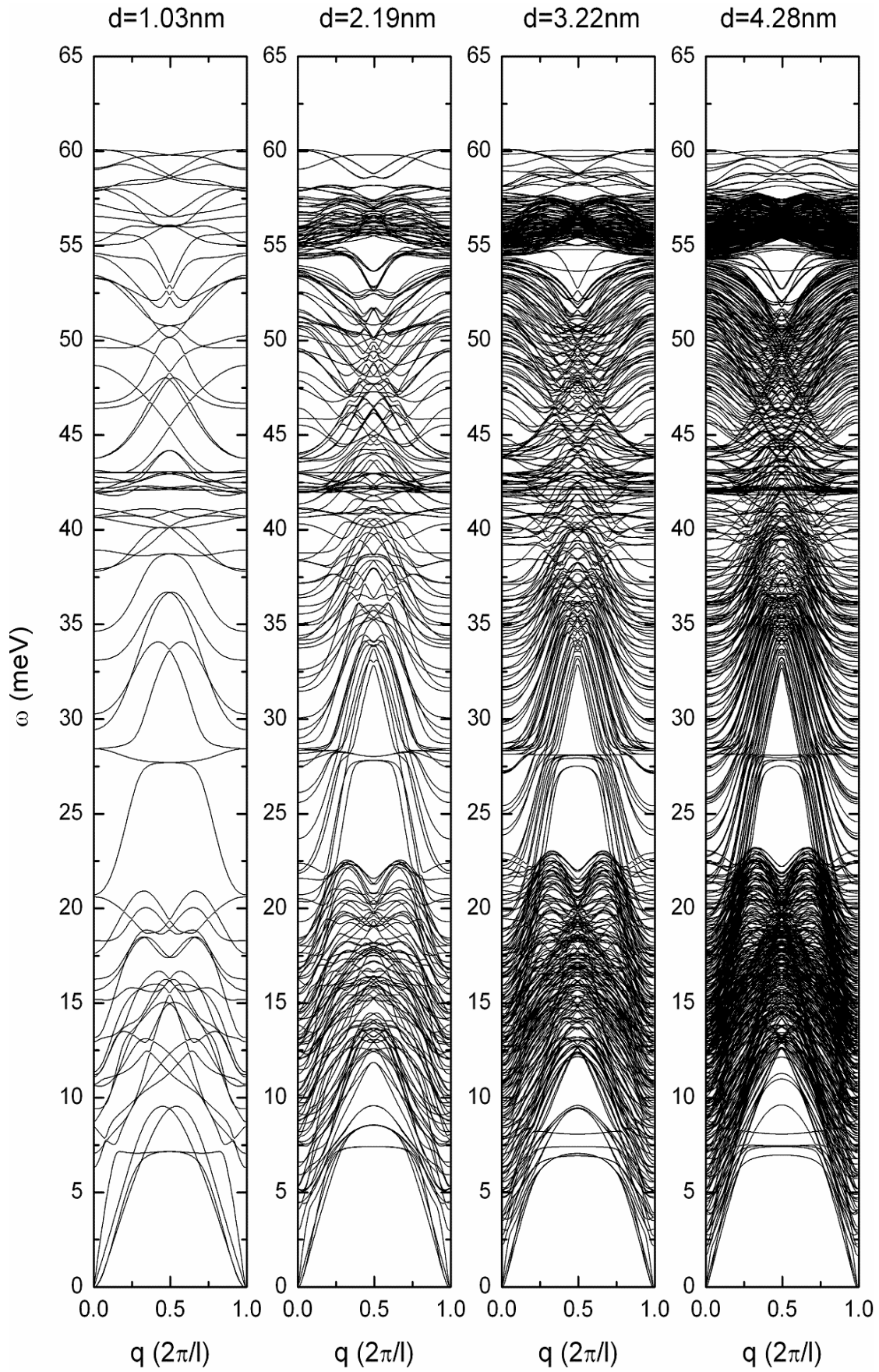


Fig.5.2.2 Phonon structure of [110]SiNW with different diameters

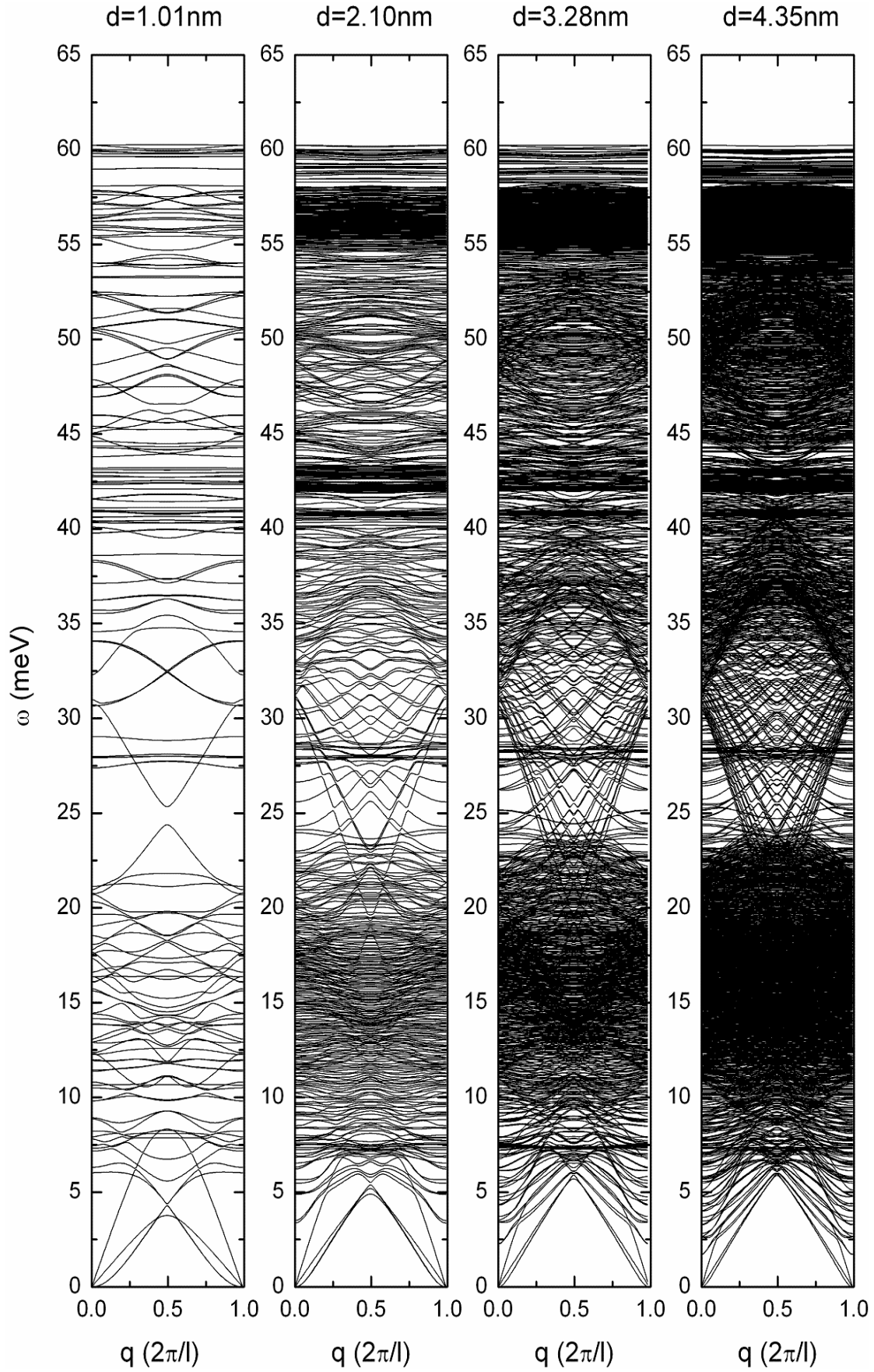


Fig.5.2.3 Phonon structure of [111]SiNW with different diameters

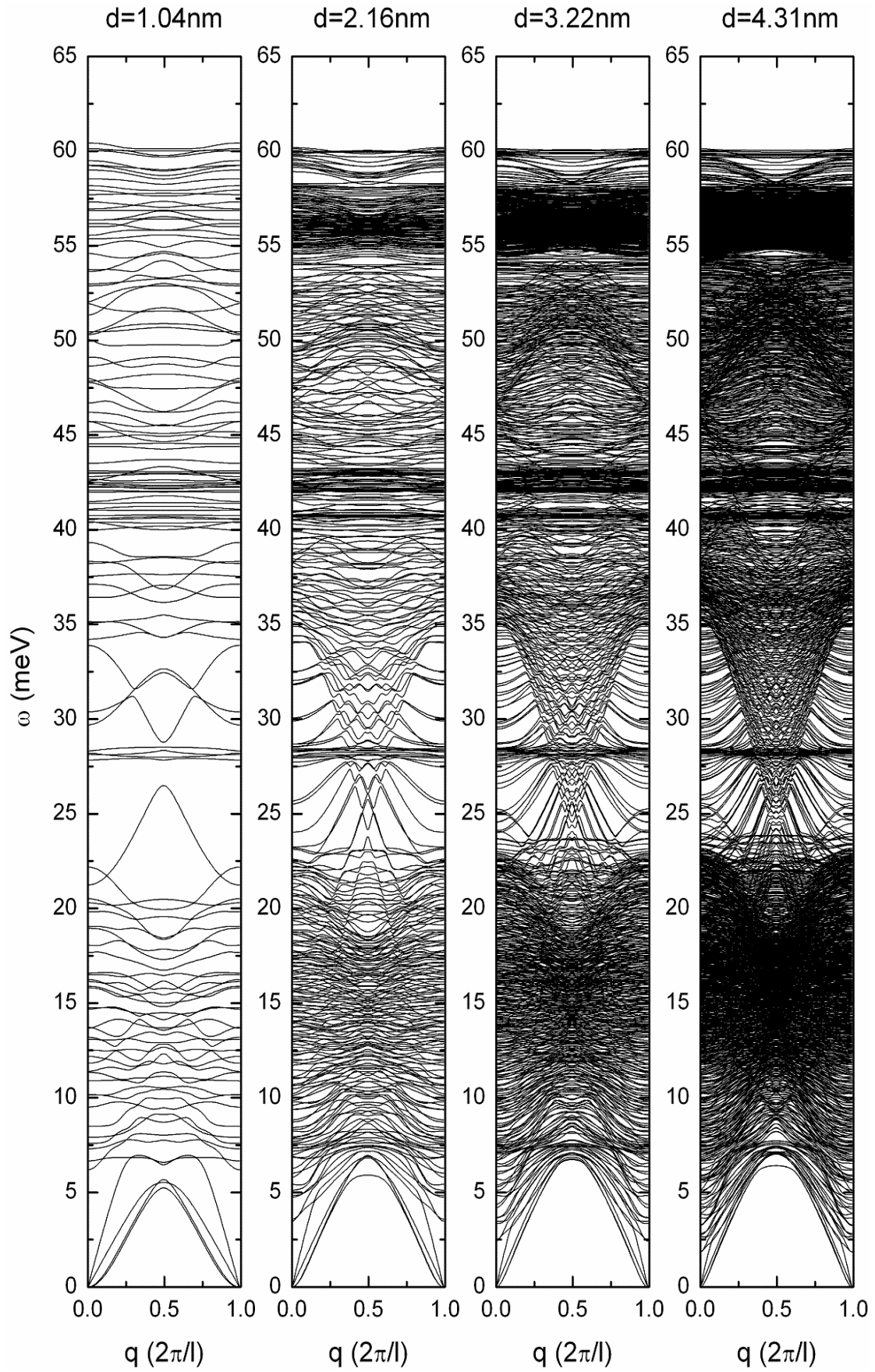


Fig.5.2.4 Phonon structure of [112]SiNW with different diameters

From the figures, we find there are four acoustic modes passing through the Γ point in SiNWs. Frequencies of the lowest two acoustic modes are proportional to the square of wavevector $\omega \propto q^2$, and frequencies of the other two acoustic modes are proportional to wavevector $\omega \propto q$. It is also a character³⁸ of 1D nanowire to have two branches proportional to q^2 . The two branches linear in q are identified as the longitudinal and transverse acoustical phonons. From the center to boundary of the first Brillouin zone, phonon modes get together gradually. Except for the stretching mode¹⁰¹ of Si-H bond ($\sim 200\text{meV}$), the largest energy of phonon is about 60meV corresponding to the bending mode of Si-H bond. There should be $3N$ phonon modes if there are N atoms in one unit cell. With increasing the diameter, there will be more and more modes, but the energy of phonon is limited, so the dispersion curves grow denser and denser.

We find the energy of the first nonzero mode at the Γ point declines and the energy of the lowest mode at the boundary of the first Brillouin zone increases as diameter increases. These two phenomena are called phonon softening and hardening respectively and they are due to the confinement effect of 1D system. The phonon softening and hardening in SiNWs are reported in Ref.¹⁰² and Ref.¹⁰³ also, and Peelaers¹⁰² *et al.* discussed the phenomena in detail.

In order to understand the vibration of lattice visually, Fig.5.2.5 shows the vibration modes i.e. the eigenvectors of four selected phonons of 2.19nm -diameter $[110]\text{SiNW}$. Fig.5.2.5a shows the vibration of the first acoustic phonon which is proportional to q^2 . Fig.5.2.5b shows the vibration of the third acoustic phonon i.e. the longitudinal acoustic phonon. Fig.5.2.5c shows the vibration of the fifth mode which is the lowest nonzero phonon at Γ point. Fig.5.2.5d shows the vibration of the radial breathing mode (RBM) of $[110]\text{SiNW}$.

The number of phonon mode increases as diameter increases, and consequently there are more electron-phonon scattering. At equilibrium or near equilibrium, phonons obey the Bose-Einstein distribution,

$$n_{Bose-Einstein}(\hbar\omega) = \frac{1}{e^{\hbar\omega/k_B T} - 1}$$

At room temperature (300K), $k_B T = 25.85$ meV, the distribution of phonon is shown in Fig.5.2.6. The number of phonon whose energy is equal to 25.85meV is 0.582. Therefore, there are only acoustic phonon scatterings at low temperature (77K) and there will be more and more optical phonon scatterings as temperature increases. The optical phonon scattering plays an important role in electronic transport under the room temperature.

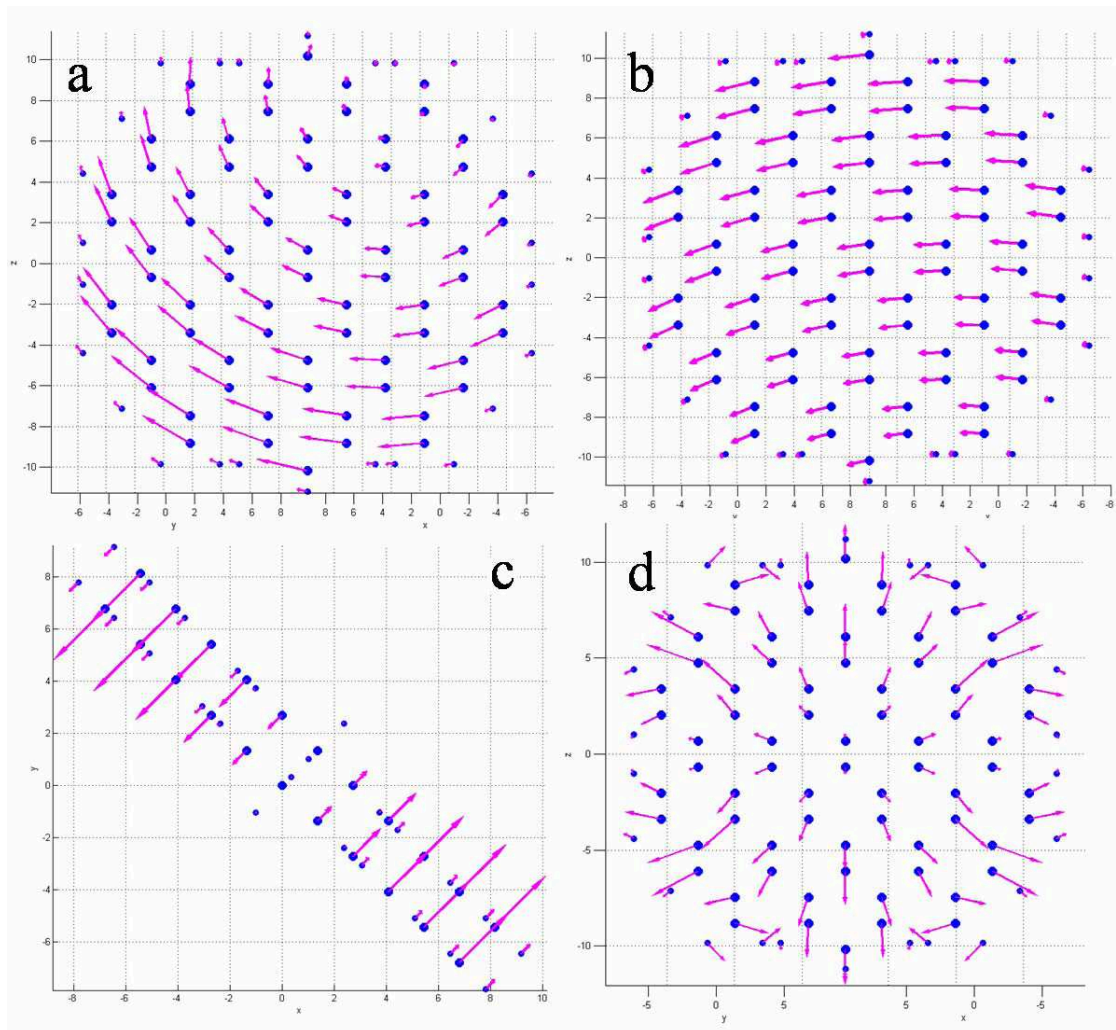


Fig.5.2.5 Vibration mode of 2.19nm [110]SiNW at $q = 0$ (Γ). a) 1st acoustic mode (cross-section view), b) 3rd acoustic mode (cross-section view), c) 5th mode (side view), d) radial breathing mode (cross-section view). Big circles denote silicon atoms, small circles denote hydrogen atoms, red arrows denote the directions and amplitudes.

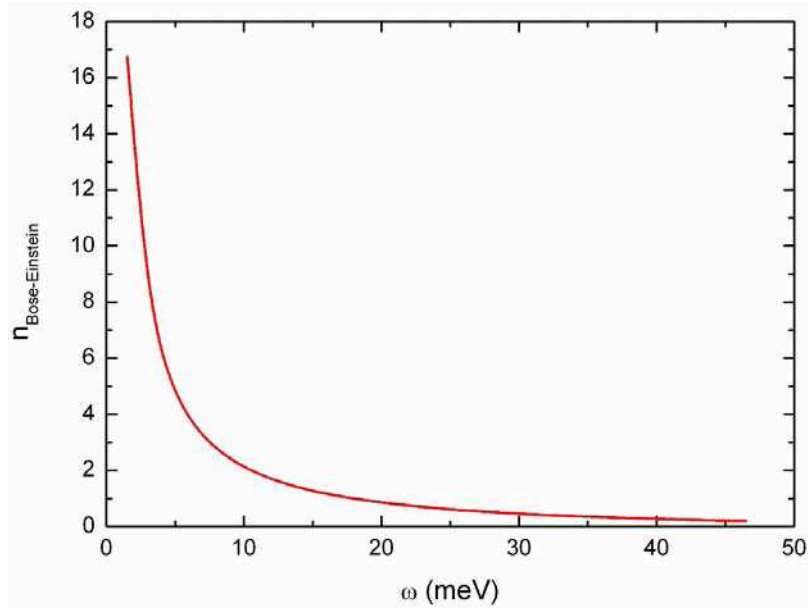


Fig.5.2.6 Bose-Einstein distribution of phonons at room temperature (300K).

§5.3 [110]SiNW: low-field mobility and e-p coupling effect

Traditionally it's believed that electronic mobility of SiNW would be larger than bulk silicon because the electronic density of state of SiNW is smaller than bulk silicon¹⁰⁴⁻¹⁰⁶. In fact, measurements of transport properties of SiNW-field-effect transistors (SiNW-FET) showed a contrary fact: the electronic mobility of SiNW is smaller than bulk silicon. For narrow channels of silicon, the mobility could be even ten times smaller. Therefore, we need to study the transport theory of SiNWs urgently. As is well known, in transport the electrons are affected by phonon scattering¹⁰⁷⁻¹²⁷, coulomb scattering¹²⁸⁻¹⁵⁴, surface-roughness scattering¹⁵⁵⁻¹⁷³, impurity scattering¹²⁸⁻¹³² and a lot of other factors. Among all these factors the electron-phonon (e-p) coupling plays a major role in electronic transport of high purity SiNW at room temperature.

So far, there have been some works¹⁷⁶⁻¹⁷⁹ that studied the e-p scattering rate of SiNWs and several works^{174,175,180,181} that calculated the mobility of carriers in SiNWs by solving the Boltzmann transport equation. These theoretical works confirmed the experiments and revealed the physics in electronic transport of SiNWs: the electronic mobility of SiNW is smaller than bulk silicon because the e-p coupling in SiNWs is

much larger than the e-p coupling in bulk silicon i.e. the overlap of electronic wavefunction and phonon eigenvector is much larger in SiNWs than in bulk silicon, although the electronic density of state of SiNW is smaller. This illustrates that the quantum-confinement effect becomes more and more prominent as the size of system decreases to nanometer scale. The electronic structures and phononic structures of SiNWs are completely different from bulk silicon as introduced in previous sections. Previous theoretical studies have predicted some transport properties of SiNWs, however, there are some disadvantages: 1) due to the expensive cost of full band calculation, most of previous works applied the $k \cdot p$ model or simpler single-effective-mass model to simulate the electronic structure of SiNW, these models can describe the band structure around the Γ point very well but they are invalid for general k points, 2) the models for phononic structure of SiNW are very simple in previous works, various empirical formula or elastic continuum wave equations even bulk phonons were used to simulate the phononic structure of SiNW, 3) most of previous works considered intraband electronic transitions only, only a few works included the interband scattering, but the discussion about interband scattering is very limited and qualitative due to the inaccuracy of electronic wavefunction and phonon eigenvector, 4) it is difficult to discuss the acoustic phonon scattering and the optical phonon scattering uniformly, because previous works treated the acoustic mode and the optical mode by different models. For the sake of solving these problems and within current power of computation, we incorporated the tight-binding model and the valence-force-field model introduced in pre-chapters with Boltzmann transport equation to study the transport properties of SiNWs at atomic level. We have studied the low-field transport properties of [110]SiNW with the new method. This section introduces the results and discussions.

5.3.1 Low-field mobility versus density of carrier

Fig.5.3.1 and Fig.5.3.2 show the dependence of low-field mobility on density of carrier in 2.19nm [110]SiNW at low temperature and at room temperature separately.

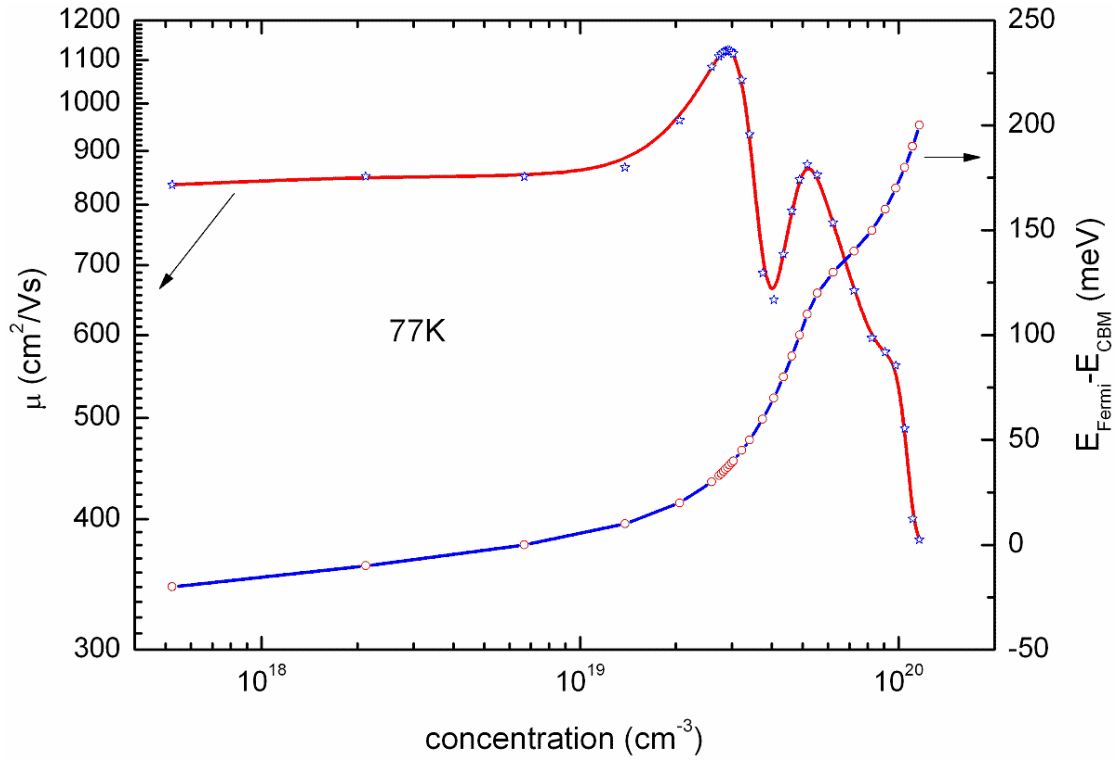


Fig.5.3.1 Low-field mobility versus doping concentration of electrons (red line), and Fermi level versus doping concentration of electrons (blue line) at 77K.

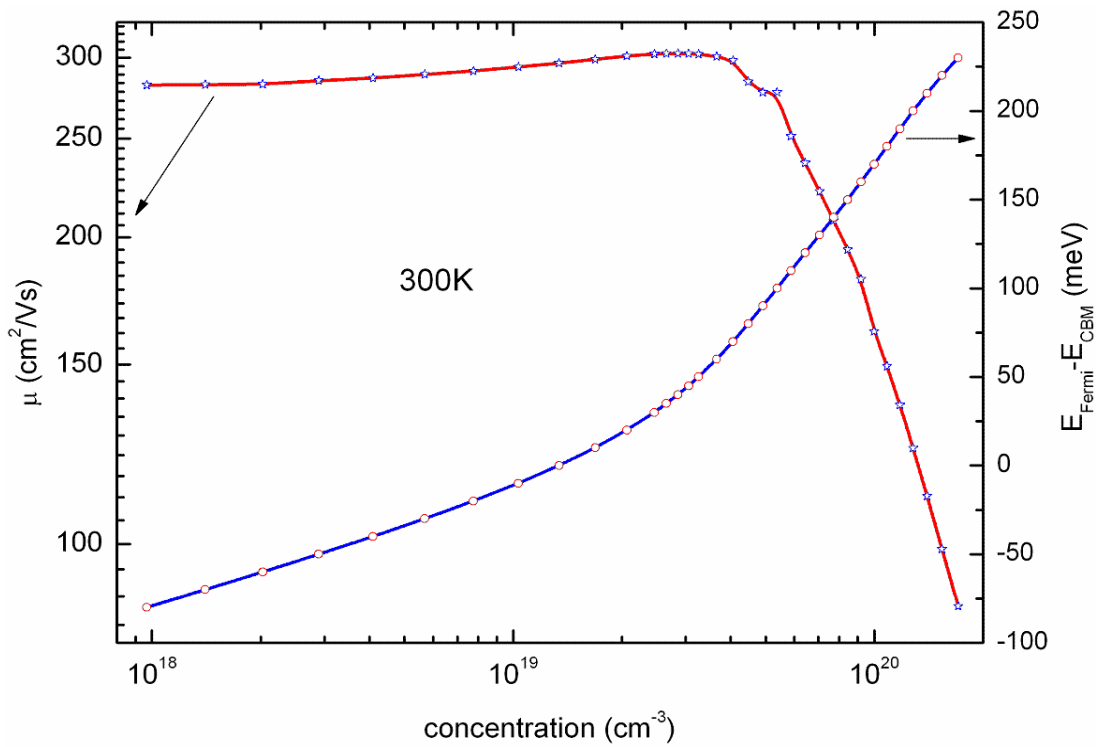


Fig.5.3.2 Low-field mobility versus doping concentration of electrons (red line), and Fermi level versus doping concentration of electrons (blue line) at 300K.

When the doping density of electron is low, both figures show the low-field mobility is almost constant. That is because the low-field mobility is nearly independent on the Fermi level at low doping density.

More and more electrons occupy the high-energy states in the lowest several conduction bands even the states around the conduction band minimum of indirect gap at $k \approx \pm 0.8\pi/l$ as the doping density of electron increases. Electrons are fermions and obey the Fermi-Dirac distribution as shown in Fig.5.3.3. The distribution of electrons decreases exponentially with the energy of electron. Only the distribution of electrons within 100meV above the Fermi level is visible. In calculations, we consider all electronic states within 500meV in the vicinity of the Fermi level to ensure all possible transitions being included. On the one hand, hot electrons can occupy states with dozens even hundreds of milli electron volts above the Fermi level. On the other hand, the energy differences of lowest conduction bands become smaller and smaller as increasing the diameter of SiNW. Therefore, interband transitions of electron play an important role in transport properties of SiNWs. This is different from the situation in bulk silicon. In bulk silicon, the interband scattering is not prominent and can be ignored.

In the formula of low-field mobility (Eq.4.5.12), there is a derivative of Fermi-Dirac distribution function with respect to energy of electron. We plot the derivative of Fermi-Dirac distribution function in Fig.5.3.4. From this figure, it's clear to see the broadening of Fermi-Dirac function at room temperature is about 400meV in the vicinity of Fermi level and the states outside of this range make no contribution to the low-field mobility.

At 77K, there are only the acoustic phonons of low energy and the broadening of Fermi-Dirac function is very small $\sim 13.2\text{meV}$, so there are two peaks of mobility in Fig.5.3.1 corresponding to the lowest two conduction bands respectively.

At 300K, there are much more phonons than at 77K and most of them are optical phonons. Thus the mobility is much smaller. Due to a big broadening of Fermi-Dirac function ($\sim 51.7\text{meV}$), there is only one very wide peak of mobility in Fig.5.3.2.

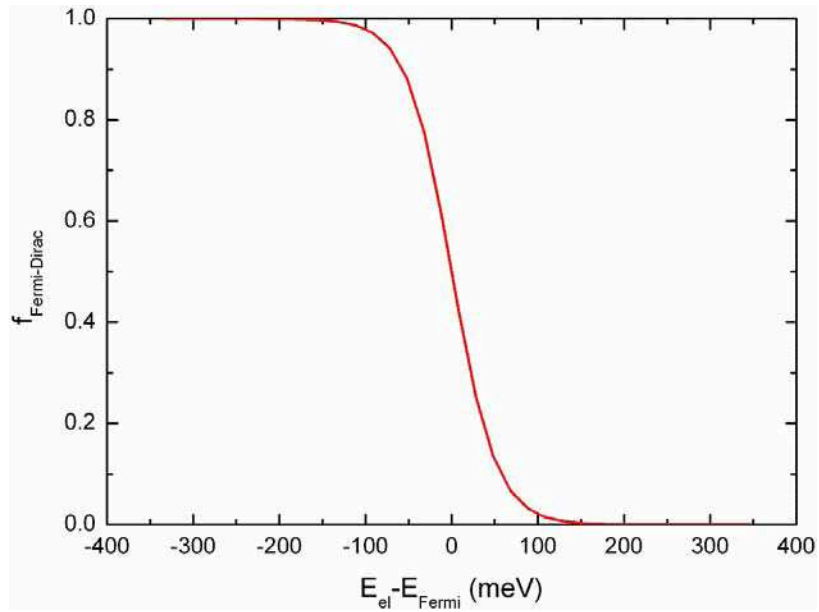


Fig.5.3.3 Fermi-Dirac distribution of electrons at room temperature (300K).

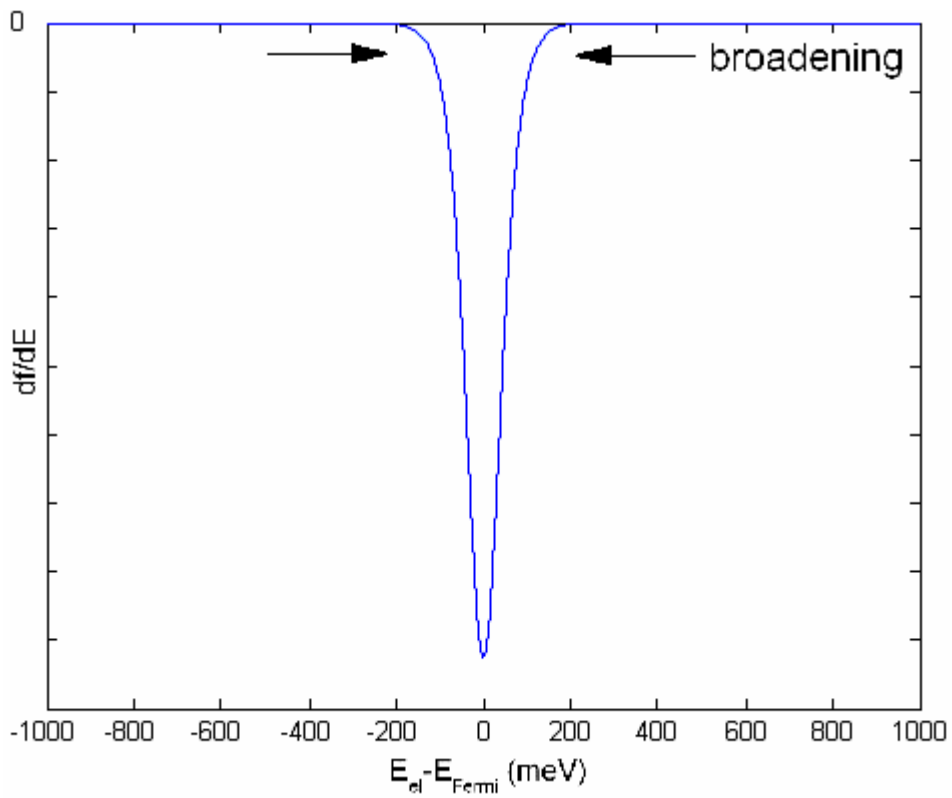


Fig.5.3.4 Derivative of Fermi-Dirac distribution function with respect to the energy of electron at room temperature (300K).

5.3.2 Electron-transition rate

Fig.5.3.5 shows the dependence of total transition rate on the energy of electrons

in the lowest two conduction bands of 2.19nm [110]SiNW and with doping density of $10^{19}/\text{cm}^3$. The variation tendencies of the total transition rate for two bands are similar, but the transition rate of the second band is about two times larger than the transition rate of the first band. Peaks in the figure indicate the electronic states are corresponding to strong e-p coupling. Here we marked four typical electronic states. E1 and E3 denote two states corresponding to the strongest e-p coupling in the first conduction band. E2 denotes a common state corresponding to weak e-p coupling in the first conduction band. E4 denotes the state corresponding to the strongest e-p coupling in the second conduction band. For the sake of comparing contributions from different phonon modes, we plotted the specific transition rate of the four marked states with respect to every scattering process in following figures (Fig.5.3.6, Fig.5.3.7, Fig.5.3.8 and Fig.5.3.9).

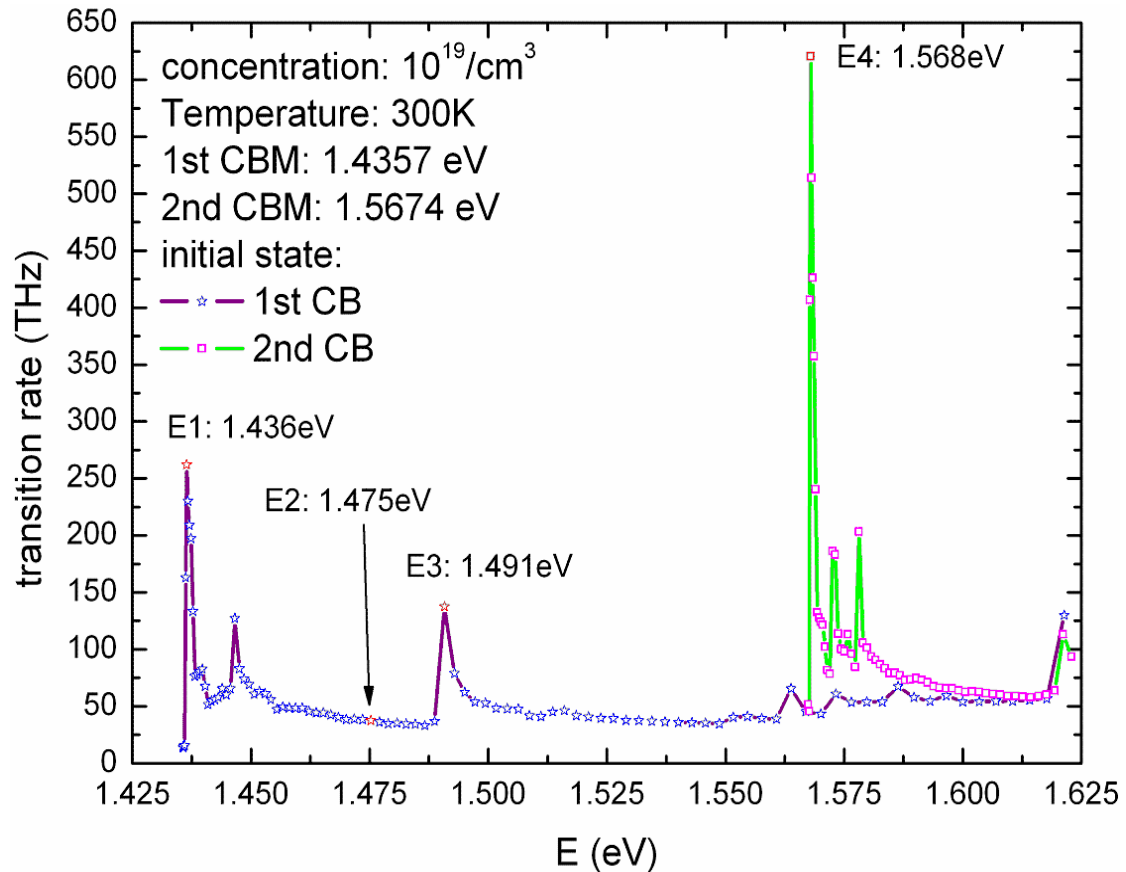


Fig.5.3.5 Dependence of transition rate on energy of electrons in the first conduction band (violet line) or in the second conduction band (green line) of 2.19nm [110]SiNW. Doping density is $10^{19}/\text{cm}^3$, temperature is 300K, energy of the first conduction band minimum (CBM) is 1.4357eV, energy of the second CBM is 1.5674eV.

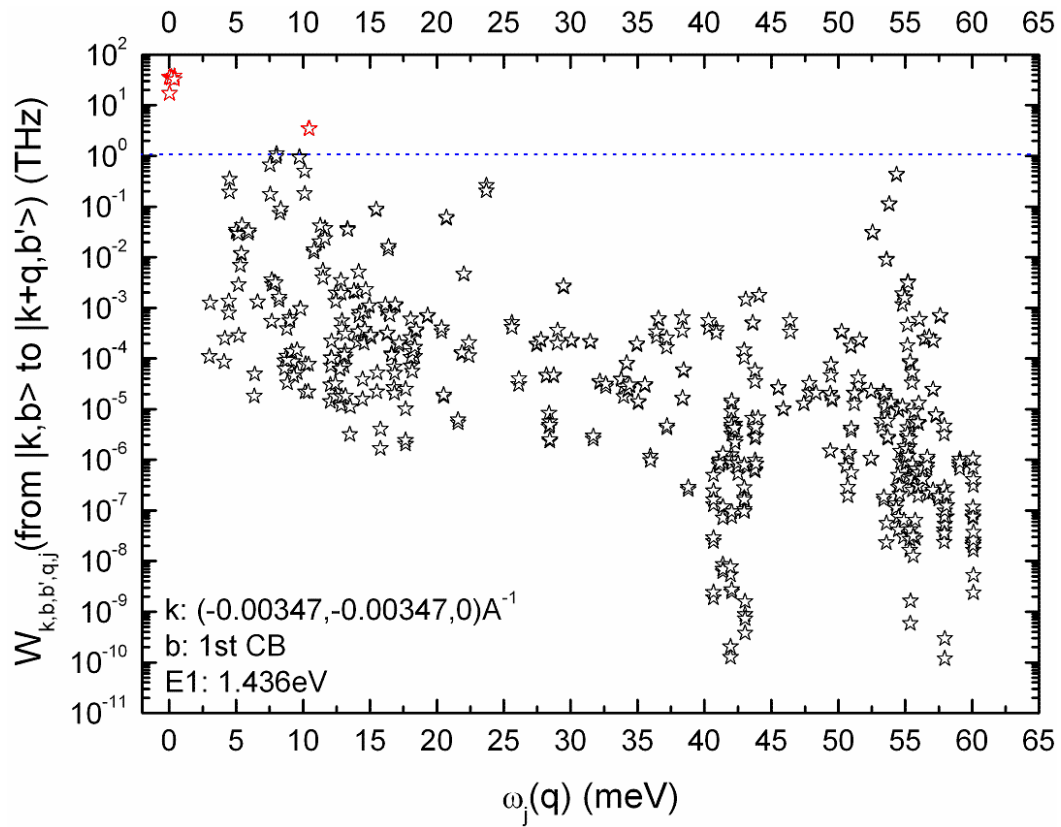


Fig.5.3.6 Transition rate versus frequency of phonon for electronic state E1.

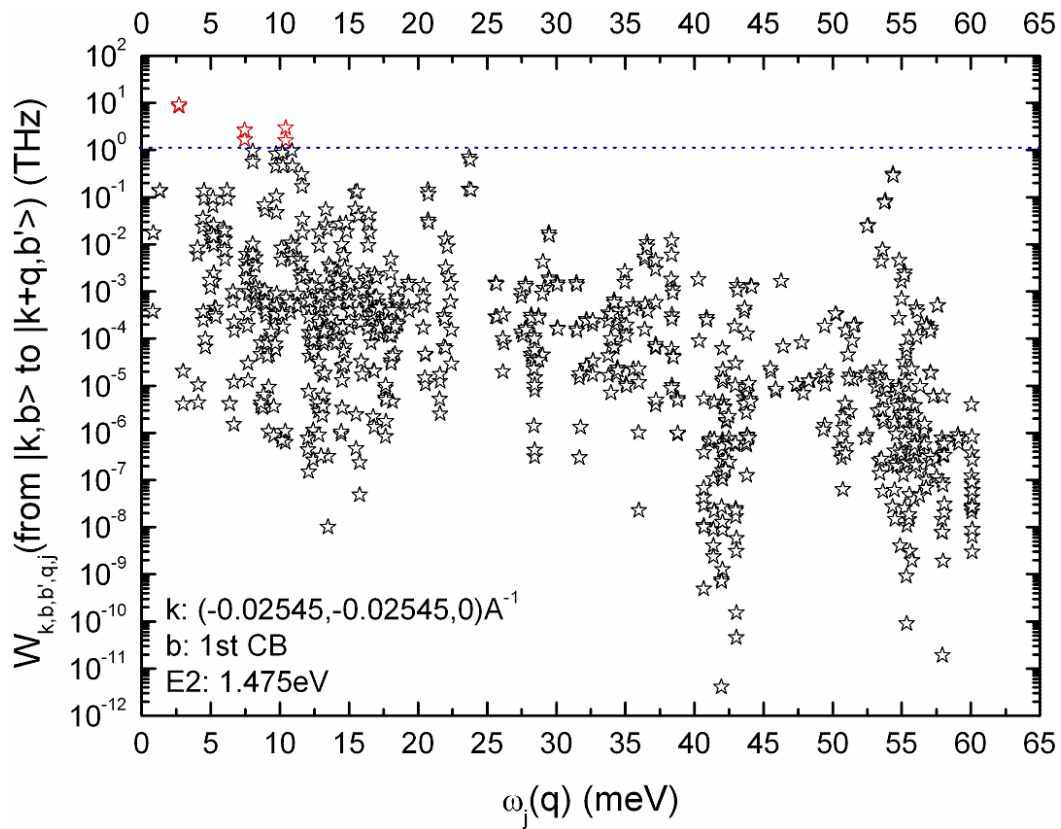


Fig.5.3.7 Transition rate versus frequency of phonon for electronic state E2.

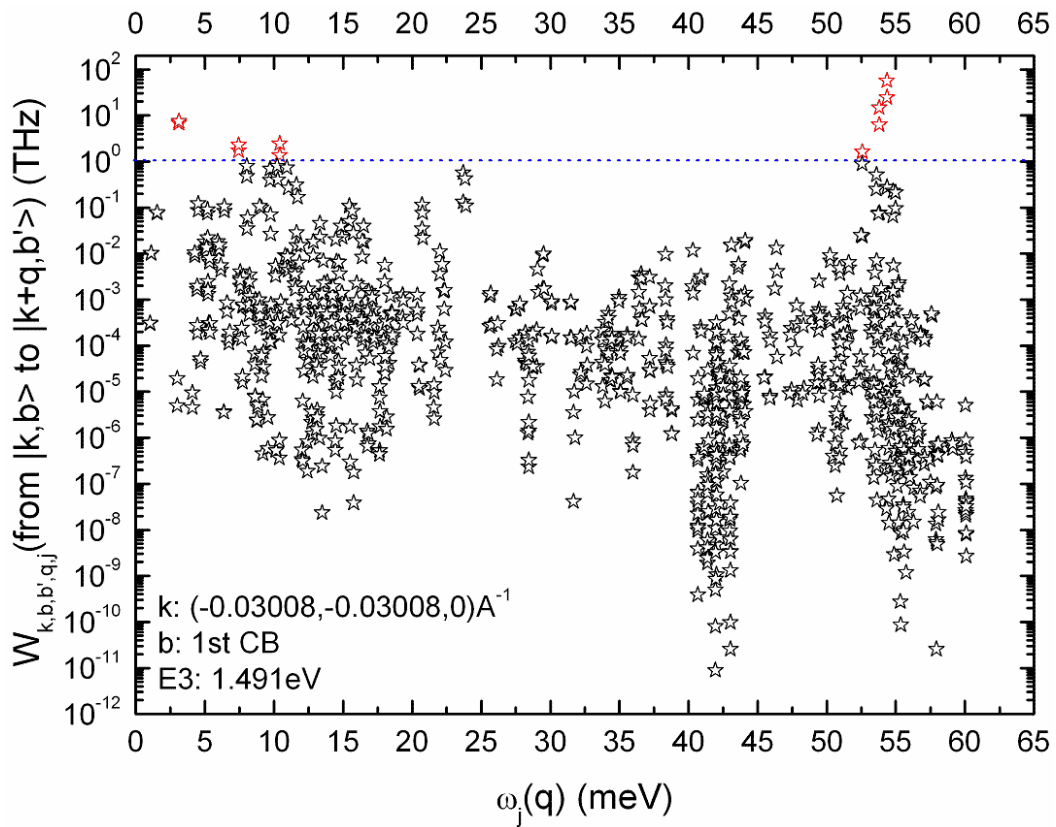


Fig.5.3.8 Transition rate versus frequency of phonon for electronic state E3.

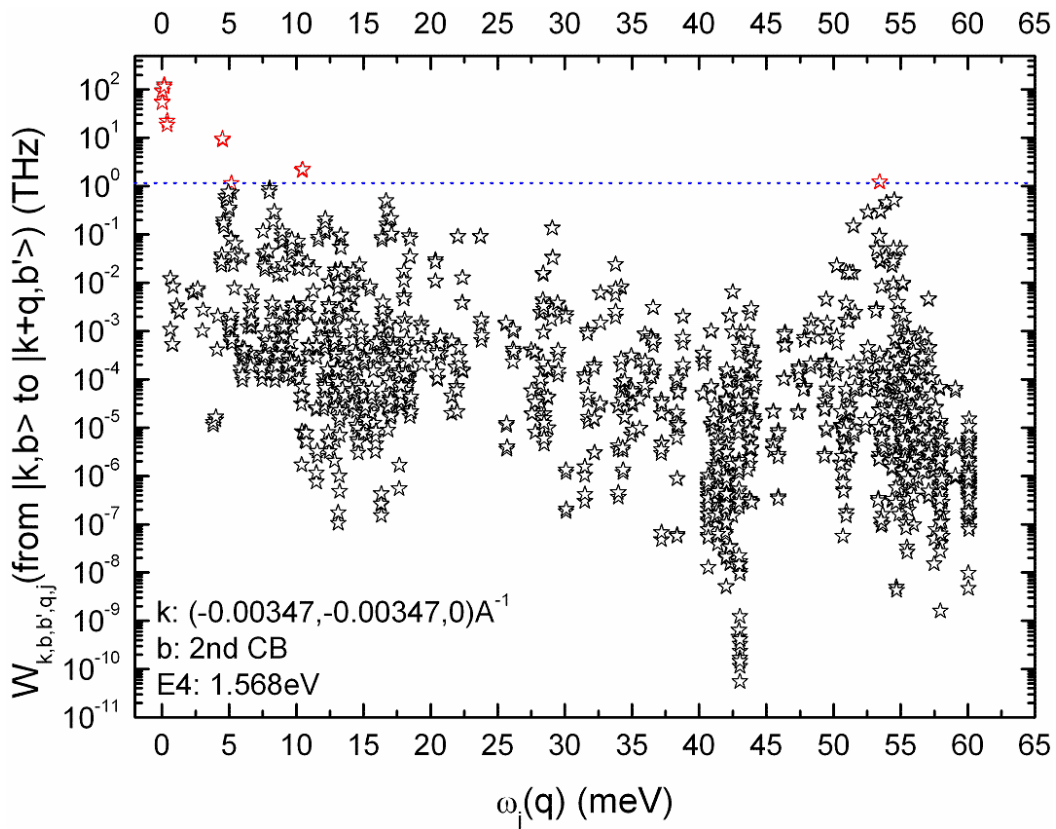


Fig.5.3.9 Transition rate versus frequency of phonon for electronic state E4.

In above figures, the blue dotted lines are corresponding to the transition rate of 1THz, and red stars denote all scattering processes corresponding transition rate larger than 1THz. These figures make clear to us that there are more and more phonon scattering of high-energy acoustic modes and optical modes from low electronic state E1 to high electronic state E3. That is to say, there is a transition of scattering mechanism from acoustic phonon scattering to optical phonon scattering when the energy of electron increases within the same conduction band. For electronic state E4, it's also a state of low energy in the second conduction band, so the scattering process is similar as the electronic state E1, i.e. the acoustic phonon scattering makes a major contribution. But the transition rate of E4 is larger because there are more electronic states in the vicinity of E4 than E1 as shown in Fig.5.1.2.

5.3.3 Low-field mobility versus diameter

We calculated the low-field mobility of electrons in [110]SiNW of different sizes at both low temperature (77K) and room temperature (300K) as shown in Fig.5.3.10. The low-field mobility of electrons increases with the diameter and in principle it should tend to reach the limit of bulk when the diameter grows larger and larger.

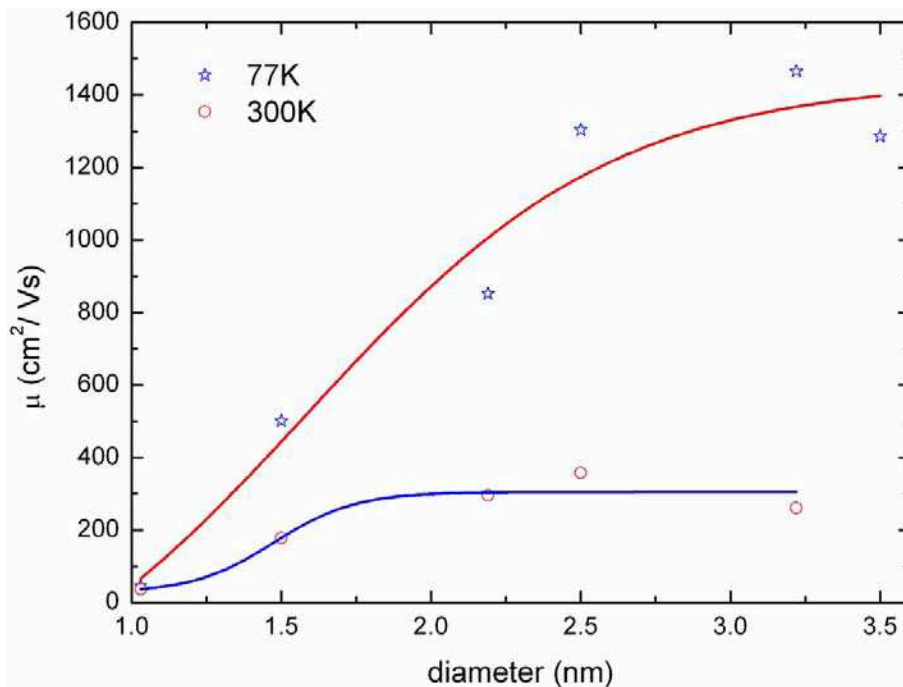


Fig.5.3.10 Dependence of low-field mobility on the diameter of [110]SiNW.

5.3.4 Low-field mobility versus temperature

We calculated the low-field mobility of electrons in 2.19nm [110]SiNW at different temperatures with low doping density ($10^{17}/\text{cm}^3$) or high doping density ($10^{19}/\text{cm}^3$) as shown in Fig.5.3.11. It can be concluded that the low-field mobility decreases in power law (Eq.5.3.1) with temperature. That's because there are more phonons and the broadening of Fermi-Dirac function increases with temperature, and correspondingly the e-p scattering increases rapidly.

$$\mu = \mu_{0K} + C_1 \cdot T + C_2 \cdot T^2 \quad (5.3.1)$$

where μ_{0K} denotes the low-field mobility at absolute zero, C_1 and C_2 are parameters. From Fig.5.3.11, we can get $\mu_{0K} = 1704.78$ (cm^2/Vs), $C_1 = -19.12$ (cm^2/VsK), and $C_2 = 0.1382$ (cm^2/VsK^2).

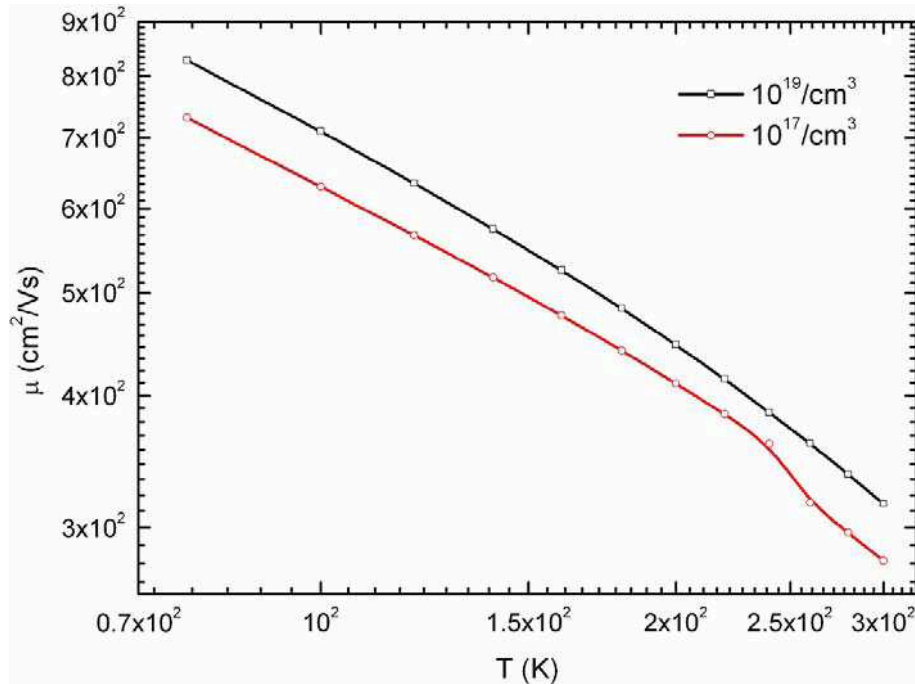


Fig.5.3.11 Dependence of low-field mobility on the temperature of 2.19nm [110]SiNW with low doping density of electron ($10^{17}/\text{cm}^3$, red line) and high doping density of electron ($10^{19}/\text{cm}^3$, black line). We use double logarithmic scale. The solid lines denote fitting with Eq.5.3.1. The empty circles are data from calculation.

§5.4 Summary

This chapter introduced electronic structures, phononic structures of SiNWs along different orientations such as [001], [110], [111] and [112]. We also discussed about the e-p coupling and transport properties of SiNWs in detail. In particular we studied the low-field mobility and offered a detailed discussion on the e-p coupling effect in the transport properties of [110]SiNWs in the third section of this chapter, like the dependence of mobility on temperature, the effect of size, and the effect of doping density.

Unlike the phonon scattering, the ionized impurity scattering¹⁰⁸ is elastic in nature and thus it cannot control the transport process alone in the presence of an external field. It must be accompanied by some dissipative processes i.e. phonon scattering to derive a proper distribution of electrons. Another kind of scattering mechanism is scattering from surface roughness¹⁷¹ which neglects all collisions in principle. Therefore, the surface roughness affects the transport of electrons by changing the wave function. We will study the surface roughness effect in transport properties of SiNWs within the e-p coupling regime with our code in the future.

With this method, people are able to study real transport behavior of carriers in electronic devices on a complete microscopic level and it can be expected that there would be more studies on the transport properties of SiNWs. The knowledge of e-p coupling effect in transport properties is not only very important in fundamental physics but very helpful in the development of high-performance electronic devices. The future of the new method is extensive.

Appendix A Y. M. Niquet TB model

In the diagonal-block Hamiltonian of Boykin's model⁶⁸ only the on-site term (diagonal element) is nonzero. Thus the valence band deformation potential d_v (see Ref.1) is incorrect and the Hamiltonian matrix doesn't obey rotational invariance in Boykin's model. All these deficiencies come from the 'diagonal' assumption. To solve this problem, Y. M. Niquet improved traditional $sp^3d^5s^*$ tight-binding Hamiltonian by adding the off-diagonal couplings between different orbitals of the same atom into the diagonal block⁶¹. The detailed form is as follows:

1) s (s^*) orbital:

$$\hat{H}_s = E_s^0 + \alpha_s \frac{\Delta\Omega}{\Omega_0} \quad (\text{A.1})$$

Here Ω_0 denotes the volume of regular tetrahedron with center at a silicon atom, $\Delta\Omega$ denotes the deviation of volume from equilibrium value. E_s^0 is the energy of s orbital at equilibrium. α_s is a parameter.

2) p orbitals (p_x, p_y, p_z):

$$\hat{H}_p = (E_p^0 + \alpha_p \frac{\Delta\Omega}{\Omega_0})\hat{I} + \sum_j^{NN} \beta_p(d) \begin{bmatrix} l^2 - \frac{1}{3} & ml & nl \\ ml & m^2 - \frac{1}{3} & mn \\ nl & mn & n^2 - \frac{1}{3} \end{bmatrix} \quad (\text{A.2})$$

$$\beta_p(d) = \beta_p^{(0)} + \beta_p^{(1)} \frac{d-d_0}{d_0}$$

Here $l_{ij} = \bar{x} \cdot R_{ij} / d_{ij}$, $m_{ij} = \bar{y} \cdot R_{ij} / d_{ij}$, $n_{ij} = \bar{z} \cdot R_{ij} / d_{ij}$, and \bar{x} , \bar{y} , \bar{z} are unit vectors. d denotes the real length of bond and d_0 denotes the equilibrium value.

$\beta_p^{(0)}$ and $\beta_p^{(1)}$ are parameters.

3) d orbitals (d_{yz} , d_{zx} , d_{xy} , $d_{x^2-y^2}$, $d_{3z^2-r^2}$):

$$\hat{H}_d = (E_d^0 + \alpha_d \frac{\Delta\Omega}{\Omega_0}) \hat{I} + \sum_j^{NN} \beta_d(d) \begin{bmatrix} l^2 - \frac{1}{3} & -ml & -nl & mn & -\frac{1}{\sqrt{3}}mn \\ -ml & m^2 - \frac{1}{3} & -mn & -nl & -\frac{1}{\sqrt{3}}nl \\ -nl & -mn & n^2 - \frac{1}{3} & 0 & \frac{2}{\sqrt{3}}ml \\ mn & -nl & 0 & n^2 - \frac{1}{3} & \frac{2}{\sqrt{3}}u \\ -\frac{1}{\sqrt{3}}mn & -\frac{1}{\sqrt{3}}nl & \frac{2}{\sqrt{3}}ml & \frac{2}{\sqrt{3}}u & \frac{1}{3} - n^2 \end{bmatrix} + \sum_j^{NN} \gamma_d(d) \begin{bmatrix} m^2 n^2 & lmn^2 & lm^2 n & mun & mvn \\ lmn^2 & l^2 n^2 & l^2 mn & lun & lvn \\ lm^2 n & l^2 mn & l^2 m^2 & lum & lvm \\ mun & lun & lum & u^2 & uv \\ mvn & lvn & lvm & uv & v^2 \end{bmatrix} \quad (\text{A.3})$$

$$\beta_d(d) = \beta_d^{(0)} + \beta_d^{(1)} \frac{d-d_0}{d_0}$$

$$\gamma_d(d) = \gamma_d^{(0)} + \gamma_d^{(1)} \frac{d-d_0}{d_0}$$

Here $u = (l^2 - m^2)/2$, $v = (3n^2 - 1)/2\sqrt{3}$. $\beta_d^{(0)}$, $\beta_d^{(1)}$, $\gamma_d^{(0)}$ and $\gamma_d^{(1)}$ are parameters.

4) coupling between s and s^* :

$$\hat{H}_{ss^*} = \sum_j^{NN} \gamma_{ss^*}^{(j)}(d) \quad (\text{A.4})$$

$$\gamma_{ss^*}^{(j)}(d) = \gamma_{ss^*}^{(j)(0)} + \gamma_{ss^*}^{(j)(1)} \frac{d-d_0}{d_0}$$

Here $\gamma_{ss^*}^{(j)(0)}$ and $\gamma_{ss^*}^{(j)(1)}$ are parameters.

5) couplings between s (s^*) and p (p_x, p_y, p_z):

$$\hat{H}_{sp} = \sum_j^{NN} \beta_{sp}^{(j)}(d) [l \ m \ n] \quad (\text{A.5})$$

$$\beta_{sp}^{(j)}(d) = \beta_{sp}^{(j)(0)} + \beta_{sp}^{(j)(1)} \frac{d-d_0}{d_0}$$

Here $\beta_{sp}^{(j)(0)}$ and $\beta_{sp}^{(j)(1)}$ are parameters.

6) couplings between s (s^*) and d ($d_{yz}, d_{zx}, d_{xy}, d_{x^2-y^2}, d_{3z^2-r^2}$):

$$\hat{H}_{sd} = \sum_j^{NN} \beta_{sd}^{(j)}(d) [mn \ nl \ ml \ u \ v] \quad (\text{A.6})$$

$$\beta_{sd}^{(j)}(d) = \beta_{sd}^{(j)(0)} + \beta_{sd}^{(j)(1)} \frac{d-d_0}{d_0}$$

Here $\beta_{sd}^{(j)(0)}$ and $\beta_{sd}^{(j)(1)}$ are parameters.

7) couplings between p (p_x, p_y, p_z) and d ($d_{yz}, d_{zx}, d_{xy}, d_{x^2-y^2}, d_{3z^2-r^2}$):

$$\hat{H}_{pd} = \sum_j^{NN} \beta_{pd}^{(j)}(d) \begin{bmatrix} 0 & n & m & l & -\frac{1}{\sqrt{3}}l \\ n & 0 & l & -m & -\frac{1}{\sqrt{3}}m \\ m & l & 0 & 0 & \frac{2}{\sqrt{3}}n \end{bmatrix} + \sum_j^{NN} \gamma_{pd}^{(j)}(d) \begin{bmatrix} lmn & l^2n & l^2m & lu & lv \\ m^2n & lmn & m^2l & mu & mv \\ mn^2 & n^2l & lmn & nu & nv \end{bmatrix} \quad (\text{A.7})$$

$$\beta_{pd}(d) = \beta_{pd}^{(0)} + \beta_{pd}^{(1)} \frac{d - d_0}{d_0}$$

$$\gamma_{pd}(d) = \gamma_{pd}^{(0)} + \gamma_{pd}^{(1)} \frac{d - d_0}{d_0}$$

Here $\beta_{pd}^{(0)}$, $\beta_{pd}^{(1)}$, $\gamma_{pd}^{(0)}$ and $\gamma_{pd}^{(1)}$ are parameters.

Appendix B Ballistic transport of CNT heterojunctions

The first section of this appendix introduces the structures of single-wall carbon nanotube (CNT) and carbon nanotube heterojunction. In the second section we introduce the theoretical background of ballistic transport. In the third section we introduce the anomalous conductance of (12,0)/(9,0)/(12,0) junction and propose a reasonable explanation. In the fourth section a universal relation between the ballistic conductance and the rotation angle for metallic CNT junctions is presented. The last section introduces ballistic conductance of a typical T junction and a typical Cross junction. These theoretical studies strengthened our understanding of the transport properties of CNTs.

§B.1 CNT heterojunction

A CNT heterojunction can be made by joining two different CNTs together with pentagon-heptagon (p-h) pairs or other structural defects¹⁸².

Terrones *et al.* created ‘X’, ‘Y’ and ‘T’ single-wall carbon nanotube junctions experimentally by controlled electron beam exposure of crossing tubes at elevated temperatures¹⁸³. The structures are shown in Fig.B.1.1. and Fig.B.1.2.

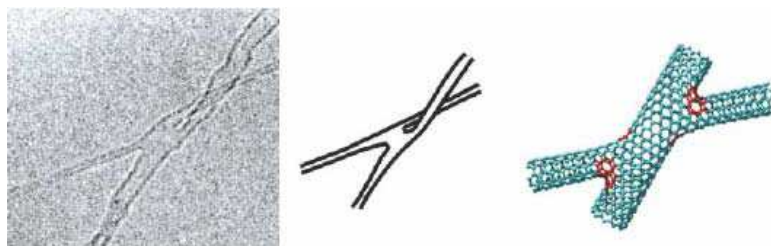


Fig.B.1.1 High-resolution transmission electron microscopy (HRTEM) image and molecular model of an ‘X’ junction.¹⁸³

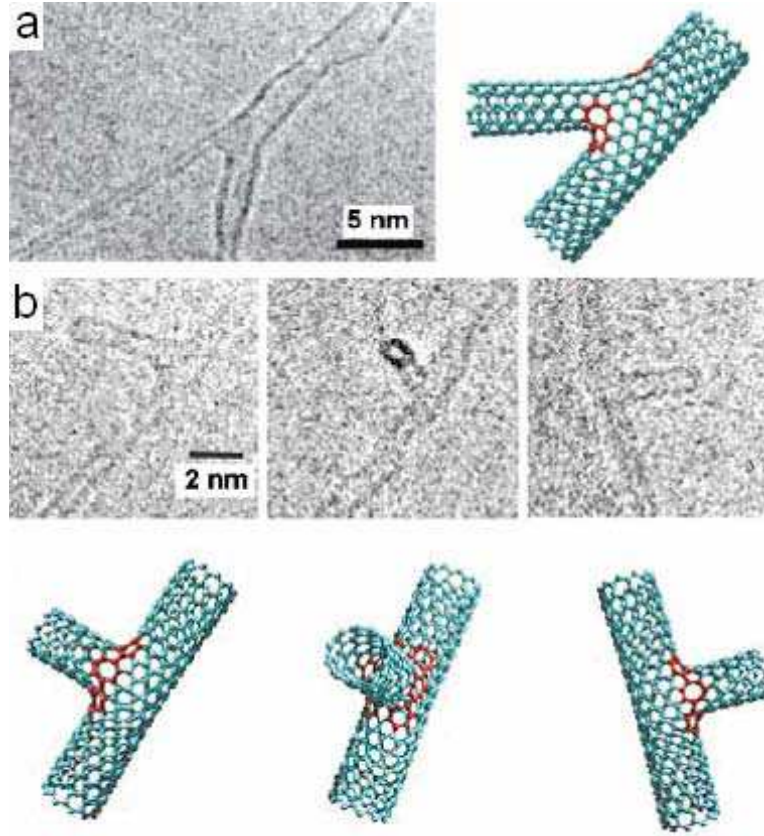


Fig.B.1.2 HRTEM images and molecular models of a ‘Y’ junction (a) and three ‘T’ junctions (b).¹⁸³

Single-wall carbon nanotube junction is one of the smallest and simplest electronic devices. CNT junctions have a lot of interesting transport properties^{184,185} and potential applications¹⁸⁷⁻¹⁸⁹. Thus we studied systematically the ballistic transport properties of CNT junctions with tight-binding model and nonequilibrium Green’s function (NEGF) method.

Structure of CNT

As shown in Fig.B.1.3, a carbon nanotube can be made by rolling up a piece of graphene. In the figure, a_1 and a_2 denote primitive translation vectors of graphene. \bar{C}_h is chiral vector and its definition is $\bar{C}_h = na_1 + ma_2 \equiv (n, m)$, here n and m are integers and $0 \leq m \leq n$. It’s customary to describe a CNT as (n, m) . θ is called

chiral angle. \vec{T} is translation vector and determined by $\vec{T} = t_1 a_1 + t_2 a_2 \equiv (t_1, t_2)$, here $t_1 = \frac{2m+n}{d_R}$ and $t_2 = -\frac{2n+m}{d_R}$. $d_R \equiv \text{gcd}(2m+n, m+2n)$ and ‘gcd’ means ‘greatest common divisor’. In fact \vec{T} is just the primitive translation vector of CNT. A zigzag nanotube corresponds to the case of $m=0$, that is $\vec{C}_h = (n,0)$, and an armchair nanotube corresponds to the case of $n=m$, or $\vec{C}_h = (n,n)$. All other (n,m) chiral vectors correspond to chiral nanotubes. Of special interest is the fact that the electronic structure of a carbon nanotube can be either metallic or semiconducting depending on its diameter and chirality. According to band-folding theory¹⁸², a carbon nanotube is metallic in the case of $n-m=3d$ and semiconducting in other cases, where d is an integer. Therefore, almost one third of the CNTs are metallic and the other two thirds are semiconducting.

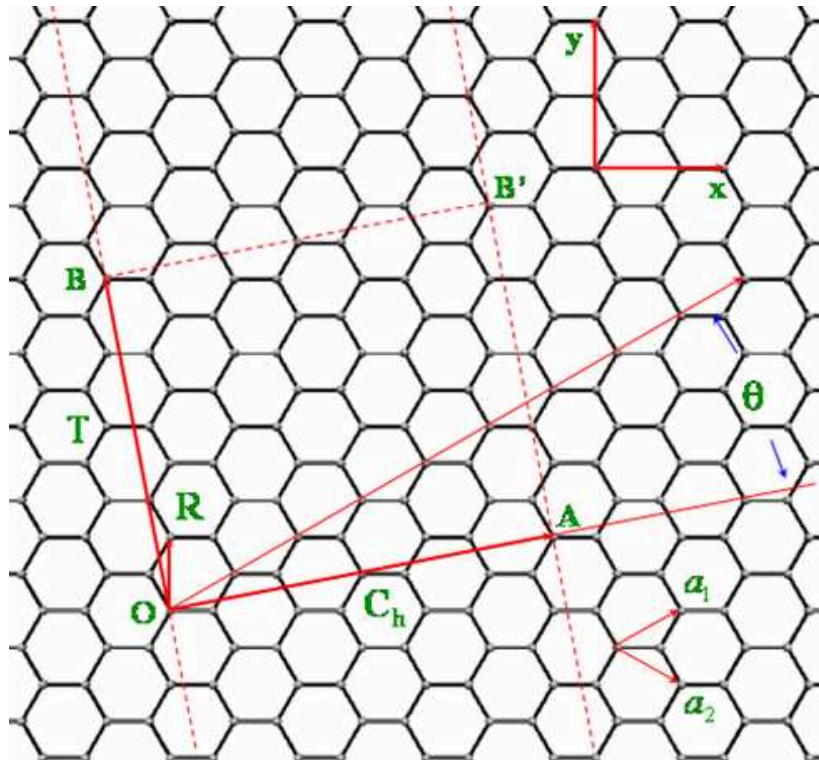
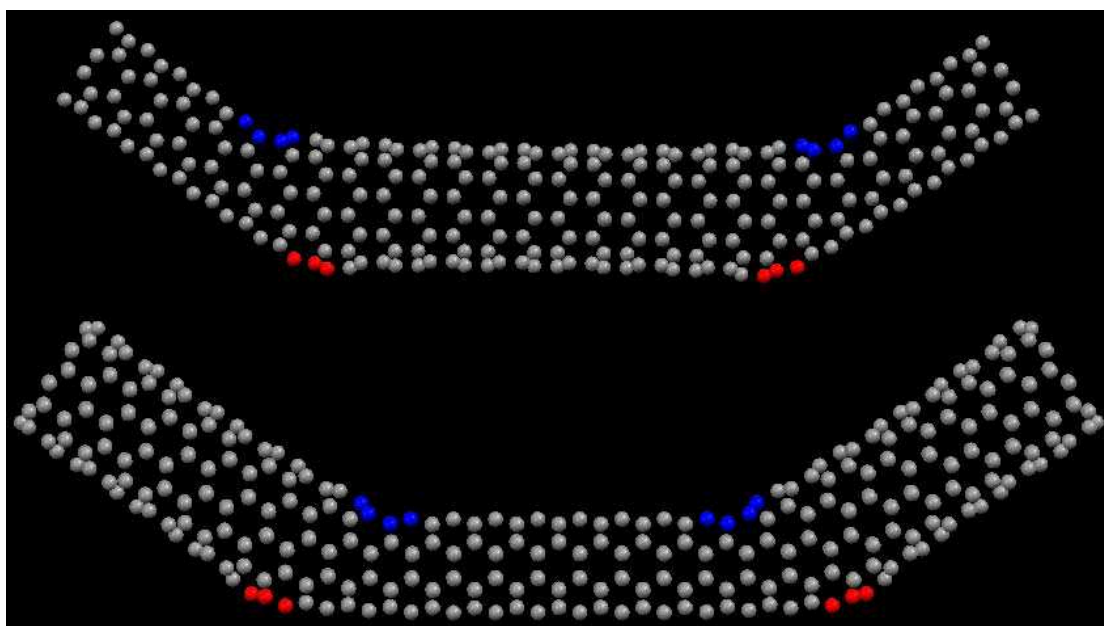


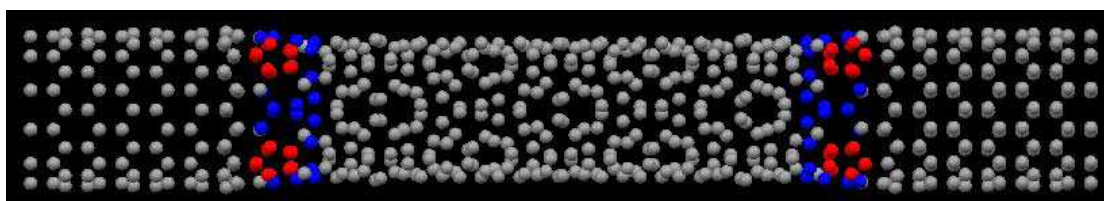
Fig.B.1.3 Planar schematic diagram of atomic structure of CNT.

Structure of CNT heterojunction

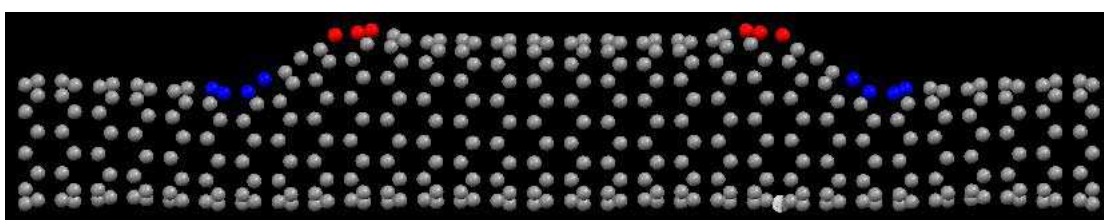
We can join two nanotubes of different chirality together by inserting some structural defects like pentagon-heptagon pairs or tetragon-octagon pairs. Fig.B.1.4 shows a (4,4)/(9,0)/(4,4) junction and its counterpart, that is (9,0)/(4,4)/(9,0) junction. Fig.B.1.5 shows a (12,0)/(8,4)/(12,0) junction and Fig.B.1.6 shows a (9,0)/(12,0)/(9,0) junction. In these figures, we use blue balls for heptagons and red balls for pentagons.



B.1.4 Molecular models of junctions (4,4)/(9,0)/(4,4) (top) and (9,0)/(4,4)/(9,0) (bottom).



B.1.5 Molecular model of (12,0)/(8,4)/(12,0) junction.



B.1.6 Molecular model of (9,0)/(12,0)/(9,0) junction

Structure of T junction and Cross junction

We can go further, and construct more complicated structures from simple CNT junctions mentioned above. For example, Fig.B.1.7 shows a T junction and a Cross junction.

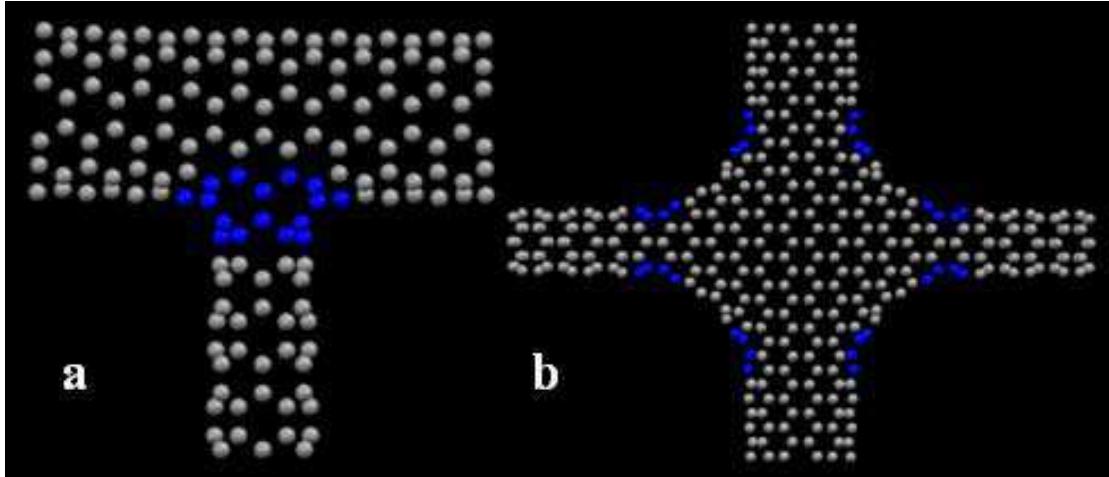


Fig.B.1.7 Molecular models: (a) T junction (6,6)/(6,0)/(6,6), (b) Cross junction (6,6)/(6,0)/(6,6)/(6,0)

§B.2 Theoretical background

The theoretical background of ballistic transport is introduced in this section.

Ballistic transport

The mean free path of electrons in CNT is very large and always larger than the length of channel in nano-electronic devices, and consequently electrons pass through the nanotube without collision. It's called ballistic transport^{191,192}.

The ballistic transport conductance is

$$G = \frac{2e^2}{h} \cdot \frac{T}{R} \quad (\text{B.2.1})$$

which is known as the *Landauer formula*^{193,194}. For detailed derivation please refer to the section 1.2 of Ref.¹⁹². In Eq.B.2.1, T is the transmission coefficient and R is the reflection coefficient. If we measure the potential from two leads, then $R \approx 1$, and

the conductance reads

$$G(E) = \frac{2e^2}{h} \cdot T(E) \quad (\text{B.2.2})$$

because the transmission coefficient always depends on the energy of electron.

Tight-binding Hamiltonian

A lot of tight-binding models¹⁹⁵⁻¹⁹⁸ of carbon can be used to calculate the ballistic conductance of carbon nanotubes. Louie *et al.* proposed a simple model¹⁸⁵ with one π orbital.

$$H = -V_{pp\pi} \sum_{\langle i,j \rangle} a_i^+ a_j + c.c. \quad (\text{B.2.3})$$

Where $\langle i, j \rangle$ denotes the summation is over all nearest neighbors, and $V_{pp\pi}$ (2.7eV) is coupling between nearest neighbors. This model is used widely in studies of carbon nanotubes and graphene. Here we will also use it to study the ballistic conductance of CNT junctions.

Nonequilibrium Green's function (NEGF)^{191,199-209}

In this part we will introduce the method of nonequilibrium Green's function to calculate the transmission coefficient and ballistic conductance.



Fig.B.2.1 Schematic diagram of current. 'L' is left lead, 'R' is right lead, 'C' is conductor. Red arrows denote the current flowing in or out.

Fig.B.2.1 shows a system with a conductor in the middle and two infinite long leads at the two sides. The transmission coefficient can be expressed in terms of the Green's functions of the conductors and the coupling of the conductor to the leads²⁰⁶:

$$T = \text{Tr}(\Gamma_L G_C^r \Gamma_R G_C^a) \quad (\text{B.2.4})$$

Here $\Gamma_{L(R)}$ is function that describes the coupling between the conductor and the left (right) lead, $G_C^{r(a)}$ is retarded (advanced) Green's function of the conductor. To compute $\Gamma_{L(R)}$ and $G_C^{r(a)}$, we start from the equation for the Green's function of the whole system:

$$(\varepsilon - H)G = I \quad (\text{B.2.5})$$

where $\varepsilon = E + i \cdot \eta$ and η is infinitesimal. According to the structure as shown in Fig.B.2.1, we can partition the Green's function of the whole system into submatrices:

$$\begin{pmatrix} G_L & G_{LC} & G_{LCR} \\ G_{CL} & G_C & G_{CR} \\ G_{LRC} & G_{RC} & G_R \end{pmatrix} = \begin{pmatrix} (\varepsilon - H_L) & h_{LC} & 0 \\ h_{LC}^+ & (\varepsilon - H_C) & h_{CR} \\ 0 & h_{CR}^+ & (\varepsilon - H_R) \end{pmatrix}^{-1} \quad (\text{B.2.6})$$

where $H_{C(L,R)}$ is the block Hamiltonian of conductor (left lead, right lead), $h_{LC(CR)}$ is the coupling Hamiltonian between left lead and the conductor or between the conductor and the right lead. We can obtain the Green's function of the conductor from Eq.B.2.6 directly,

$$G_C = (\varepsilon - H_C - \Sigma_L - \Sigma_R)^{-1} \quad (\text{B.2.7})$$

where $\Sigma_{L(R)}$ is the self-energy correction of the left (right) lead. The definition of coupling function is,

$$\Gamma_{\{L,R\}} = i \cdot [\Sigma_{\{L,R\}}^r - \Sigma_{\{L,R\}}^a] \quad (\text{B.2.8})$$

Until now, we have discussed the system with infinite long leads, but in calculations computer can deal with finite system only. Therefore, we need to use a technique called layered Green's function^{204,205}. From now on, we will introduce the layered Green's function method which brings the calculation into practice.

As is known, a quasi-one-dimensional lattice can be divided into layers. Therefore, we can construct the tight-binding Hamiltonian of the quasi-one-dimensional system layer by layer. If the layer is big enough, only the diagonal block corresponding to the same layer and the coupling block between two nearest layers

are nonzero. Then we can rewrite the equation of Green's function as follows:

$$\begin{aligned}
(\varepsilon - H_{00})G_{00} &= I + H_{01}G_{10} \\
(\varepsilon - H_{00})G_{10} &= H_{01}^+G_{00} + H_{01}G_{20} \\
&\dots\dots \\
(\varepsilon - H_{00})G_{n0} &= H_{01}^+G_{n-1,0} + H_{01}G_{n+1,0}
\end{aligned}$$

where H_{nm} (G_{nm}) is the Hamiltonian (Green's function) element between the layer n and the layer m . We use the same pristine CNT for both leads, so

$$H_{00} = H_{11} = \dots$$

and

$$H_{01} = H_{12} = \dots$$

We define two transfer matrices:

$$T = t_0 + \tilde{t}_0 t_1 + \tilde{t}_0 \tilde{t}_1 t_2 + \dots + \tilde{t}_0 \tilde{t}_1 \tilde{t}_2 \dots t_n \quad (\text{B.2.9})$$

and

$$\bar{T} = \tilde{t}_0 + t_0 \tilde{t}_1 + t_0 t_1 \tilde{t}_2 + \dots + t_0 t_1 t_2 \dots \tilde{t}_n \quad (\text{B.2.10})$$

where

$$t_0 = (\varepsilon - H_{00})^{-1} H_{01}^+$$

and

$$\tilde{t}_0 = (\varepsilon - H_{00})^{-1} H_{01}$$

We can calculate the transfer matrices iteratively from Eq.B.2.9 and Eq.B.2.10. And then the Green's function of the conductor is

$$G_C(E) = (\varepsilon - H_C - H_{01}T - H_{01}^+\bar{T})^{-1} \quad (\text{B.2.11})$$

Compared with Eq.B.2.7, we find

$$\Sigma_L = H_{01}^+\bar{T} \quad (\text{B.2.12})$$

and

$$\Sigma_R = H_{01}T \quad (\text{B.2.13})$$

then the coupling functions will be

$$\Gamma_L = -\text{Im}(H_{01}^+ \bar{T}) \quad (\text{B.2.14})$$

and

$$\Gamma_R = -\text{Im}(H_{01} \bar{T}) \quad (\text{B.2.15})$$

From the Green's function theory, the electronic density of state (DOS) can be obtained from the Green's function directly

$$N(E) = -\frac{1}{\pi} \text{Im}[\text{Tr}(G(E))] \quad (\text{B.2.16})$$

With the nonequilibrium Green's function method and the *Landauer formula*, we can calculate the ballistic conductance of quasi-one-dimensional nanomaterials. For example, we studied the ballistic conductance and the electronic density of state for pristine CNTs (12,0) and (9,0), and the results are shown in Fig.B.2.2. The peaks of DOS are consistent with the steps of conductance. Because every peak of DOS corresponds to a new electronic band, i.e. a new conducting channel for electrons, then the conductance corresponds to a step.

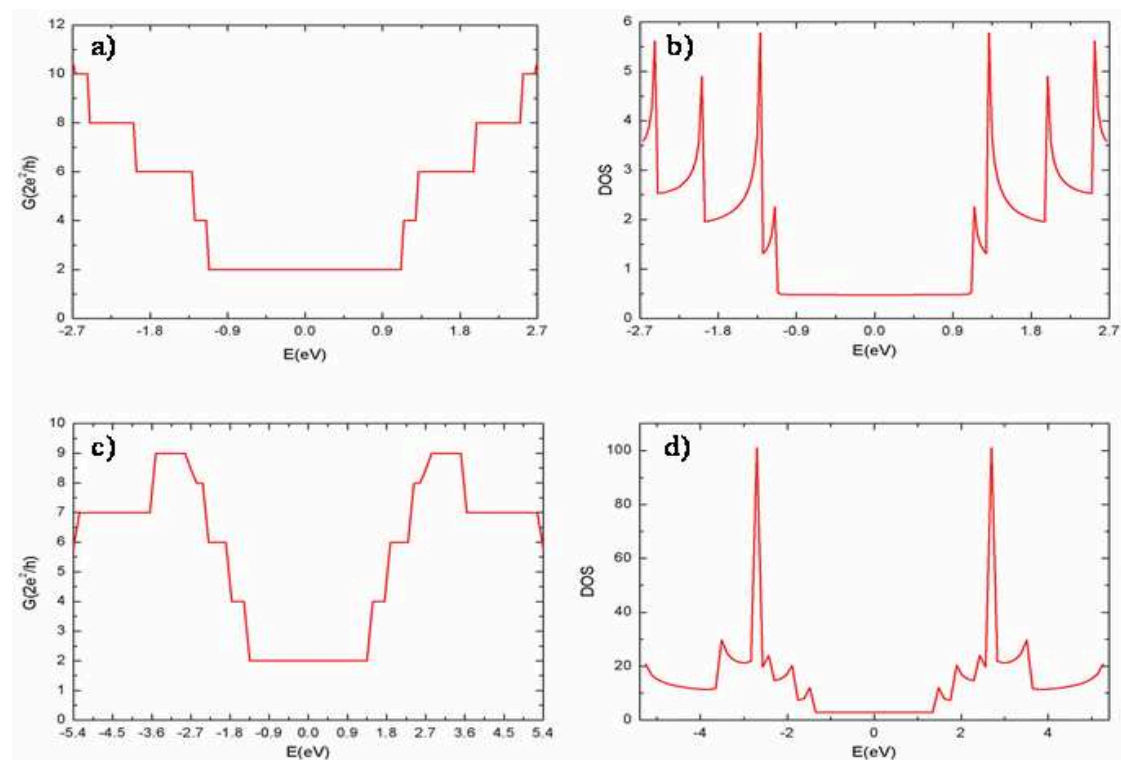


Fig.B.2.2 a) ballistic conductance of (12,0), b) electronic density of state of (12,0), c) ballistic conductance of (9,0), d) electronic density of state of (9,0)

§B.3 Anomalous conductance of (12,0)/(9,0)/(12,0) junction

According to Ohm's law, the conductance of conductor should decrease with increasing the length. However, in our studies¹⁹⁰ on length-dependent transport behaviors of (12,0)/(n,m)/(12,0), we find the conductance of (12,0)/(9,0)/(12,0) increases and approaches to a limit when the length increases. This anomalous phenomenon denotes the ballistic transport is very different from the classic transport. The Ohm's law is not valid anymore when carbon nanotube enters into nano scale.

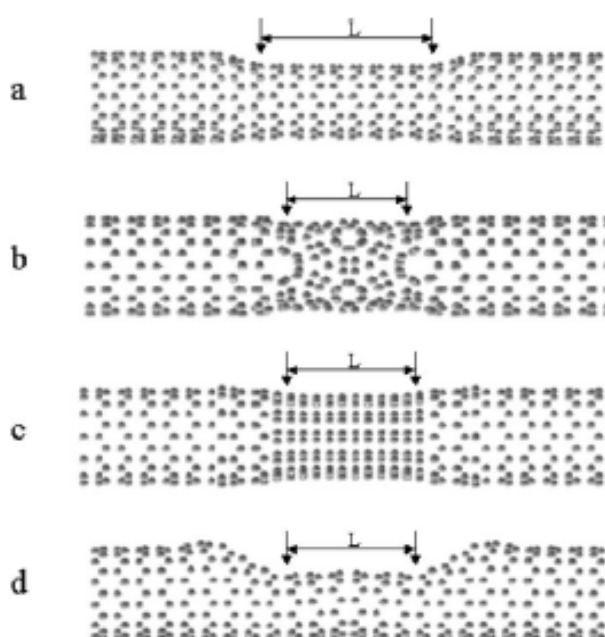


Fig.B.3.1 Side view of atomic structure of CNT junctions¹⁹⁰: a) (12,0)/(11,0)/(12,0), b) (12,0)/(8,4)/(12,0), c) (12,0)/(6,6)/(12,0), d) (12,0)/(9,0)/(12,0)

Fig.B.3.1 shows the atomic structures of CNT junctions in the study. We use metallic carbon nanotube (12,0) as leads, and use different type of nanotubes as conductor. We studied the relationship between ballistic conductance at Fermi level and the length of conductor. Results are shown in Fig.B.3.2. To study semiconducting CNTs we choose a zigzag tube (11,0) (Fig.B.3.1a) and a chiral tube (8,4) (Fig.B.3.1b). To study metallic CNTs we choose an armchair tube (6,6) (Fig.B.3.1c) and a zigzag tube (9,0) (Fig.B.3.1d).

Fig.B.3.2a, Fig.B.3.2b and Fig.B.3.2c show that the conductances at Fermi level

decrease exponentially with length of conductor. We can fit the curves with exponential law very well

$$G = G_1 e^{-\beta L} \quad (\text{B.3.1})$$

where L denotes the length of conductor. $1/\beta$ is called attenuation length which is an important physical parameter for electronic devices. G_1 is contact conductance.

The fitted values of parameters are listed in table B.3.1.

Table B.3.1 Parameters of length-dependent conductance

	G_1 ($2e^2/h$)	β (\AA^{-1})
(12,0)/(11,0)/(12,0)	1.066	0.132
(12,0)/(8,4)/(12,0)	0.820	0.552
(12,0)/(6,6)/(12,0)	0.371	0.801

However, in Fig.B.3.2d, the ballistic conductance of (12,0)/(9,0)/(12,0) increases exponentially to a limit with increasing length of conductor. We can describe this curve with

$$G = G_1 - G_2 e^{-\beta L} \quad (\text{B.3.2})$$

where G_1 is the limit of conductance, G_2 is a parameter corresponding to interface, β is inverse saturation length. And the fitted values are $G_1 = 1.383G_0$, $G_2 = 0.167G_0$ and $\beta = 3.492 \text{\AA}^{-1}$, where $G_0 \equiv 2e^2/h$.

To explain the two contrary length dependences of ballistic conductance at Fermi level as mentioned above, we studied the ballistic conductance spectra of four single-interface junctions (12,0)/(11,0), (12,0)/(8,4), (12,0)/(6,6) and (12,0)/(9,0) separately. And the results are shown in Fig.B.3.3.

From Fig.B.3.3, the first three junctions are semiconducting and the last one, or (12,0)/(9,0), is metallic. That is, there are barriers for electrons to transmit through the conductor in junctions (12,0)/(11,0)/(12,0), (12,0)/(8,4)/(12,0), and (12,0)/(9,0)/(12,0).

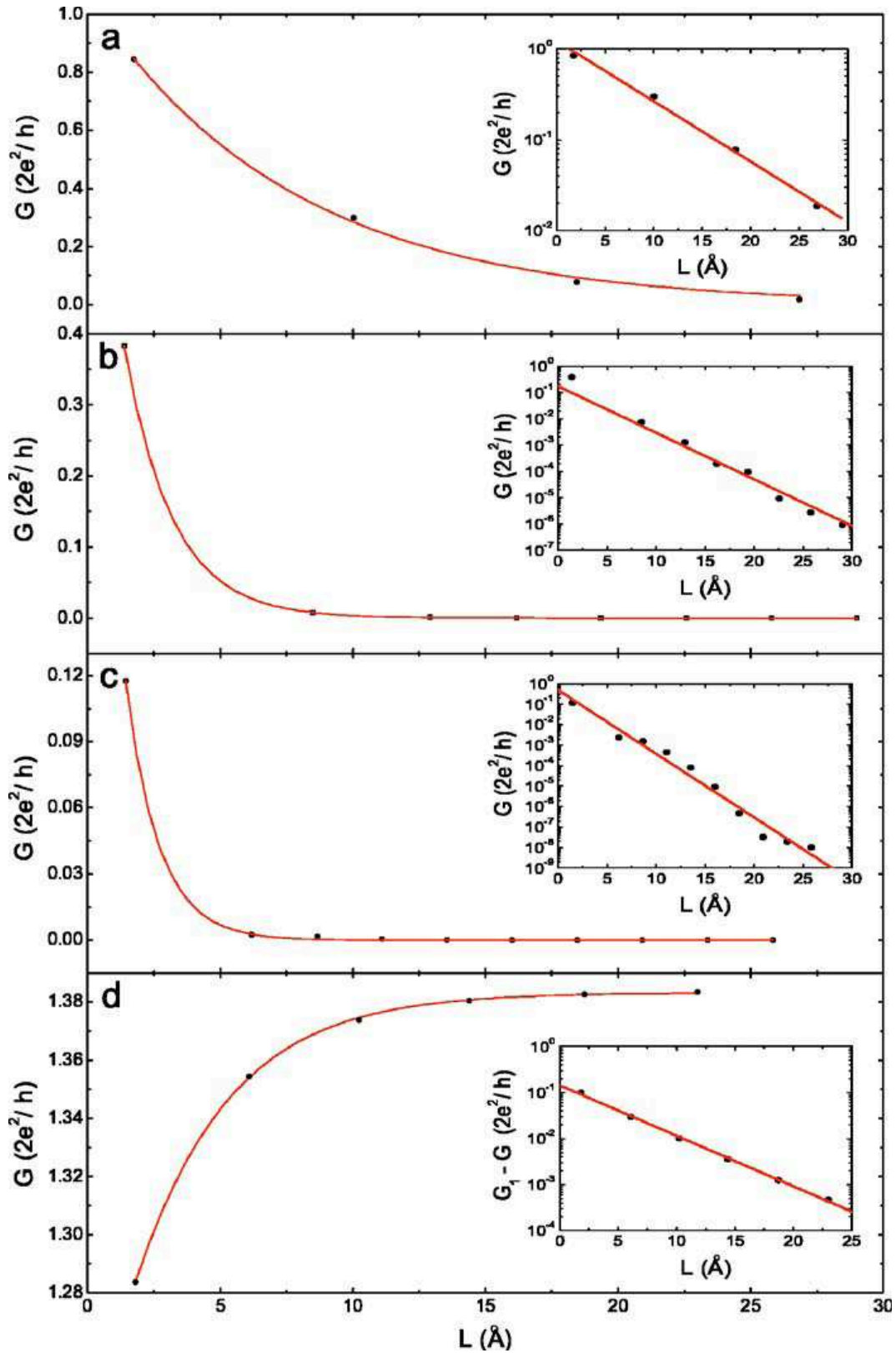


Fig.B.3.2 Length-dependent ballistic conductance at Fermi level for different CNT junctions¹⁹⁰: a) (12,0)/(11,0)/(12,0), b) (12,0)/(8,4)/(12,0), c) (12,0)/(6,6)/(12,0), d) (12,0)/(9,0)/(12,0). Insets are semi-log plots. Red solid lines denote fitting curves.

Black dots denote results from calculation.

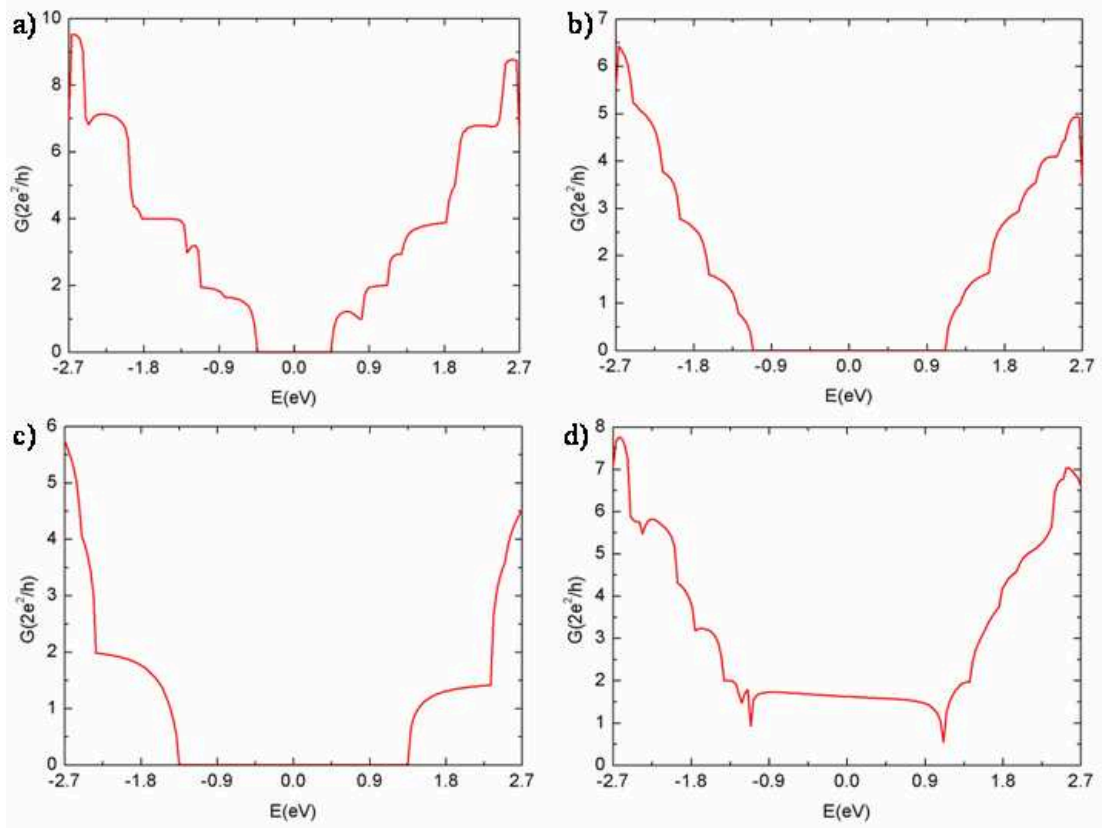


Fig.B.3.3 Ballistic conductance spectra for different single-interface junctions:

a) (12,0)/(11,0), b) (12,0)/(8,4), c) (12,0)/(6,6), d) (12,0)/(9,0).

According to the quantum mechanics, the transmission coefficient of electron decreases exponentially with increasing the width of barrier. It is in consistent with our results.

But for (12,0)/(9,0) junction, it's metallic. In the (12,0)/(9,0)/(12,0) junction, the injected electrons are multiscattered between two interfaces at (12,0)/(9,0) and (9,0)/(12,0) during they pass through the region of conductor, that is (9,0). Those electrons with wavelengths obeying the condition of resonance will tunnel through the junction without decay. We show the ballistic conductance spectra of (12,0)/(9,0)/(12,0) with different lengths of conductor in Fig.B.3.4. From bottom to top, the corresponding lengths of conductor are 1.8 Å, 10.2 Å, 18.7 Å and 23.0 Å, and corresponding to 1, 3, 5 and 6 unit cells of (9,0) respectively. The peaks of value $2G_0$ around Fermi level are corresponding to resonant tunneling¹⁹⁰. With increasing the length, the peak (indicated by black arrow) moves towards the Fermi level (dotted

line), and resulting in an increase of the conductance at Fermi level.

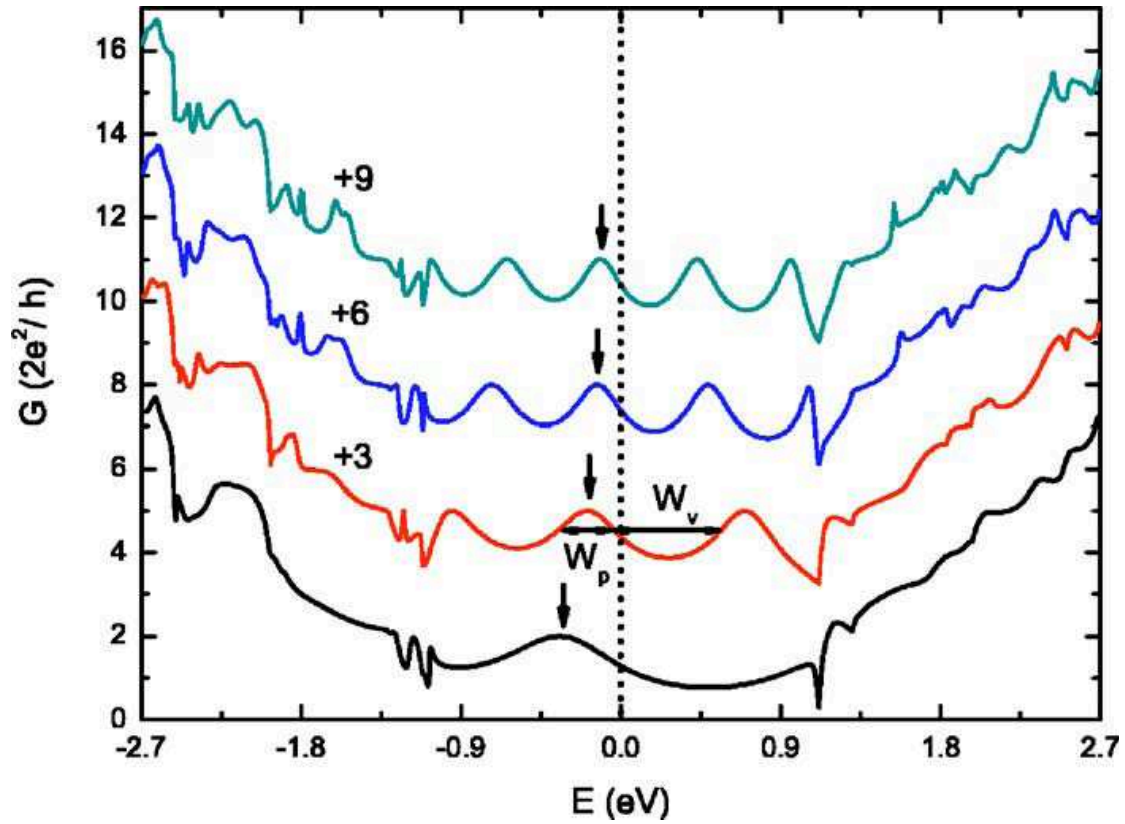


Fig.B.3.4 Conductance spectra for (12,0)/(9,0)/(12,0) with different lengths of (9,0), from bottom to top, corresponding to 1, 3, 5, and 6 unit cells of (9,0) respectively.¹⁹⁰

Further, we raised an exponentially dropped potential (Fig.B.3.5) to describe the potential distribution in the vicinity of interface (12,0)/(9,0).

$$V(x) = V_0 + V_1[e^{-\alpha(x+L/2)} + e^{\alpha(x-L/2)}] = V_0 + V_1e^{-\alpha L/2}(e^{-\alpha x} + e^{\alpha x}) \quad (\text{B.3.3})$$

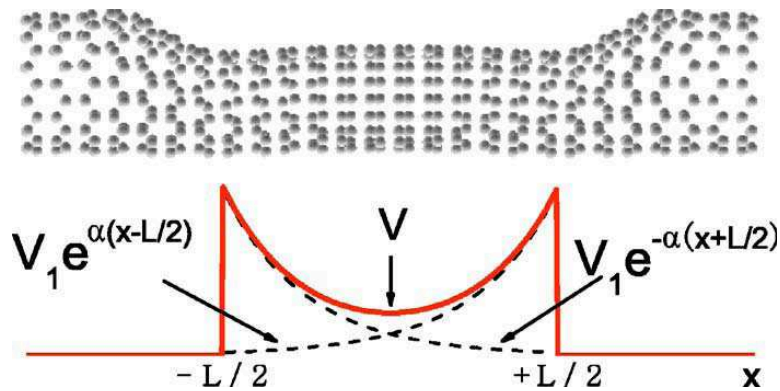


Fig.B.3.5 Schematic diagram of the exponentially dropped potential in Eq.B.3.3.

Where V_0 , V_1 , α are parameters to be determined and $|x| \leq L/2$. A schematic plot of the potential is shown in Fig.B.3.5. When $|\alpha x|$ is small, we can expand the exponential to the second order

$$V(x) \approx V_0 + V_1 e^{-\alpha L/2} (2 + \alpha^2 x^2) = V_0 + 2V_1 e^{-\alpha L/2} + \frac{1}{2} m \omega^2 x^2 \quad (\text{B.3.4})$$

$$\omega \equiv \sqrt{\frac{2V_1}{m}} \alpha e^{-\alpha L/4}$$

Eq.B.3.4 is a harmonic potential, and the energy interval between its neighbor eigenenergies is

$$\Delta E = \hbar \omega = \hbar \sqrt{\frac{2V_1}{m}} \alpha e^{-\alpha L/4} \quad (\text{B.3.5})$$

The energy interval decreases exponentially with L . It is in good agreement with the exponential decrease of resonant energy peak spacing shown in Fig.B.3.6. We can fit the peak spacing with Eq.B.3.5. Fitted values are $V_1 = 4.30\text{eV}$ and $\alpha = 0.1786\text{\AA}^{-1}$.

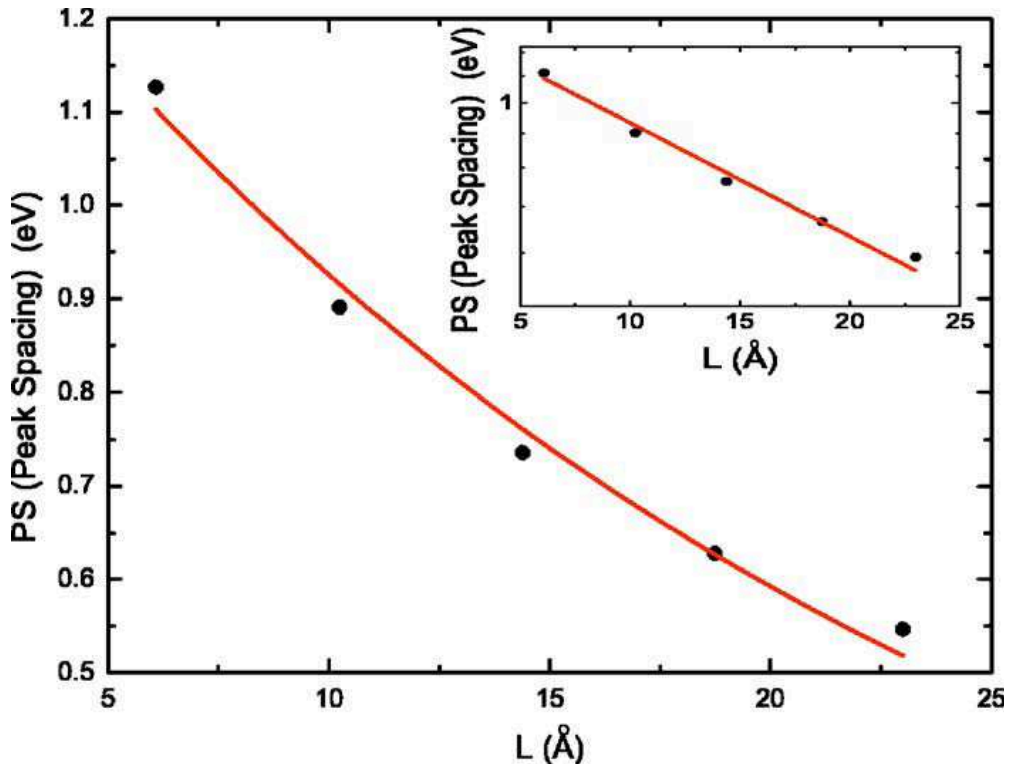


Fig.B.3.6 Relation between the peak spacing of resonant transmission and the length of conductor in (12,0)/(9,0)/(12,0) junction. Inset is semi-log plot.¹⁹⁰

§B.4 Ballistic transport of metallic CNT junctions

For a metallic CNT junction like $(n_1, m_1)/(n_2, m_2)/(n_1, m_1)$, if the center segment is of high symmetry, the geometry of junction can be changed by rotating one side with respect to the other side, and the rotation angle is determined by the symmetry of the center segment.

$$\theta = n \cdot \frac{2\pi}{d_2} \quad (\text{B.4.1})$$

$$d_2 \equiv \text{gcd}(n_2, m_2)$$

Fig.B.4.1 is an illustration of such metallic junction with $(n_1, m_1) = (6, 6)$, $(n_2, m_2) = (12, 0)$ and vice versa.

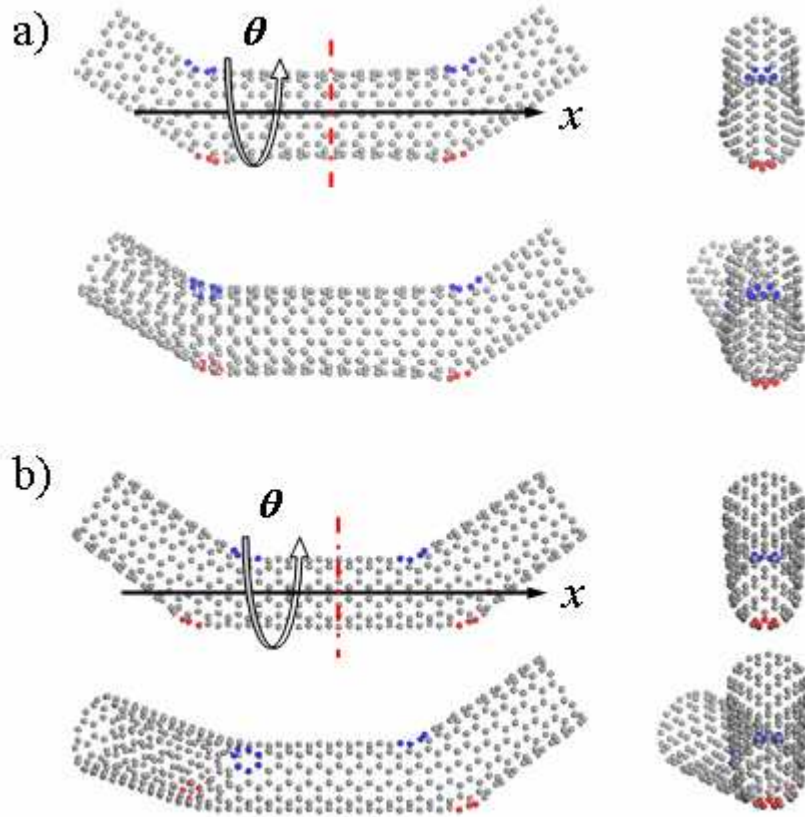


Fig.B.4.1 a) Geometries of $(6,6)/(12,0)/(6,6)$ junction for $\theta = 0^\circ$ and $\theta = 30^\circ$, b) geometries of $(12,0)/(6,6)/(12,0)$ junction for $\theta = 0^\circ$ and $\theta = 60^\circ$. From Ref.²¹⁰.

Fig.B.4.2 plot the conductance spectra for various configurations of (6,6)/(12,0)/(6,6) and (12,0)/(6,6)/(12,0) separately. In the vicinity of the Fermi level (0eV), there are two shapes of the conductance spectra for all configurations of (6,6)/(12,0)/(6,6), and a period of 90° exists. However, the conductance spectra for all configurations of (12,0)/(6,6)/(12,0) are the same. We studied many kinds of junctions and found the phenomenon is quite common.

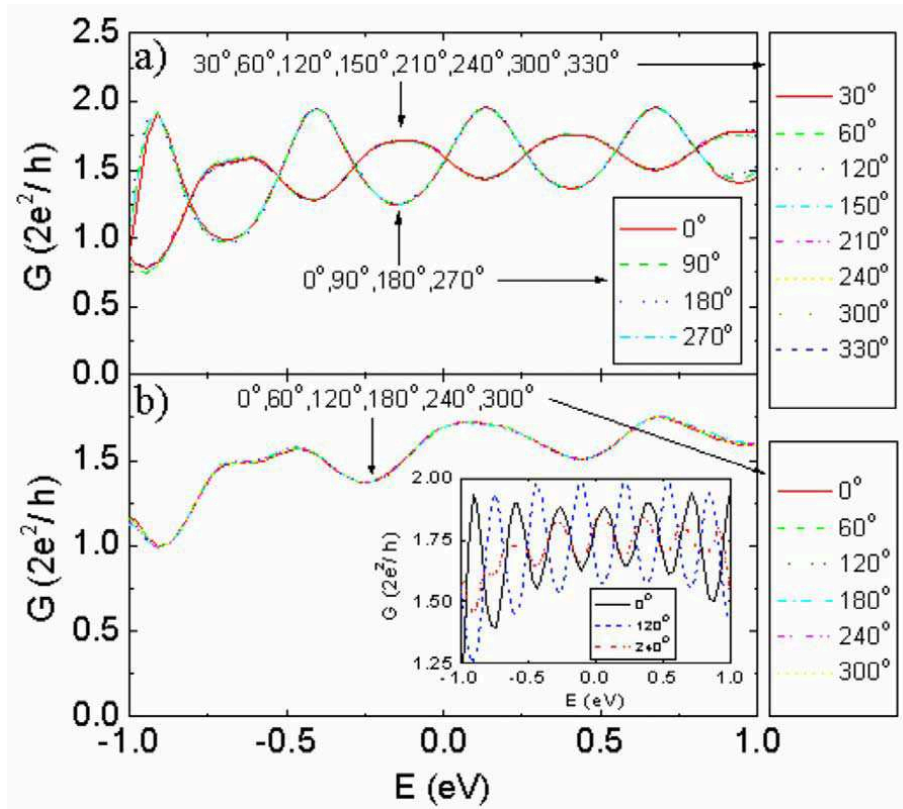


Fig.B.4.2 a) Conductance spectra for (6,6)/(12,0)/(6,6) with $\theta = 0^\circ, 30^\circ, \dots, 330^\circ$. b) Conductance spectra for (12,0)/(6,6)/(12,0) with $\theta = 0^\circ, 60^\circ, \dots, 300^\circ$. From Ref.²¹⁰.

From now on, we move on to investigate the general physics behind this phenomenon. We consider a general case that an electron passes through a carbon nanotube from site A to site B as illustrated in Fig.B.4.3. The phase difference of electron traveling from A to B is the only factor that may affect the transmission coefficient because there is no collision in ballistic transport. Then we write down the phase difference as

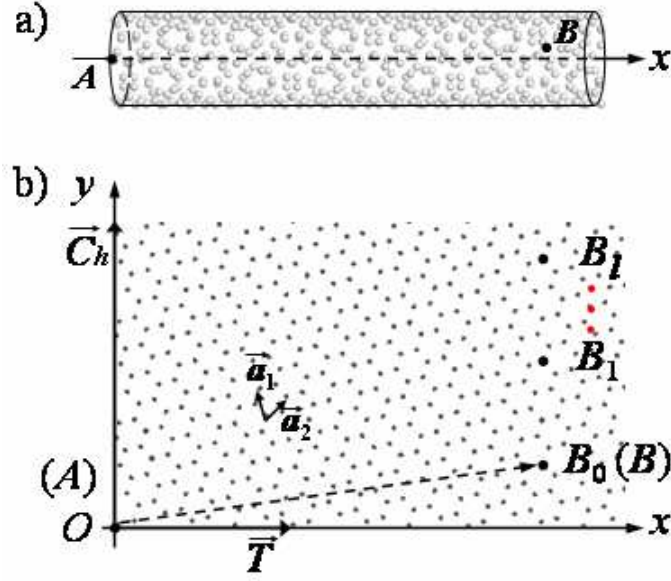


Fig.B.4.3 a) Schematic diagram of a CNT with two defects A and B . b) Planar graph of a), $\vec{C}_h=(n,m)$ and \vec{T} are the chiral vector and the translational vector of the nanotube respectively, \vec{a}_1 and \vec{a}_2 are primitive vectors, all the points of B_l ($l = 0,2,\dots,d-1$, $d = \text{gcd}(n,m)$) are equivalent due to the symmetry of the tube.²¹⁰

$$\varphi_{AB_l}(k_x, k_y) = k_x(x_{B_l} - x_A) + k_y(y_{B_l} - y_A) \quad (\text{B.4.2})$$

Substitute $\Delta x_{AB} \equiv x_{B_0} - x_A = x_{B_1} - x_A = \dots = x_{B_l} - x_A$, $\Delta y_{AB} \equiv y_{B_0} - y_A$, and $y_{B_l} - y_A = \Delta y_{AB} + l \cdot |\vec{C}_h| / d$ into Eq.B.4.2, then

$$\varphi_{AB_l}(k_x, k_y) = k_x \Delta x_{AB} + k_y \Delta y_{AB} + k_y \cdot l \cdot \frac{|\vec{C}_h|}{d} \quad (\text{B.4.3})$$

$$l = 0, \dots, d-1$$

From band-folding theory, the Fermi level lies on two irreducible points K_1 and K_2 in the reciprocal space of Bravais lattice as shown in Fig.B.4.4. The transverse component of wavevector is

$$k_y = \vec{\Gamma K} \cdot \vec{C}_h / |\vec{C}_h| = \pm 2\pi \cdot \frac{n-m}{3|\vec{C}_h|} \quad (\text{B.4.4})$$

substitute Eq.B.4.4 into Eq.B.4.3, then

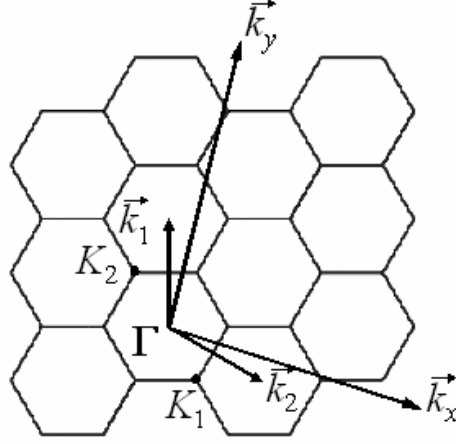


Fig.B.4.4 Reciprocal space of graphene, the irreducible points K_1 and K_2 are corresponding to the Fermi level in electronic structure.²¹⁰

$$\varphi_{AB_l}(k_x, K) = k_x \Delta x_{AB} + k_y \Delta y_{AB} \pm 2\pi \cdot \frac{l \cdot (n - m)}{3d} \quad (\text{B.4.5})$$

$$l = 0, \dots, d - 1$$

Based on Eq.B.4.5, a universal relation for any metallic CNT junction like $(n_1, m_1)/(n_2, m_2)/(n_1, m_1)$ is predicted:

1) When $(n_2 - m_2)/3d$ is an integer, φ changes integer times of 2π with different l 's, and then no change in the ballistic transport behavior of electrons. Consequently, all conductance spectra are the same for various configurations.

2) When $(n_2 - m_2)/3d$ is not an integer, φ changes periodically in period of three with increasing l . There are two situations now. First, if the first two terms of the right hand side in Eq.B.4.5 are integral multiple of $\pi/3$, two thirds of the configurations are corresponding to the first conductance spectrum, and the other one third are corresponding to the second conductance spectrum. Second, if the first two terms of the right hand side in Eq.B.4.5 are not integral multiple of $\pi/3$, there will be three different conductance spectra (e.g. $(12,0)/(9,3)/(12,0)$, shown in Fig.B.4.5).

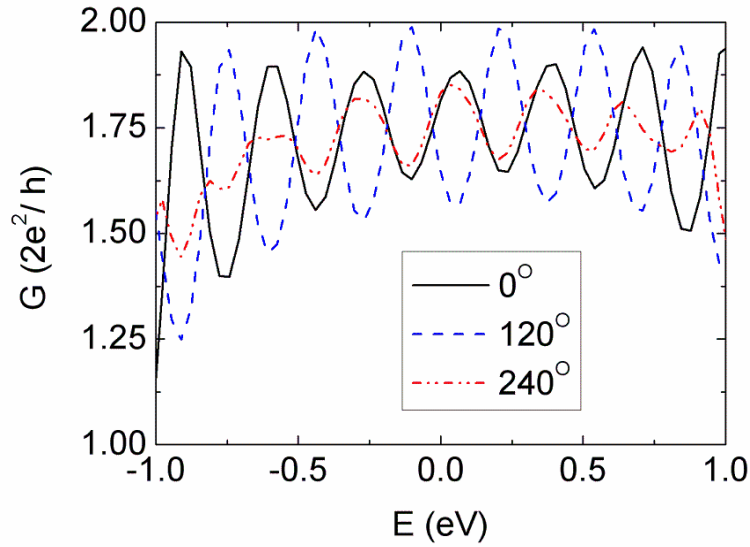


Fig.B.4.5 Conductance spectra for (12,0)/(9,3)/(12,0) with $\theta = 0^\circ$, 120° , and 240° .

§B.5 Ballistic transport of T junction and Cross junction

Fig.B.5.1 is an illustration of the atomic structure of T junction (6,6)/(6,0)/(6,6). We marked the three ends with numbers. Ballistic conductance spectra between any two ends are calculated and shown in Fig.B.5.2. The two conductance spectra between (6,0) tube and different (6,6) tube are the same.

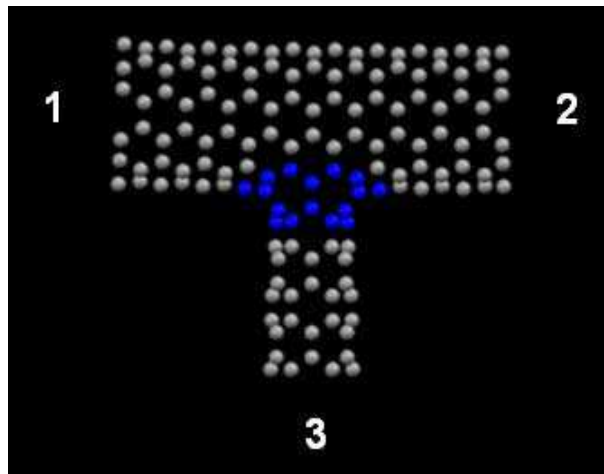


Fig.B.5.1 Atomic structure of T junction (6,6)/(6,0)/(6,6). Numbers ‘1’, ‘2’ and ‘3’ denote the three leads if the junction is regarded as an electronic device.

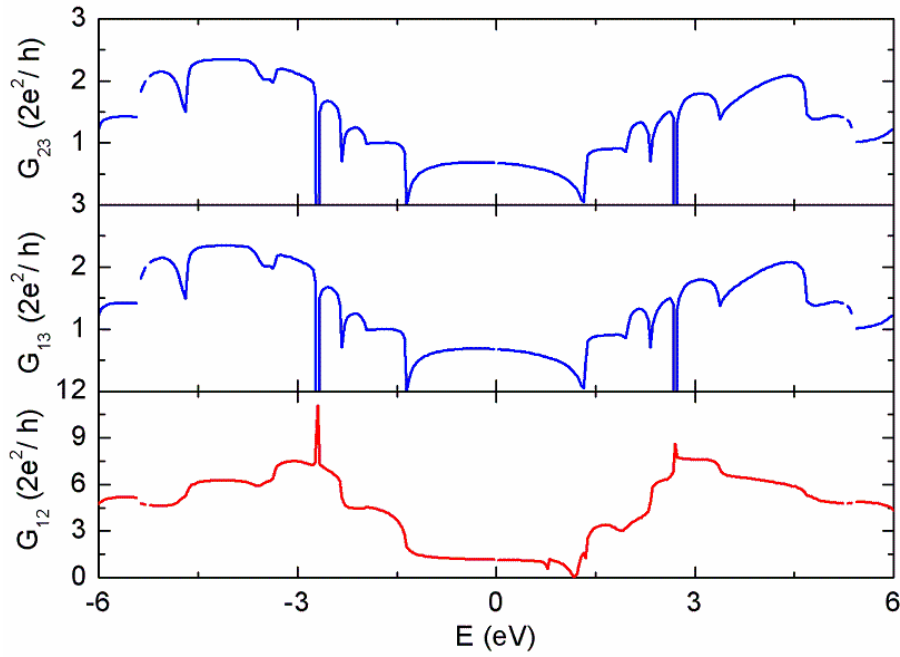


Fig.B.5.2 Conductance spectra between different leads of T junction (6,6)/(6,0)/(6,6).

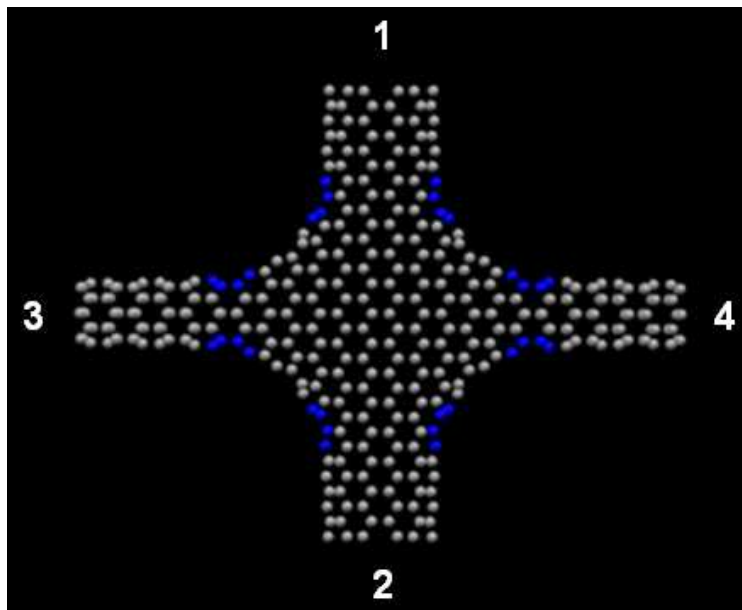


Fig.B.5.3 Atomic structure of Cross junction (6,6)/(6,0)/(6,6)/(6,0).

Fig.B.5.3 shows the structure of Cross junction (6,6)/(6,0)/(6,6)/(6,0) and Fig.B.5.4 plots the ballistic conductance spectra between different leads. The conductance between two (6,6) leads is nearly zero in the vicinity of Fermi level. The conductance between one (6,6) lead and one (6,0) lead is a small finite value around Fermi level. The conductance between two (6,0) leads is very big and resonant tunneling appears.

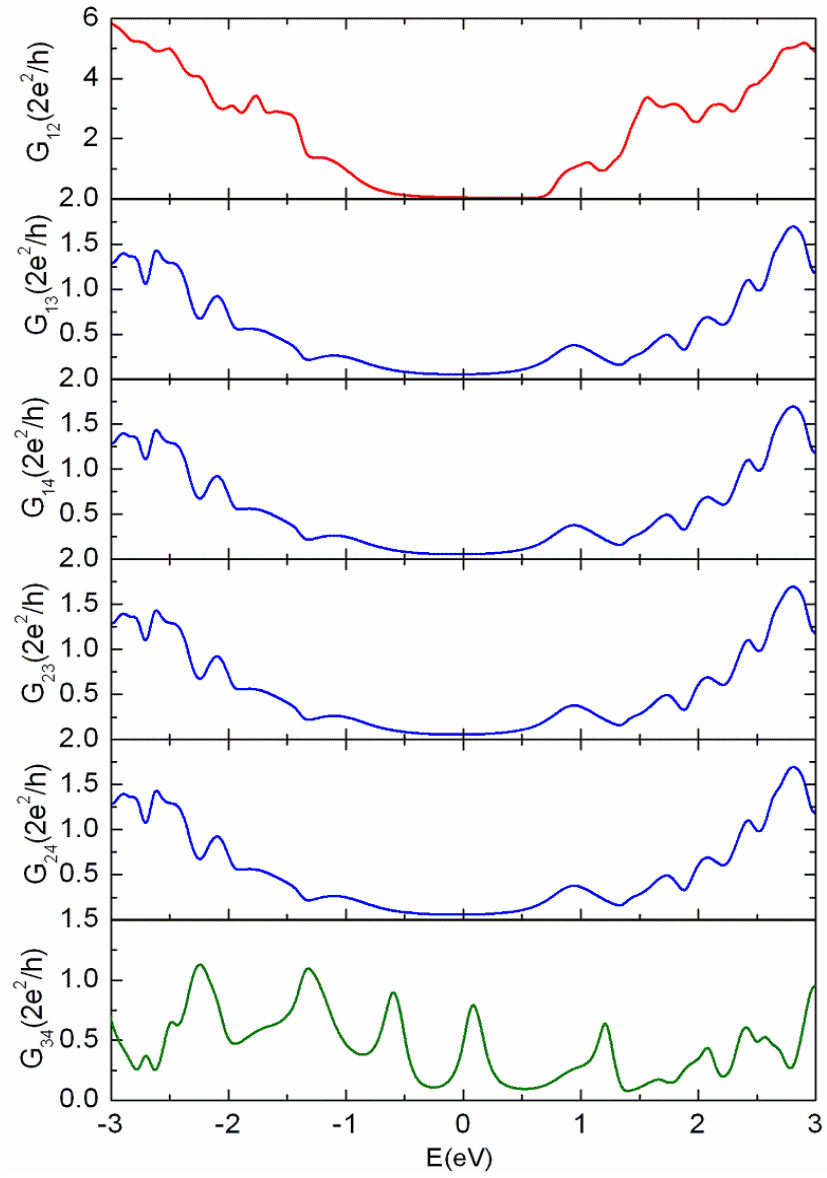


Fig.B.5.4 Conductance spectra between different leads of Cross junction

(6,6)/(6,0)/(6,6)/(6,0).

References

1. *Cramming more components onto integrated circuits*, Gordon E. Moore, *Electronics* **38**, 8 (1965).
2. *Excerpts from A Conversation with Gordon Moore: Moore's Law*, Intel Corporation 2005.
3. *1965—"Moore's Law" Predicts the Future of Integrated Circuits*, Computer History Museum, 2007.
4. *Progress in Digital Integrated Electronics*, Gordon E. Moore, IEEE, IEDM Tech Digest 11-13 (1975).
5. *Report on Penryn Series Improvements*, Intel (October 2006).
6. *Revolutionizing How We Use Technology—Today and Beyond*, Intel (July 2008).
7. *Logic Operations at the Molecular Level: An XOR Gate Based on a Molecular Machine*, A. Credi, V. Balzani, S. J. Langford, and J. F. Stoddart, *J. Am. Chem. Soc.* **119**, 2679 (1997).
8. *Understanding Nanotechnology*, by Scientific American, Grand Central Publishing (2002).
9. *Functional Nanoscale Electronic Devices Assembled Using Silicon Nanowire Building Blocks*, Y. Cui and C. M. Lieber, *Science* **291**, 851 (2001).
10. *Physical properties of carbon nanotubes*, R. Saito, G. Dresselhaus and M. S. Dresselhaus, Imperial College Press (1998).
11. *Diameter-controlled synthesis of single-crystal silicon nanowires*, Y. Cui et al., *Appl. Phys. Lett.* **78**, 2214 (2001).
12. *The influence of the surface migration of gold on the growth of silicon nanowires*, J. B. Hannon et al., *Nature* **440**, 69 (2006).

13. *Control of Thickness and Orientation of Solution-Grown Silicon Nanowires*, J. D. Holmes et al., Science **287**, 1471 (2000).
14. *Synthesis of large area silicon nanowire arrays via self-assembling nano electrochemistry*, Adv. Mat. **14**, 1164 (2002).
15. *Silicon vertically integrated nanowire field effect transistors*, J. Goldberger et al., Nano Lett. **6**, 973 (2006).
16. *Self-Oriented Regular Arrays of Carbon Nanotubes and Their Field Emission Properties*, S. Fan et al., Science **283**, 512 (1999).
17. *Synthesis of Large Arrays of Well-Aligned Carbon Nanotubes on Glass*, Z. F. Ren et al., Science **282**, 1105 (1998).
18. *Large-Scale Synthesis of Aligned Carbon Nanotubes*, W. Z. Li et al., Science **274**, 1701 (1996).
19. *Single- and multi-wall carbon nanotube field-effect transistors*, R. Martel et al., Appl. Phys. Lett. **73**, 2447 (1998).
20. *Scanned Probe Microscopy of Electronic Transport in Carbon Nanotubes*, A. Bachtold et al., arXiv:cond-mat/0002209 (2000).
21. *Michael Faraday: Physics and Faith*, C. Russell, Oxford University Press (2000).
22. *The Kind of Motion We Call Heat: A History of the Kinetic Theory of Gases*, S. G. Brush, Amsterdam: North-Holland (1986).
23. *The Quantum Theory of the Electron*, P. A. M. Dirac, in Proceedings of the Royal Society of London (1928-02-01).
24. *Nuclear Physics*, E. Fermi, University of Chicago Press (1950).
25. *Spatial variation of currents and fields due to localized scatterers in metallic conduction*, R. Landauer, IBM J. RES. DEVELOP. **44**, 251 (2000).
26. *Statistical Physics I: Equilibrium Statistical Mechanics (Springer Series in Solid-State Sciences)*, M. Toda et al., 3rd Edition, Springer (2004).
27. *Quantum transport theory of electrons in solids: A single-particle approach*, J. Rammer, Rev. Mod. Phys. **63**, 781 (1991).
28. *Growth of silicon nanowires via gold/silane vapor–liquid–solid reaction*, J. Westwater et al., Journal of Vacuum Science & Technology B: Microelectronics

- and Nanometer Structures **15**, 554 (1997).
29. *Vapor-liquid-solid mechanism of single crystal growth*, R. S. Wagner and W. C. Ellis, Appl. Phys. Lett. **4**, 89 (1964).
 30. *Electron beam lithography patterning of sub-10 nm line using hydrogen silsesquioxane for nanoscale device applications*, I-B. Baek et al., J. Vac. Sci. Technol. B **23**, 3120 (2005).
 31. *Sub-10 nm Nanoimprint Lithography by Wafer Bowing*, W. Wu et al., Nano Lett. **8**, 3865 (2008).
 32. *Physics of Semiconductor Devices*, S. M. Sze and K. K. Ng, John Wiley & Sons Inc. (2007).
 33. *Small-Diameter Silicon Nanowire Surface*, D. Ma et al., Science **299**, 5614 (2003).
 34. *First-Principles calculations of the electronic properties of silicon quantum wires*, A. Read et al., Phys. Rev. Lett. **69**, 8 (1992).
 35. *Size dependence of band gaps in silicon nanostructures*, B. Delley and E. Steigmeier, Appl. Phys. Lett. **67**, 2370 (1995).
 36. *Measurement on Carrier Mobility in Silicon Nanowires*, O. Gunawan et al., Nano Lett. **8**, 1566 (2008).
 37. *Quantum Confinement and Electronic Properties of Silicon Nanowires*, X. Zhao et al., Phys. Rev. Lett. **92**, 236805 (2004).
 38. *Phonon modes in Si [111] nanowires*, T. Thonhauser and G. D. Mahan, Phys. Rev. B **69**, 075213 (2004).
 39. *Theory of transport in silicon quantum wires*, G. D. Sanders, C. J. Stanton, and Y. C. Chang, Phys. Rev. B **48**, 11067 (1993).
 40. *Electron Mobility in Silicon Nanowires*, E. B. Ramayya et al., IEEE Transactions on nanotechnology **6**, 113 (2007).
 41. *Significant Enhancement of Hole Mobility in [110] Silicon Nanowires Compared to Electrons and Bulk Silicon*, A. K. Bui et al., Nano Lett. **8**, 760 (2008).
 42. *Size Dependence of Surface-Roughness-Limited Mobility in Silicon-Nanowire FETs*, S. Poli et al., IEEE Transactions on electron devices **55**, 2968 (2008).

43. *A Laser Ablation Method for the Synthesis of Crystalline Semiconductor Nanowires*, A. M. Morales and C. M. Lieber, *Science* **279**, 208 (1998).
44. *Electronic and transport properties of silicon nanowires*, F. Sacconi et al., *J. Comput. Electron* **6**, 329 (2007).
45. *Electronic structure of semiconductor nanowires*, Y. M. Niquet et al., *Phys. Rev. B* **73**, 165319 (2006).
46. *Simplified LCAO Method for the Periodic Potential Problem*, J. C. Slater and G. F. Koster, *Phys. Rev.* **94**, 1498 (1954).
47. *Nanostructures: Theory and Modelling*, C. Delerue and M. Lannoo, Springer (March 31, 2004).
48. *Empirical $sp^3d^5s^*$ tight-binding calculation for cubic semiconductors: General method and material parameters*, J-M. Jancu et al., *Phys. Rev. B* **57**, 6493 (1998).
49. *Introduction to Lattice Dynamics*, M. T. Dove, Cambridge Topics in Mineral Physics and Chemistry, University of Cambridge Press (1993).
50. *Effect of Invariance Requirements on the Elastic Strain Energy of Crystals with Application to the Diamond Structure*, P. N. Keating, *Phys. Rev.* **145**, 637 (1966).
51. *Theory of the Third-Order Elastic Constants of Diamond-Like Crystals*, P. N. Keating, *Phys. Rev.* **149**, 674 (1966).
52. *Anharmonic elastic and phonon properties of Si*, D. Vanderbilt, S. H. Taole and S. Narasimhan, *Phys. Rev. B* **40**, 5657 (1989).
53. *Monte Carlo Methods in Ab Initio Quantum Chemistry*, B. J. Hammond, W. A. Lester and P. J. Reynolds, Singapore: World Scientific (1994).
54. *Quantum Chemistry*, I. N. Levine, New jersey: Prentice Hall (1991).
55. *A tight-binding method for the evaluation of the total energy of large systems*, M. J. Mehl, D. A. Papaconstantopoulos and R. E. Cohen, *International Journal of Thermophysics* **16**, 503 (1995).
56. *Introduction to Solid State Physics*, C. Kittel, Wiley: New York (1996).
57. *On the Non-Orthogonality Problem Connected with the Use of Atomic Wave Functions in the Theory of Molecules and Crystals*, Per-Olov Löwdin, *J. Chem. Phys.* **18**, 365 (1950).

58. *Tight-Binding Approach to Computational Materials Science*, P. E. A. Turchi, A. Gonis, and L. Columbo, eds., MRS Proceedings **491**, 221 (Materials Research Society, Warrendale PA, 1998).
59. *Nonorthogonal tight-binding model for germanium*, N. Bernstein, M. J. Mehl, and D. A. Papaconstantopoulos, Phys. Rev. B **66**, 075212 (2002).
60. *Applications of a tight-binding total-energy method for transition and noble metals: Elastic constants, vacancies, and surfaces of monatomic metals*, M. J. Mehl and D. A. Papaconstantopoulos, Phys. Rev. B **54**, 4519 (1996).
61. Private communications with Dr. Y. M. Niquet (CEA/CNRS, Grenoble).
62. *First-principles computation of material properties : the ABINIT software project*, X. Gonze et al., Computational Materials Science **25**, 478-492 (2002).
63. *Solid state theory*, Z. Z. Li, 2nd Ed., Advanced Education Press (December, 2002).
64. *Dynamical Theory of Crystal Lattices*, M. Born and K. Huang, Oxford University Press: Oxford (1954).
65. *Phonons and related crystal properties from density-functional perturbation theory*, S. Baroni et al., Rev. Mod. Phys. **73**, 515 (2001).
66. *Practical methods in ab initio lattice dynamics*, G. J. Ackland, M. C. Warren, and S. J. Clark, J. Phys.: Condens. Matter **9**, 7861 (1997).
67. Private communications with Dr. C. Delerue (IEMN/CNRS, Lille).
68. *Valence band effective-mass expressions in the $sp^3d^5s^*$ empirical tight-binding model applied to a Si and Ge parametrization*, T. B. Boykin, G. Klimeck and F. Oyafuso, Phys. Rev. B **69**, 115201 (2004).
69. http://en.wikipedia.org/wiki/Gaussian_function
70. Private communications with Dr. G. Allan (IEMN/CNRS, Lille).
71. *Fundamentals of carrier transport*, M. Lundstrom, 2nd Ed., Cambridge University Press (2000).
72. *Electron-Phonon Interaction and Transport in Semiconducting Carbon Nanotubes*, V. Perebeinos, J. Tersoff and Phaedon Avouris, Phys. Rev. Lett. **94**, 086802 (2005).
73. *Introduction to algorithms* (2nd ed.), T. H. Cormen, C. E. Leiserson, R. L. Rivest

- and C. Stein, MIT press and McGraw-Hill, 2001.
74. *Methods of conjugate gradients for solving linear systems*, M. R. Hestenes and E. Stiefel, Journal of Research of the National Bureau of Standards **49**, 409(1952).
 75. *Matrix analysis*, R. A. Horn and C. R. Johnson, Cambridge University Press, 1985.
 76. *An introduction to numerical analysis* (2nd ed.), A. A. Kendell, John Wiley and Sons, 1988.
 77. *Nonlinear programming: analysis and methods*, A. Mordecai, Dover Publishing, 2003.
 78. *Matrix computations* (3rd ed.), H. G. Gene and C. F. Van Loan, Johns Hopkins University Press, 1996.
 79. *Iterative methods for sparse linear systems* (2nd ed.), Y. Saad, Society of Industrial and Applied Mathematics, 2003.
 80. *An introduction to the conjugate gradient method without the agonizing pain* (Edition $1\frac{1}{4}$), J. R. Shewchuk, Carnegie Mellon University, 1994.
 81. *Numerical Recipes in Fortran 90*, W. H. Press et al., 2nd Ed., Cambridge University Press (January 15, 1996).
 82. http://en.wikipedia.org/wiki/Conjugate_gradient_method
 83. http://en.wikipedia.org/wiki/Preconditioned_conjugate_gradient_method
 84. *First-principles calculations of the electronic properties of silicon quantum wires*, A. J. Read et al., Phys. Rev. Lett. **69**, 1232 (1992).
 85. *Optical properties of porous silicon: a first-principles study*, F. Buda, J. Kohanoff, and M. Parrinello, Phys. Rev. Lett. **69**, 1272 (1992).
 86. *Size dependence of band gaps in silicon nanostructures*, B. Delley and E. F. Steigmeier, Appl. Phys. Lett. **67**, 2370 (1995).
 87. *Metallic and semimetallic silicon [100] nanowires*, R. Rurali and N. Lorente, Phys. Rev. Lett. **94**, 026805 (2005).
 88. *Structural and electronic properties of epitaxial core-shell nanowire hetero structures*, R. N. Musin and X. Q. Wang, Phys. Rev. B **71**, 155318(R) (2005).

89. *Interband absorption in quantum wires. I. Zero-magnetic-field case*, U. Bockelmann and G. Bastard, Phys. Rev. B **45**, 1688 (1992).
90. *Confinement, surface, and chemisorption effects on the optical properties of Si quantum wires*, C. Y. Yeh, S. B. Zhang and A. Zunger, Phys. Rev. B **50**, 14405 (1994).
91. *Quantum Confinement and Electronic Properties of Silicon Nanowires*, X. Y. Zhao, C. M. Wei, L. Yang and M. Y. Chou, Phys. Rev. Lett. **92**, 236805 (2004).
92. *Theory of optical properties of quantum wires in porous silicon*, G. D. Sanders and Y. C. Chang, Phys. Rev. B **45**, 9202 (1992).
93. *Theoretical aspects of the luminescence of porous silicon*, C. Delerue, G. Allan, and M. Lannoo, Phys. Rev. B **48**, 11024 (1993).
94. *Quantum confinement effect in thin quantum wires*, J. B. Xia and K. W. Cheah, Phys. Rev. B **55**, 15688 (1997).
95. *Electronic structure of semiconductor nanowires*, Y. M. Niquet, A. Lherbier, N. H. Quang, M. V. Fernández-Serra, X. Blase and C. Delerue, Phys. Rev. B **73**, 165319 (2006).
96. *Quantum Confinement and Electronic Properties of Tapered Silicon Nanowires*, Z. G. Wu, J. B. Neaton and J. C. Grossman, Phys. Rev. Lett. **100**, 246804 (2008).
97. *Size and orientation dependence in the electronic properties of silicon nanowires*, J. A. Yan, L. Yang and M. Y. Chou, Phys. Rev. B **76**, 115319 (2007).
98. L. Hedin and S. Lundqvist, in *Solid State Physics* **23**, edited by F. Seitz, D. Turnbull and H. Ehrenreich (Academic, New York, 1969).
99. W. G. Aulbur, L. Jonsson and J. W. Wilkins, in *Solid State Physics* **54**, edited by H. Ehrenreich and F. Spaepen (Academic, New York, 2000).
100. [http://en.wikipedia.org/wiki/Effective_mass_\(solid-state_physics\)](http://en.wikipedia.org/wiki/Effective_mass_(solid-state_physics))
101. *Structural interpretation of the vibrational spectra of a-Si: H alloys*, G. Lucovsky, R. J. Nemanich and J. C. Knights, Phys. Rev. B **19**, 2064 (1979).
102. *Phonon Band Structure of Si Nanowires: a stability analysis*, H. Peelaers, B. Partoens and F. M. Peeters, Nano. Lett. **9**, 107 (2009).
103. *Lattice dynamics of silicon nanostructures*, S. P. Hepplestone and G. P. Srivastava,

- Nanotechnology **17**, 3288 (2006).
104. *High performance silicon nanowire field effect transistors*, Y. Cui, et al., Nano Lett. **3**, 149 (2003).
105. *In situ axially doped n-channel silicon nanowire field-effect transistors*, T. Ho, et al., Nano Lett. **8**, 4359 (2008).
106. *Measurement of carrier mobility in silicon nanowires*, O. Gunawan, et al., Nano Lett. **8**, 1566 (2008).
107. *Acoustic-phonon scattering in a rectangular quantum wire*, R. Mickevicius and V. Mitin, Phys. Rev. B **48**, 17194 (1993).
108. *The monte carlo method for the solution of charge transport in semiconductors with applications to covalent materials*, C. Jacoboni and L. Reggiani, Rev. Mod. Phys. **55**, 645 (1983).
109. *Quantum Theory of Solids* (2nd ed.), C. Kittel, John Wiley & Sons, 1987.
110. *Scattering of Electrons by Lattice Vibrations in Nonpolar Crystals*, W. A. Harrison, Phys. Rev. **104**, 1281 (1956).
111. *Deformation potential for semiconductors with complex bands*, G. L. Bir and G. E. Pikus, Fiz. Tverd. Tela **2**, 2287 (1961).
112. *Electrons and Phonons*, J. M. Ziman, Oxford University (1960).
113. *Symmetry and Strain-Induced Effects in Semiconductors*, G. L. Bir and G. E. Pikus, Wiley (1974).
114. *Long-Wavelength Phonon Scattering in Nonpolar Semiconductors*, P. Lawaetz, Phys. Rev. **183**, 730 (1969).
115. *Microscopic theory of electron-phonon interaction in insulators or semiconductors*, P. Vogl, Phys. Rev. B **13**, 694 (1976).
116. *Theory of optical-phonon deformation potentials in tetrahedral semiconductors*, W. Pötz and P. Vogl, Phys. Rev. B **24**, 2025 (1981).
117. *Self-consistent calculation of electron-phonon couplings*, P. K. Lam, M. M. Dacorogna and M. L. Cohen, Phys. Rev. B **34**, 5065 (1986).
118. *Theoretical investigation of electron-phonon interaction in one-dimensional silicon quantum dot array interconnected with silicon oxide layers*, S. Uno et al.,

- Phys. Rev. B **72**, 035337 (2005).
119. *Transport in Nanostructures*, D. K. Ferry and S. M. Goodnick, Cambridge University Press (1997).
120. *Fundamentals of Carrier Transport*, M. Lundstrom, Cambridge University Press (2000).
121. *High Field Transport in Semiconductors*, E. M. Conwell, Academic, Solid State Phys. Suppl. **9** (1967).
122. *Direct solution of the Boltzmann transport equation in nanoscale Si devices*, K. Banoo, PhD thesis, Purdue University (2000).
123. *Electron mobility in silicon nanowires*, E. B. Ramayya et al., IEEE Trans. Nanotechnology **6**, 113 (2007).
124. *Scattering Probabilities for Holes I. Deformation Potential and Ionized Impurity Scattering Mechanisms*, M. Costato and L. Reggiani, physica status solidi (b) **58**, 471 (1973).
125. *Acoustic scattering in a two-band system and its application to hole transport properties in cubic semiconductors*, S. Bosi, C. Jacoboni and L. Reggiani, J. Phys. C: Solid State Phys. **12**, 1525 (1979).
126. *Intervalley scattering selection rules for silicon and germanium*, H. W. Streitwolf, physica status solidi (b) **37**, K47 (1970).
127. *Electron-phonon interaction in n-silicon*, M. Asche, O. G. Sarbei, physica status solidi (b) **103**, 11 (1981).
128. *Theory of Impurity Scattering in Semiconductors*, E. Conwell and V. F. Weisskopf, Phys. Rev. **77**, 388 (1950).
129. *Electron scattering by ionized impurities in semiconductors*, D. Chattopadhyay and H. J. Queisser, Rev. Mod. Phys. **53**, 745 (1981).
130. *Scattering of electrons and holes by charged donors and acceptors in semiconductors*, Philosophical Magazine **46**, 831 (1955).
131. *Electron Transport in Compound Semiconductors*, B. R. Nag, Springer-Verlag Berlin and Heidelberg GmbH & Co. K (1980).
132. *Scattering of carriers by ionized impurities in semiconductors*, F. J. Blatt, J. Phys.

- and Chem. Solids **1**, 262 (1957).
133. *Heavily doped semiconductors and devices*, R. A. Abram, G. J. Rees and B. L. H. Wilson, *Advances in Physics* **27**, 799 (1978).
134. *Deformation electron-phonon coupling in disordered semiconductors and nanostructures*, A. Sergeev, M. Y. Reizer and V. Mitin, *Phys. Rev. Lett.* **94**, 136602 (2005).
135. *Charged impurity scattering limited low temperature resistivity of low density silicon inversion layers*, S. D. Sarma and E. H. Hwang, *Phys. Rev. Lett.* **83**, 164 (1999).
136. *Comment on “charged impurity scattering limited low temperature resistivity of low density silicon inversion layers”*, A. Gold and V. T. Dolgoplov, *Phys. Rev. Lett.* **85**, 3541 (2000).
137. *Theory of screening and electron mobility: application to n-type silicon*, B. A. Sanborn, P. B. Allen and G. D. Mahan, *Phys. Rev. B* **46**, 15123 (1992).
138. *Effect of the electron-plasmon interaction on the electron mobility in silicon*, M. V. Fischetti, *Phys. Rev. B* **44**, 5527 (1991).
139. *Transport along doping quantum wires in silicon*, G. E. Bauer, *Phys. Rev. B* **43**, 4023 (1991).
140. *Elastic scattering of electrons by neutral donor impurities in silicon*, K. C. Kwong, J. Callaway, N. Y. Du and R. A. LaViolette, *Phys. Rev. B* **43**, 1576 (1991).
141. *Inelastic scattering of electrons by neutral impurities in semiconductors*, K. C. Kwong, N. Y. Du, J. Callaway and R. A. LaViolette, *Phys. Rev. B* **41**, 12666 (1990).
142. *Electronic structure and impurity limited electron mobility of silicon superlattices*, S. Krishnamurthy and J. A. Moriarty, *Phys. Rev. B* **32**, 1027 (1985).
143. *Effect of valence dielectric screening on ionized-impurity scattering in semiconductors*, D. Chandramohan and S. Balasubramanian, *Phys. Rev. B* **31**, 3899 (1985).
144. *Monte carlo simulation of remote coulomb scattering limited mobility in metal*

- oxide semiconductor transistors*, F. Gámiz, J. B. Roldán, J. E. Carceller, and P. Cartujo, *Appl. Phys. Lett.* **82**, 3251 (2003).
145. *Remote coulomb scattering in metal oxide semiconductor field effect transistors: screening by electrons in the gate*, F. Gámiz and M. V. Fischetti, *Appl. Phys. Lett.* **83**, 4848 (2003).
146. *Modeling transport in ultrathin Si nanowires: charged versus neutral impurities*, R. Rurali et al., *Nano Lett.* **8**, 2825 (2008).
147. *Scattering suppression and high-mobility effect of size-quantized electrons in ultrafine semiconductor wire structures*, H. Sakaki, *Jpn. J. Appl. Phys.* **19**, L735 (1980).
148. *Scattering in quantum simulations of silicon nanowire transistors*, M. J. Gilbert, R. Akis and D. K. Ferry, *J. Phys.: Conf. Ser.* **35**, 219 (2006).
149. *The influence of polarisation and image charges on electron impurity scattering in high degeneracy nanometre scale silicon wrap-round gate MOSFETs*, J. R. Barker, E. Towie and J. R. Watling, *J. Phys.: Conf. Ser.* **109**, 012009 (2008).
150. *A theoretically accurate mobility model for semiconductor device drift-diffusion simulation*, E. Velmre, A. Udal, T. Kocsis and F. Masszi, *Phys. Scr.* **T54**, 263 (1994).
151. *Charged precipitate scattering of electrons in silicon*, L. Zhong, J. X. Shi and S. M. She, *Phys. Scr.* **37**, 800 (1988).
152. *Electron-phonon scattering in Li-doped silicon in the intermediate concentration region*, V. Radhakrishnan and P. C. Sharma, *J. Phys. C: Solid State Phys.* **13**, 2001 (1980).
153. *Effect of ionised impurity scattering on hot-electron diffusion in silicon*, D. Chattopadhyay and B. R. Nag, *J. Phys. C: Solid State Phys.* **11**, 2055 (1978).
154. *The Electrical Conductivity and Hall Effect of Silicon*, E. H. Putley and W. H. Mitchell, *Proc. Phys. Soc.* **72**, 193 (1958).
155. *Thermal conductivity of silicon in the boundary scattering regime*, W. S. Hurst and D. R. Frankl, *Phys. Rev.* **186**, 801 (1969).
156. *Warm and hot carriers in silicon surface -inversion layers*, K. Hess and C. T. Sah,

- Phys. Rev. B **10**, 3375 (1974).
157. *Hot-electron effects in silicon quantized inversion layers*, D. K. Ferry, Phys. Rev. B **14**, 5364 (1976).
158. *Intersubband scattering effect on the mobility of a Si (100) inversion layer at low temperatures*, S. Mori and T. Ando, Phys. Rev. B **19**, 6433 (1979).
159. *Calculated temperature dependence of mobility in silicon inversion layers*, F. Stern, Phys. Rev. Lett. **44**, 1469 (1980).
160. *Temperature dependent resistivities in silicon inversion layers at low temperatures*, K. M. Cham and R. G. Wheeler, Phys. Rev. Lett. **44**, 1472 (1980).
161. *Peak mobility of silicon metal-oxide-semiconductor systems*, A. Gold, Phys. Rev. Lett. **54**, 1079 (1985).
162. *Electronic transport properties of a two-dimensional electron gas in a silicon quantum-well structure at low temperature*, A. Gold, Phys. Rev. B **35**, 723 (1987).
163. *Phonon scattering at silicon crystal surfaces*, T. Klitsner and R. O. Pohl, Phys. Rev. B **36**, 6551 (1987).
164. *Monte Carlo study of electron transport in silicon inversion layers*, M. V. Fischetti and S. E. Laux, Phys. Rev. B **48**, 2244 (1993).
165. *Measurement of roughness of two interfaces of a dielectric film by scattering ellipsometry*, T. A. Germer, Phys. Rev. Lett. **85**, 349 (2000).
166. *Nonuniform H distribution in thin-film hydrogenated amorphous Si by small-angle neutron scattering*, D. L. Williamson, D. W. Marr, J. Yang, B. Yan and S. Guha, Phys. Rev. B **67**, 075314 (2003).
167. *Characterization of electron transport at high fields in silicon-on-insulator devices: a Monte Carlo study*, J. B. Roldán, F. Gámiz, A. Roldán and N. Rodríguez, Semicond. Sci. Technol. **21**, 81 (2006).
168. *Theoretical investigation of surface roughness scattering in silicon nanowire transistors*, J. Wang, E. Polizzi, A. Ghosh, S. Datta, M. Lundstrom, Appl. Phys. Lett. **87**, 043101 (2005).
169. *Electronic Properties of Silicon Nanowires: Confined Phonons and Surface*

- Roughness*, E. B. Ramayya, I. Knezevic, D. Vasileska, S. M. Goodnick, IEEE Nanotechnology **1**, 20 (2006).
170. *Quantum transport length scales in silicon-based semiconducting nanowires: Surface roughness effects*, A. Lherbier and et al., Phys. Rev. B **77**, 085301 (2008).
171. *Orientalional dependence of charge transport in disordered silicon nanowires*, M. P. Persson et al., Nano Lett. **8**, 4146 (2008).
172. *Semiclassical transport in silicon nanowire FETs including surface roughness*, J. Comp. Elec. **7**, 355 (2008).
173. *Electron Transport in Silicon Nanowires: The Role of Acoustic Phonon Confinement and Surface Roughness Scattering*, E. B. Ramayya, D. Vasileska, S. M. Goodnick and I. Knezevic, J. Appl. Phys. **104**, 063711 (2008).
174. *Significant enhancement of hole mobility in [110] silicon nanowires compared to electrons and bulk silicon*, A. K. Buin et al., Nano Lett. **2**, 760 (2008).
175. *Giant Enhancement of the Carrier Mobility in Silicon Nanowires with Diamond Coating*, V. A. Fonoberov and A. A. Balandin, Nano Lett. **11**, 2442 (2006).
176. *Electron scattering due to confined and extended acoustic phonons in a quantum wire*, N. Nishiguchi, Phys. Rev. B **54**, 1494 (1996).
177. *Phonon scattering and energy relaxation in two-, one-, and zero-dimensional electron gases*, U. Bockelmann and G. Bastard, Phys. Rev. B **42**, 8947 (1990).
178. *Electron-acoustic-phonon scattering rates in rectangular quantum wires*, S. G. Yu et al., Phys. Rev. B **50**, 1733 (1994).
179. *Theory of transport in silicon quantum wires*, G. D. Sanders, C. J. Stanton and Y. C. Chang, Phys. Rev. B **48**, 11067 (1993).
180. *Electron-acoustic phonon interaction in semiconductor nanostructures*, F. Grosse and R. Zimmermann, Physics of semiconductors, 28th International conference.
181. *Assessment of room-temperature phonon-limited mobility in gated silicon nanowires*, R. Kotlyar et al., Appl. Phys. Lett. **84**, 5270 (2004).
182. *Physical Properties of Carbon Nanotubes*, R. Saito, G. Dresselhaus and M. S. Dresselhaus, Imperial College Press, 1998.
183. *Molecular Junctions by Joining Single-Walled Carbon Nanotubes*, M. Terrones et

- al, Phys. Rev. Lett. **89**, 075505 (2002).
184. *Tunneling conductance of connected carbon nanotubes*, R. Saito, G. Dresselhaus, and M. S. Dresselhaus, Phys. Rev. B **53**, 2044 (1996).
185. *Pure Carbon Nanoscale Devices: Nanotube Heterojunctions*, L. Chico et al, Phys. Rev. Lett. **76**, 971 (1996).
186. *Quantum conductance of carbon nanotubes with defects*, L. Chico et al, Phys. Rev. B **54**, 2600 (1996).
187. *Carbon-Nanotube-Based Quantum Dot*, L. Chico, M. P. López Sancho, and M. C. Muñoz, Phys. Rev. Lett. **81**, 1278 (1998).
188. *Electronic states in zigzag carbon nanotube quantum dots*, C. G. Rocha, T. G. Dargam, and A. Latgé, Phys. Rev. B **65**, 165431 (2002).
189. *Carbon nanotube intramolecular junctions*, Zhen Yao et al, Nature (London) **402**, 273 (1999).
190. *Length-dependent transport properties of (12,0)/(n,m)/(12,0) single-wall carbon nanotube heterostructures*, Wenxing Zhang, Wengang Lu, and E. G. Wang, Phys. Rev. B **72**, 075438 (2005).
191. *Electronic Transport in Mesoscopic Systems*, S. Datta, Cambridge University Press, 1995.
192. *Transport in Nanostructures*, D. K. Ferry and S. M. Goodnick, Cambridge University Press, 1997.
193. *Spatial Variation of Currents and Fields Due to Localized Scatterers in Metallic Conduction*, R. Landauer, IBM J. Res. Develop. **1**, 223 (1957); Philos. Mag. **21**, 863 (1970).
194. *Generalized many-channel conductance formula with application to small rings*, M. Büttiker, et al, Phys. Rev. B **31**, 6207 (1985).
195. *A new tight binding parametrization for carbon*, L. Goodwin, J. Phys.: Condens. Matter **3**, 3869 (1991).
196. *Tight-binding molecular-dynamics study of phonon anharmonic effects in silicon and diamond*, C. Z. Wang, C. T. Chan, and K. M. Ho, Phys. Rev. B **42**, 11276 (1990).

197. *Environment-dependent tight-binding potential model*, M. S. Tang, et al., Phys. Rev. B **53**, 979 (1996).
198. *Tight-Binding Approach to Computational Materials Science*, P. E. A. Turchi, A. Gonis, and L. Colombo, MRS Proceedings **491** (1997).
199. *Brownian Motion of a Quantum Oscillator*, J. Schwinger, J. Math. Phys. **2**, 407 (1961).
200. *Diagram technique for non-equilibrium processes*, L. V. Keldysh, Sov. Phys. JETP **20**, 1018 (1965).
201. *Non-Equilibrium Green's Function (NEGF) Formalism: An elementary Introduction*, S. Datta, Proceedings of the International Electron Devices Meeting (IEDM), IEEE Press (2002).
202. *Non Equilibrium Green's Functions for Dummies: Introduction to the One Particle NEGF equations*, M. Paulsson, arXiv.org cond-mat/0610247 (2002).
203. A. P. Jauho (2006), "Introduction to the Keldysh Nonequilibrium Green Function Technique," <http://www.nanohub.org/resources/1877>
204. *Quick iterative scheme for the calculation of transfer matrices: application to Mo (100)*, M P Lopez Sancho, J M Lopez Sancho and J Rubio, J. Phys. F **14**, 1205 (1984).
205. *Highly convergent schemes for the calculation of bulk and surface Green functions*, M P Lopez Sancho, J M Lopez Sancho, J M L Sancho and J Rubio, J. Phys. F **15**, 851 (1985).
206. *Electronic transport in extended systems: Application to carbon nanotubes*, M. B. Nardelli, Phys. Rev. B **60**, 7828 (1999).
207. *Single and multiband modeling of quantum electron transport through layered semiconductor devices*, Roger Lake, Gerhard Klimeck, R. Chris Bowen, and Dejan Jovanovic, J. Appl. Phys. **81**, 7845 (1997).
208. *Transformation properties of three sets of closed time path green's functions*, G. Z. Zhou, L. Yu, B. L. Hao, Acta physica sinica **29**, 878 (1980).
209. *Quantum Kinetics in Transport and Optics of Semiconductors*, H. Haug and A. P. Jauho, Springer-Verlag, 1998.

210. *Conductance spectra of metallic carbon nanotube heterojunctions*, Wenxing Zhang et al., Phys. Rev. B **75**, 193410 (2007).
211. *Inelastic scattering of neutrons in solids and liquids*, G. Dolling, IAEA, Vienna, Vol. II, 37 (1963).

Publication & Meeting

Publication:

1. *Length-dependent transport properties of (12,0)/(n,m)/(12,0) single-wall carbon nanotube heterostructures*, Wenxing Zhang, Wengang Lu, and E. G. Wang, Phys. Rev. B **72**, 075438 (2005).
2. *Conductance spectra of metallic carbon nanotube heterojunctions*, Wenxing Zhang, Wengang Lu, Hong Guo, and E. G. Wang, Phys. Rev. B **75**, 193410 (2007).
3. Paper on e-ph coupling dependence of transport properties in SiNWs is in preparation, Wenxing Zhang, et al.

Meeting:

1. *Length dependent transport properties of (12,0)/(n,m)/(12,0) SWCNT junctions*, Wenxing Zhang, Wengang Lu, and E. G. Wang, 15' oral presentation in CPS2005 Fall Meeting (18-21/09/2005).
2. *Length dependent transport properties of (12,0)/(n,m)/(12,0) SWCNT junctions*, Wenxing Zhang et al., poster in ACCMS-3 (8-11/09/2005).